

University of Nottingham
UK | CHINA | MALAYSIA

Synthesis and encapsulation of biocompatible PbS quantum dots passivated with different capping ligands

Mohammed Safaa Shawkat Alnajjar

B.Sc. (Chemistry), M.Sc. (Chemistry)

Thesis submitted to the University of Nottingham for the degree of Doctor of Philosophy

September 2018

Declaration

The work presented in this thesis in chapters 3, 4, 5 and 6 has been performed by myself in the University of Nottingham and no part has been submitted for any other degree at the University of Nottingham or other institutions.

Mohammed Safaa Alnajjar

September 2018

Abstract

Semiconductor nanoparticles, also known as quantum dots (QDs), have unique properties including stable fluorescence with high quantum yields. These properties are size and composition dependent. QDs are promising candidates for non-invasive deep tissue imaging in the near-infrared wavelength range 700 - 1400 nm in which there is low absorption in biological tissues. In addition, QDs could offer opportunities for anticancer treatments.

Currently, available commercial facilities are equipped with charge-coupled device CCD detection with range up to 1000 nm, hence there is a demand for imaging labels for this wavelength range. In this project, new lead sulfide PbS QDs capped with thioglycolic acid (TGA), L-cysteine (L-Cys), L-cysteine methyl ester (L-CysOMe), glutathione (GSH) and TGA/L-CysOMe have been synthesised in aqueous solution. These QDs exhibited good chemical stability and optical emission in the near-infrared region (880 – 950 nm). Also, the diameter of these QDs is 3 – 4 nm, which makes them suitable for encapsulation inside nanocage protein.

Among a variety of delivery capsules, apoferritin (AFt) is of particular interest for QD encapsulation. A cysteine-free human heavy chain apoferritin (AFt-) has been expressed and purified to encapsulate the QDs. In order to achieve specific targeting toward cancer cells with human epidermal growth factor receptor 2 (HER2) overexpression, a modified version of AFt- cage with an average of 4 affibody copies (Afb-AFt-) was prepared for the QDs encapsulation.

In this project, two types of the synthesised QDs, capped with TGA/L-CysOMe and GSH, were successfully encapsulated separately inside the protein cages, which has not been reported previously. The

encapsulation of the QDs was achieved by different routes: altering pH/Urea initiated reassembly/nanoreactor route. The encapsulated QDs in both proteins, AFt- and Afb-AFt-, were prepared with optical and chemical stability.

The cytotoxicity of PbS QDs alone and encapsulated in AFt- was examined *in vitro* by determining the cell viability using the MTT assay. Two types of breast cancer cells were used, MDA-MB-231 (HER2 negative control) and SKBR3 (HER2 positive control). The growth inhibition factor (GI_{50}) values were determined to quantify the cytotoxic effect of the QDs in the cancer cells. The GI_{50} values of the PbS QDs studied (0.07 mg/mL) decreased in both cancer cell lines following encapsulation in AFt- (0.05 mg/mL) which indicates the higher toxic effect after the encapsulation by the AFt-.

The selectivity of the QDs to target HER2 receptors was examined on both cancer cell lines. PbS QDs capped with TGA/L-CysOMe or GSH ligands and their encapsulation were used. The GI_{50} values decreased when SKBR3 cells were exposed to the Afb-AFt-QDs (0.01 mg/mL) compared to QDs and AFt-QDs (0.1 mg/mL). While the increase in the GI_{50} values following the encapsulation of the QDs inside the Afb-AFt- indicates a lower level of toxicity in the MDA-MB-231 (0.16 mg/mL).

In this project; stable, biocompatible and NIR active PbS QDs capped with TGA/L-CysOMe and with GSH capping ligands were synthesised. The produced QDs were successfully encapsulated into the AFt- and Afb-AFt- capsules. The encapsulated QD solutions are biocompatible, emit in the NIR region and are stable over a period of at least 3 weeks. The delivery and selectivity of the QDs toward specific (HER2-positive) cells were improved by the encapsulation inside the AFt- and Afb-AFt- cages.

Acknowledgements

No work is completed individually. I would like first to thank my amazing supervisors Prof. Neil R. Thomas and Dr Lyudmila Turyanska for offering me the opportunity to do my PhD in the University of Nottingham under their supervision, support, expertise, guidance, and encouragement. Also, I would like to thank my country (Republic of Iraq) and the Ministry of Higher education and scientific research in Iraq and the Iraqi cultural attaché in London for offering me funding for this studentship.

Also, I would like to thank Dr Francesco Zamberlan, Dr Lei Zhang and Dr Ali Al-Ani for their help and scientific discussions about subjects and ideas related to my project.

Special thanks to all staff and student in Centre for Biomolecular Sciences (CBS) especially those working in C28 and A20 labs for their support during my study.

A special thanks to my Mom and Dad and my family in Iraq for their encouragement during my studies.

And finally, a special thanks to my lovely wife Rawaa for her patience and support the 4 years of my study and taking care of our lovely daughter and son.

Mohammed Safaa Alnajjar

September 2018

Abbreviations

Afb	Affibody
Afb-AFt-	Affibody-Apoferritin
AFt	Apoferritin
AFt-	Apoferritin cysteine free
BSA	Bovine serum albumin
d	Diameter
DLS	Dynamic Light Scattering
DNA	Deoxyribonucleic acid
Dps	DNA binding proteins from starved cells
DTG	Dithioglycerol
E. coli	*Escherichia coli*
E_g	Energy gap
FBS	Fetal bovine serum
FRET	Fluorescence Resonance Energy Transfer
FRT	Ferritin
GSH	Glutathione
HER	Human Epidermal growth factor Receptor
HOMO	Highest Occupied Molecular Orbital
IPTG	Isopropyl-β-thiogalactopyranoside
LB	Luria Bertani media
L-Cys	L-Cysteine
L-CysOMe	L-Cysteine methyl ester
LOBSTR	Low Background Strain
LUMO	Lowest Unoccupied Molecular Orbital
MALDI-TOF	Matrix-Assisted Laser Desorption/Ionisation Time-Of-Flight
MBA	2-((E)-2-((E)-2-((2- carboxyethyl)thio)-3-(2-((E)-3,3-dimethyl-1-(3-sulfopropyl) indolin-2-ylidene)

	ethylidene)cyclohex-1-en-1-yl)vinyl)-3,3-dimethyl-1-(3-sulfopropyl)-3H-indol-1-ium
MBP	Maltose Binding Protein
mL	Millilitre
M	Molar
MMP	Metalloproteinase
MTT	3-(4,5-Dimethylthiazol-2-yl)-2,5-diphenyltetrazolium bromide solution
M.wt	Molecular weight
Ni-IMAC	Nickel (II) - Immobilized Metal Ion Affinity Chromatography
NIR	Near-infrared
nm	Nanometre
ns	Nanosecond
OD	Optical Density
PAGE	Polyacrylamide gel electrophoresis
PBS	Phosphate-buffered saline (KH_2PO_4 (1.8 mM) pH 7.4, Na_2HPO_4 (10 mM), KCl (2.7 mM), NaCl (137 mM))
PbS	Lead sulfide
PL	Photoluminescence
PMSF	Phenylmethylsulfonyl fluoride
QDs	Quantum Dots
ROS	Reactive Oxygen Species
SD	Standard Deviation
SDS	Sodium dodecyl sulfate
SEC	Size Exclusion Chromatography
TEM	Transmission Electron Microscopy
TEMED	Tetramethylethylenediamine
TGA	Thioglycolic acid
TGL	Thioglycerol

Tris	Tris (hydroxymethyl)aminomethane
v/v	Volume per volume
w/v	Weight per weight
λ_{max}	Photoluminescence peak position

Table of contents

1. Introduction 1
   1.1. Colloidal nanomaterial 1
      1.1.1. Quantum dots 2
      1.1.2. Quantum confinement 5
      1.1.3. Role of capping ligands 9
      1.1.4. Biocompatibility of quantum dots and cytotoxicity ... 10
      1.1.5. QDs for biomedical imaging 12
      1.1.6. Cytotoxicity of QDs 15
   1.2. Nanomedicine and drug delivery vehicles 17
      1.2.1. Ferritin family 21
      1.2.2. Apoferritin 25
      1.2.3. Applications of apoferritin in biomedicine 27
      1.2.4. Affibody 32
   1.3. Breast cancer and the role of HER2 receptors 36
   1.4. Aim and Objectives 39
2. Materials and methods 41
   2.1. PbS QDs synthesis 41
      2.1.1. Thioglycolic acid capped PbS QDs 42
      2.1.2. L-Cysteine capped PbS QDs 42
      2.1.3. L-CysOMe PbS QDs 44
      2.1.4. PbS QDs capped with mixed ligands 44
      2.1.5. GSH PbS QDs 46
   2.2. Optical and morphological characterisation 46
      2.2.1. Photoluminescence measurements 46
      2.2.2. Dynamic Light Scattering (DLS) 47
   2.3. Protein preparations 49
      2.3.1. Transformation of plasmids and protein expression . 49
      2.3.1. Sodium dodecyl sulphate polyacrylamide gel electrophoresis 52
      2.3.1. Polyacrylamide gel electrophoresis of native proteins... 53

2.3.2. Nickel-immobilised metal ion affinity chromatography 54
2.3.3. Size Exclusion Chromatography 55
2.3.4. Ammonium sulfate precipitation 56
2.3.5. Protein concentration measurements 57
2.3.6. Matrix Assisted Laser Desorption/Ionisation Time- of-Flight mass spectrometry 58
2.3.7. Purification of AFt-, Afb and Afb-AFt- 58
2.3.8. Preparation of affibody-apoferritin with an average of 4 copies of affibody on the surface 60
2.3.9. Improving the purity of the Afb-AFt- 61
2.3.10. Western blot 63
2.4. PbS QDs encapsulation by AFt- and Afb-AFt- 65
2.4.1. L-Cys PbS QDs 67
2.4.2. L-CysOMe PbS QDs 67
2.4.3. TGA/L-CysOMe PbS QDs 67
2.4.4. GSH PbS QDs 68
2.5. *In vitro* studies 69
2.5.1. Subculturing cell lines 69
2.5.2. MTT assay 69
3. Synthesis of PbS QDs with different capping ligands 73
3.1. Introduction 73
3.2. TGL/DTG PbS QDs 74
3.3. TGA PbS QDs 76
3.4. L-Cys PbS QDs 79
3.5. L-CysOMe PbS QDs 87
3.6. TGA/L-CysOMe PbS QDs 90
3.7. GSH PbS QDs 95
3.8. Comparison between the different synthesised PbS QDs 101
3.9. Conclusions 103
4. Apoferritin purification and characterisation 104
4.1. Introduction 104
4.2. Estimation of Aft- and Afb-AFt- native molecular weight 105

4.3. Expression and purification of human heavy chain apoferritin 107
4.4. Expression and purification of affibody 113
4.5. Expression and purification of affibody-apoferritin..... 114
4.5.1. Optimisation of the expression and purification of Afb-AFt-. 117
4.5.2. Preparation of Afb-AFt- with 4 Afb copies 122
4.6. Conclusions 124
5. Encapsulation of PbS QDs 125
5.1. Encapsulation methods 125
5.2. Human heavy chain apoferritin encapsulated PbS QDs 127
5.2.1. L-Cys PbS QDs and L-CysOMe PbS QDs 127
5.2.2. TGA/L-CysOMe PbS QDs 131
5.2.3. GSH PbS QDs 136
5.3. Affibody-apoferritin encapsulated PbS QDs 141
5.3.1. TGA/L-CysOMe PbS QDs 141
5.3.2. GSH PbS QDs 144
5.4. Conclusions 146
6. Cytotoxicity studies of PbS QDs 148
6.1. *In vitro* studies of PbS QDs 148
6.2. Cytotoxicity of AFt-, Afb and Afb-AFt- 149
6.3. MTT assay of protein encapsulated PbS QDs 155
6.3.1. AFt- encapsulated TGA/L-CysOMe PbS QDs 155
6.3.2. Afb-AFt- encapsulated TGA/L-CysOMe PbS QDs 157
6.3.3. AFt- encapsulated GSH PbS QDs 160
6.3.4. Afb-AFt- encapsulated GSH PbS QDs 162
6.3.5. The effect of the protein encapsulation on the cytotoxicity of the QDs 164
6.4. Conclusions 167
7. Conclusions and future works 169
8. References 172

Chapter 1

1. Introduction

1.1. Colloidal nanomaterial

The nanoscience research area that deals with the properties of nanoscale particles is currently one of the fastest developing fields of research due to its interdisciplinary applications in areas such as medicine.[1] Nanoparticles have a wide range of potential applications in bioimaging due to their unique optical and electronic properties. The ability to control the size and shape of nanomaterials is leading to the development of different colloidal nanoparticles such as metal nanoparticles (Au nanoparticles)[2], nanotubes (graphene-based nanotubes)[3] and semiconductor nanoparticles (II-VI, III-V and IV-VI).[4]

Different studies have been reported on the development of nanomaterials synthesised for applications in medicine and for bioimaging. However, development of synthetic routes to produce nanomaterials with controlled physical and chemical properties is required. In this project, PbS QDs have been selected to use them as fluorescent materials for bioimaging in the 1st NIR range of low absorption of biological tissues.

Semiconductor quantum dots are advantageous for applications in bioimaging as they can be produced with a controlled size and shape.

However, the stability, biocompatibility and cytotoxicity of the QDs remain a challenge for their use.

1.1.1. Quantum dots

In the past two decades, attention has been focused on the preparation of semiconductor nanoparticles, known as quantum dots (QDs), and their applications in photoelectric devices, solar cells, photo catalysis, photoconductors and biological imaging according to their special structural, optical and electrical properties.[4,5,6] The first QDs were discovered by Burs[7] in 1985 when ZnS and CdS particles were prepared. Recently, numerous QDs have been developed with different sizes, shapes, compositions and emission properties.[7,8]

A wide range of materials have been used to synthesise nanocrystal QDs. QDs composed of elements from groups II–VI (CdSe, CdTe)[9], III–V (InP, InAs)[10] and IV–VI (PbSe, PbS) have been produced.[11] Different wavelength emissions ranging from the UV region to the IR region have been obtained from different QDs due to the usage of materials with different compositions to produce different sizes of QDs, Figure 1.1.[12]

QDs of II–VI group materials have been successfully synthesised in nonpolar solvents and the surface has been modified with amphiphilic ligands to give them solubility in polar solvents.[13] However, their emission in the visible wavelength region limits their use in deep tissue imaging due to the absorbance of the biological molecules in this region.[14] This limitation may potentially be overcome by using

IV–VI semiconductor nanocrystals, such as PbS QDs, which have tuneable emissions in the NIR wavelength region which is of potential interest for non-invasive deep tissue imaging.[15,16,17]

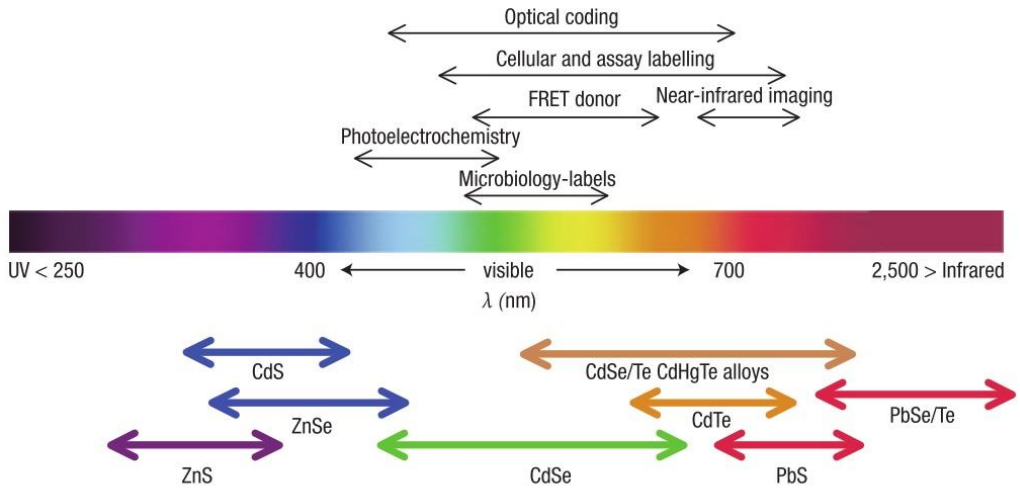


Figure 1.1. Wavelength range of optical emission of the QD depending on their composition.[12]

Over the past few decades, organic dyes have been widely used for bioimaging. Their availability to fluoresce in different colours and ability to link to other molecules such as proteins to reach the targeted tissues has made them popular.[18] However, their usage faces limitations, especially for deep imaging. The excitation of the fluorophore is very narrow and specific for each dye and their emission is also in a very narrow bandwidth.[19] Also, to achieve images with different colours, a mixture of fluorophores is required; however, complex analysis is then required to solve the images in addition to their high cost. In contrast, QDs with their potential properties overcome these limitations.[20] Optical properties of QDs such as

narrow tuneable fluorescence emission and high quantum yield make them promising for replacement of currently used organic dyes in biomedical optical imaging. [21,22,23]

A stronger fluorescence intensity can be achieved using QDs as compared with organic fluorescence dyes. In addition, QDs have high fluorescence stability, which gives QDs the ability to resist photobleaching due to the high chemical stability of the QDs.[24] Photobleaching is a phenomenon of fluorescence intensity reduction due to the luminescent material decomposing in response to optical excitation.[25] Based on QDs potential photochemical stability that resists photobleaching, organs and cells labelled by QDs can be detected for a long time.[25]

The fluorescence lifetime of QDs is longer compared to organic dyes and biomolecules (currently used), whose PL lifetime < 100 ns. QDs labels with a long lifetime can prevent the artefacts due to fluorescence of the biological molecules.[26] PbS QDs capped with oleic acid and octadecene synthesised at room temperature were reported to have a lifetime ranging between 250 and 2500 ns depending on the QDs' size.[27] Further studies also reported that CdSe QDs have luminescence lifetime (20 to 50 ns).[28]

The efficiency of the bioimaging label is related to nanoparticles quantum yield, which is defined as the relation between the number of emitted photons per the number of absorbed photons.[29] CdSe/ZnS was produced with quantum yield (49%)[29] while PbS QDs were produced with quantum yield (39%).[30]

1.1.2. Quantum confinement

The unique properties of QDs are due to their nanoscale size that leads to the quantum confinement effect. The confinement of the electrons means a limitation of their movement within a space leading to quantization of their energy.

Bulk semiconductors have a characteristic energy gap, E_g (band gap), which is different for each type of bulk semiconductor material. This is an energy range where there are no states available for the electron to occupy. All valence electrons are occupying the states with an energy below the energy gap which is known as valence band. At the $E > E_g$, there are states available for the electron to occupy in which is known as conduction band. Upon absorption of $E > E_g$ (e.g., absorption of the photon), electrons can be transferred from the valence band to the conduction band. The band gap energy is the minimum energy required to transfer the electron from the valence band to the conduction band. The created electron-hole pair is called an exciton, Figure 1.2.A. The minimal physical distance between the electron in the conduction band and its hole in the valence band is called the exciton Bohr radius.[31] QDs fluorescence emission occurs when the excited electron relaxes to valence band and the E is released as light with energy equal to the band gap energy.

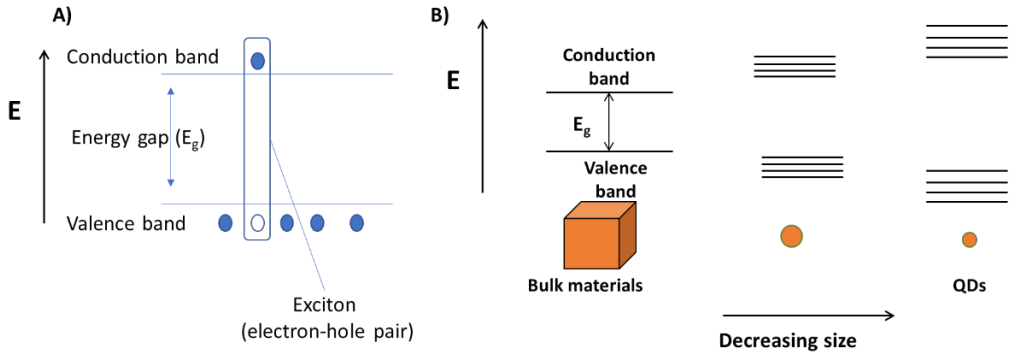


Figure 1.2. A) Schematic diagram illustrating exciton formation, and B) Schematic diagram of *E* bands of bulk semiconductors and QDs showing the formation of discrete energy bands by reducing the particle size.

When a bulk material is reduced to nanoscale dimensions, and the density of states decreases near the conduction band and valence band edges, the emergence of discrete excitonic states occur. The band gap energy further increases with decreasing nanocrystal size as the exciton is confined to smaller dimensions than its Bohr radius. The PL emission wavelength shifts since exciton recombination occur between the band edge states (Figure 1.2.B).[32] Decreasing the size of the nanocrystal leads to an increase in the quantum confinement by increasing the space between the energy levels. The colour and emission wavelength of a QD is determined by its size and composition. Wavelengths of light ranging from the ultraviolet (UV) to the infrared (IR) can be emitted from QDs.[33]

The QD fluorescence mechanism begins when an electron of semiconductor is excited by photons with energy higher than the band gap, then the electrons relax to the lowest level of the conduction band and release energy as heat. Then the electron

transfers from the conduction band to the valence band and emits the energy as light to be detected in a specific region depending on the size of the QD. (Figure 1.3).

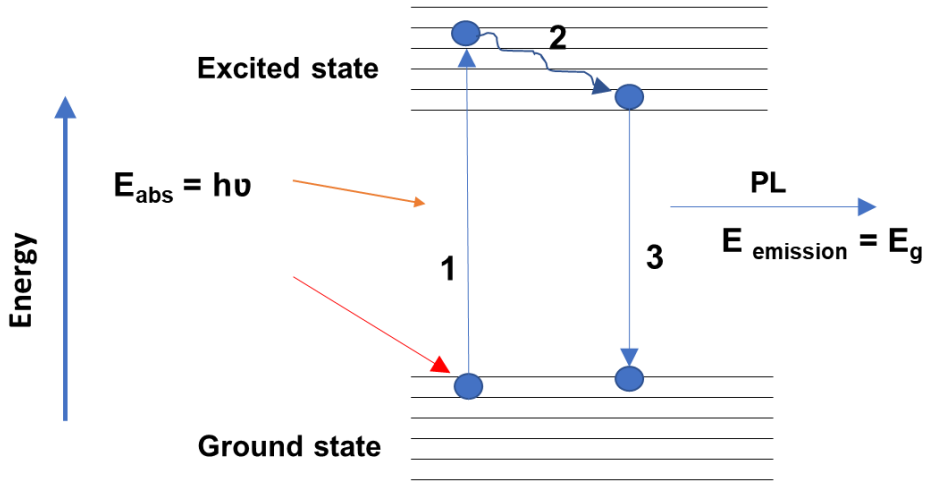


Figure 1.3. A diagram of the fluorescence mechanism illustrating 1) the photon absorption and excitation of electron from the ground state to the excited state, followed by 2) the non-radiative relaxation and 3) the relaxation to the ground stated and emission of the light.

QDs of lead chalcogenides such as PbS and PbSe have a bulk cubic crystal structure with Bohr radii of 18 nm and 48 nm, respectively. Also, PbS and PbSe have narrow energy band gaps of 0.41 and 0.28 eV respectively. These result in strong confinement effects with tunable energy band gaps between 0.3–1.7 eV, which gives them a potential advantage for imaging in the NIR region.[11]

The relation between the QDs size and their E_g was studied theoretically and experimentally by Moreels *et al.*[34] The dependence of E_g on QDs diameter of the PbS QDs can be described theoretically by the equation (1), where $E_{g(QDs)}$ is the band gap energy of quantum

dot, $E_{(bulk)}$ is band gap energy of bulk semiconductor, h is plank constant, R is radius of quantum dot, m^*_e is effective mass of excited electron, m^*_h is effective mass of excited hole, e is electronic charge, ε_o is permittivity of vacuum and ε_r is relative permittivity.

$$E_{g(QD)} = E_{(bulk)} + \frac{h^2}{8R^2}\left(\frac{1}{m_e^*} + \frac{1}{m_h^*}\right) - \frac{1.786\, e^2}{4\pi\varepsilon_o\varepsilon_r R^2} \qquad (1)$$

For PbS QDs with diameter *d* ranging from 3.9 to 13.3 nm. The calculated values were compared to the experimental values estimated by PL measurements (Figure 1.4). The experimental and theoretical values were in good agreement with the model.[35] This dependence can be used to determine the size of the PbS QDs from measured PL peak positions.[34] The observed increase of E_g arises from the increasing strength of the quantum confinement resulting from the decreasing QD size.

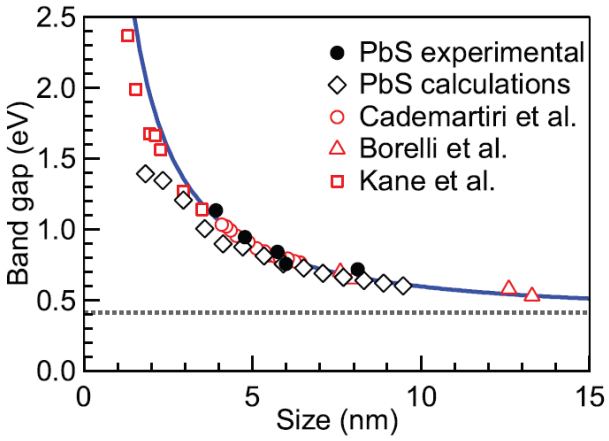


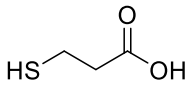
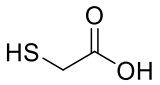
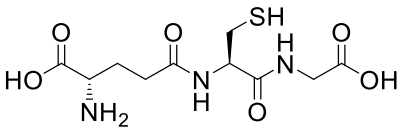
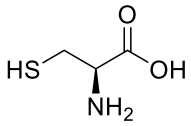
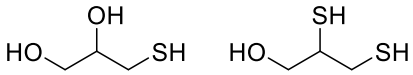
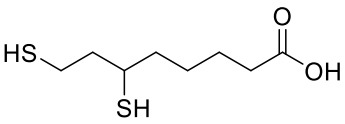
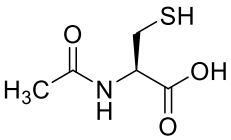
Figure 1.4. The relationship between QD diameter and the band gap energy (eV) for PbS QDs. The solid blue line is the fitted curve to indicate the QDs size and the dotted line is the E_g of bulk material, PbS experimental: is the synthesised QDs, PbS calculation: QDs from the equation of the model and Cademartiri *et al*., Borelli *et al*. and Kane *et al*. are another QDs from the literature.[34]

1.1.3. Role of capping ligands

QD surface passivation plays an important role in QDs solubility, size and optical properties. Thiol ligands are commercially available and inexpensive. Ligands with thiol groups are used to cap the QDs. Thiol groups can coordinate to metal ions such as Pb^{2+} on the QD surface. Also, depending on their hydrophilicity, thiol ligands are able to increase the aqueous solubility of the QDs and increase their biocompatibility due to coating the QDs surface with a hydrophilic layer.[36] Furthermore, the small size of thiol capping ligands are not highly affected the hydrodynamic size of the QDs. In addition, the availability of terminating functional groups on the capping ligands can be conjugated with other functional molecules such as peptides and antibodies for specific applications such as targeted cancer receptors cells.[37]

Different molecules containing thiol groups have been reported to cap QDs and are summarised in Table 1.1. Different types of QDs were solubilised and functionalised using ligands containing thiol groups. The high affinity of the S group to link to the metal ion of the QDs plays an important role in the formation, size control and solubility of QDs. To date, different QDs have been produced in aqueous solution. CdSe QDs capped with mercaptosuccinic acid were prepared and are stable for up to 6 months.[38] PbS QDs capped with TGA have been reported to be stable for 12 months in aqueous solution.[39] In this study we have used TGA, L-Cys, L-CysOMe, GSH and their mixture to passivate the surface of the PbS QDs.

Table 1.1. A list of thiol-containing capping ligands are reported in the litereture of producing biocompatible QDs with different composition

Ligands	Structures	QDs core
3-Mercaptopropionic acid (3-MPA)		PbS[40] CdTe[41]
Thioglycolic acid		PbS,[42] CdSe[43]
L-Glutathione		ZnS,[44] CdTe[45]
L-Cysteine		PbS,[46] CdTe[47]
TGL/DTG		PbS[48]
DHLA		PbS,[49] ZnS[50]
N-acetyl-L-cysteine		ZnCdSe[51]

1.1.4. Biocompatibility of quantum dots and cytotoxicity

The biocompatibility of QDs is one of the major challenges for any potential biological application. QDs must be soluble in physiological solvents and must not interfere with physical functions.[52] The purpose of modifying the nanocrystal surface is to achieve colloidal stability in biological media without altering the photochemical

properties of the QDs.[53,54] The surface of the QDs allows additional functionalisation with biomolecules such as peptides, nucleic acids, antibodies and proteins, hence enabling targeting for specific sites or cells within the body.[55,56]

Different approaches have been considered to solubilise the QDs. Dawei *et al.*[57] developed a new procedure to convert oil soluble oleic acid capped QDs into water soluble QDs by using the hydrophilic thiol ligand, glutathione, and produced highly soluble QDs with high quantum yield (30 %). In addition, these QDs were used *in vivo* for imaging and showed high stability and low toxicity.[57]

Three main strategies that have been used to improve the solubility of QDs in aqueous solution are ligand exchange, encapsulation and combinations of layers.[53] Ligand exchange can be achieved by replacing the hydrophobic ligand initially used in the preparation of QDs by hydrophilic molecules such as thiol ligands because they have a higher affinity for the QD surface, such as replacing oleate with 3-mercaptopropionic acid (3-MPA) and solubilising the CdSe/ZnS core/shell QDs.[58]

The encapsulation strategy is accomplished by covering the hydrophobic surface of the QDs by molecules of polar and nonpolar terms, where the nonpolar side link to the hydrophobic ligand and the polar side is soluble in aqueous solution. Amphiphilic diblock layer, silica shell and PEGylated phospholipid micelle were used to coat CdSe/ZnS, CdSe/CdS and PbS QDs, respectively.[59,60,61] The encapsulation strategy using the mentioned molecules does not

produce stable QDs in biological condition due to the weak interaction between the nonpolar sides of each molecule.[62]

The combination of layers strategy can be accomplished by covering the QDs with a layer ends with thiol and/or amine group such as DNA segments to achieve aqueous solubility.[63] This method is complicated and the conjugated QDs present a reduction in the PL quantum yield.[64]

1.1.5. QDs for biomedical imaging

Medical bioimaging was realized first by Wilhelm Röntgen[65] in 1895 after his discovery of the X-ray and was applied to image the bone of a hand on film. This discovery led to the intense development of new imaging techniques such as X-ray computed tomography, magnetic resonance imaging, positron emission tomography, ultrasound and optical imaging, which are necessary for diagnostic medicine.[66] These imaging technologies have differences in the following aspects: resolution, penetration depth, temporal resolution and energy expended for generation of the image.

New imaging technologies were combined with recently developed imaging probes to monitor disease progression and examine cellular and molecular phenomena. Addressing safety and toxicology is important in drug discovery and development, as well as understanding estimating therapeutic efficacy *in vivo*.[67]

Among the different techniques, fluorescent imaging is one of the most attractive modalities for small animal imaging because of its

lower cost, portability and potentially high resolution with controllable fine-tuning. Despite being one of the most attractive techniques to provide non-invasive and non-ionizing *in vivo* visualization, the artefacts of optical imaging induced by the autofluorescence of living biological tissues affect the imaging quality. Also, the absorption of biological tissues limits the depth of imaging and its resolution. Figure 1.5, shows the absorption of the main biological tissues such as water, lipids, oxyhaemoglobin (HbO_2) and deoxyhaemoglobin (Hb), indicating that PL emission in the wavelength range from 700 nm and 1400 nm is beneficial to overcome challenges of autofluorescence and tissue absorption.

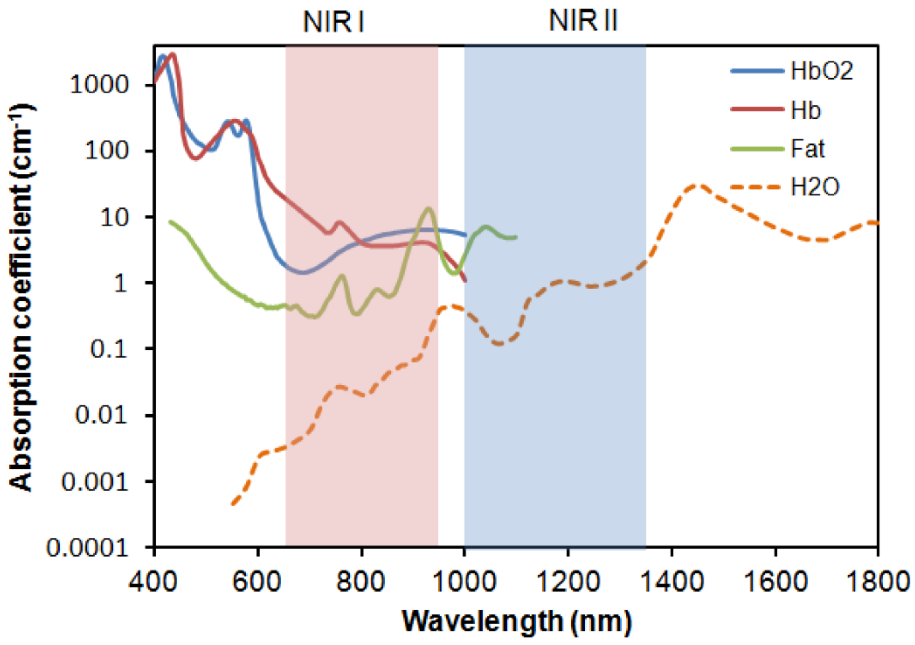


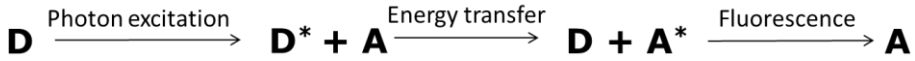
Figure 1.5. Absorption of the biological tissues (HbO_2 Hb, fat and H_2O) and the optical NIR windows.[66]

Intense research has focused on development of highly sensitive and efficient fluorescent probes with emission wavelengths in the first and

second NIR windows of low absorption of biological tissues (NIR I, 650–950 nm and NIR II, 1000–1350 nm).[68]

The selection of suitable imaging labels for *in vivo* imaging depends on many factors. The most important factors would be the molar extinction coefficient and the quantum yield in the NIR region. For more than three decades, organic dyes, such as the cyanine family dyes, have been commonly used for *in vivo* applications, as bioprobes to provide multicolour spectral imaging.[69] However, there are several limitations in their use in bioimaging compared to QDs, such as emission in visible range, low fluorescence intensity, short lifetime and emission time.[20] The narrow PL spectra make the QDs suitable for multiple colour imaging. The longer fluorescence lifetime of QDs compared with that of biological tissues reduces background signal from autofluorescence.[70,71]

Fluorescence resonance energy transfer is also considered for bioimaging in order to avoid the need for external excitation. Fluorescence (or Förster) resonance energy transfer analysis (FRET) involves the transfer of excited fluorescence energy from a donor particle (D) to a neighbour acceptor particle (A). To ensure efficient *E* transfer, the energy range of the emission of D should overlap with absorption of the acceptor. As a result of FRET, fluorescent emission of the acceptor is observed.[72]



Increasing overlap between the emission of the donor and the absorption of the acceptor results in a higher FRET efficiency. However, FRET can be significant only if the donor and acceptor pairs are either part of the same molecule or in close proximity.[73,74]

QDs have been used in FRET pairs. Different studies have attempted to use QDs as donors or acceptor particles. QDs have been used in FRET for measuring protein conformational changes and monitoring protein interactions. CdSe-ZnS core-shell QDs have been applied in FRET studies. A bioconjugate of the engineered maltose binding protein (MBP) connecting with an oligohistidine tail and labelled with an acceptor dye (Cy3) was immobilized on the QDs surface. This module proved to be a good FRET system. Two signals of overlapping spectra of the QDs donor and dye labelled protein acceptor were detected.[75]

1.1.6. Cytotoxicity of QDs

In order to use QDs in biological studies, their potential cytotoxicity has to be addressed. The QDs toxicity depends on many parameters, such as size, shape, composition, concentration, surface coating, photostability and solubility.[76]

Degradation products of QDs might cause harm to the cells or produce an immune response. The toxicity of QDs can be considered in two points. First is the oxidation of the nanoparticle materials and

release of free heavy metal ions, which results in interruption of the cell activities, such as free cadmium ions released from CdSe QDs have been found to cause death in primary liver cell cultures.[77] Second, cellular damage is caused by ROS in cells, and it has been found that ROS can be generated by QDs, resulting in damage to cellular proteins, lipids and nucleic acids.[78]

Nanoparticles could have toxicity due to their size-dependent intracellular uptake. Nanoparticles can reach and access organelles that are not usually accessible to metal ions. It has been observed that metal ions can only locate to the cytoplasm while QDs can localize to the cell's nuclear compartment.[79] For efficient treatment, QDs should not induce mutations of the DNA because the mutations may affect future generations of cells and lead to disease development.[80]

Another important point in QD toxicity is their dose, which can be considered as the most important factor. Dose-dependent QD toxicity was first demonstrated by Dubertret *et al.*[81] by injecting Xenopus frog embryos with different concentrations of ZnS capped CdSe QDs encapsulated within phospholipid block-copolymer micelles. No phenotypic alterations were observed when QDs with a concentration up to 2×10^9 QDs/cell were used. However, abnormalities were observed following exposure to QD concentration $> 5 \times 10^9$ QDs/cell.[81]

Some studies have been undertaken with QDs on smaller animals such as rats and mice, and no abnormal behaviour or cell damage was noticed over a period of months.[82]

Currently, QDs are used for *in vivo* imaging applications. PbS QDs capped with dihydrolipoic acid polyethylene glycol (DHLA-PEG) with free functional groups such as (NH_2 and COOH) have been synthesised with emission in the first and second NIR window. The *in vivo* images were recorded for mice' liver and brain using NIR fluorescence.[49]

To date the best *in vivo* imaging was recorded by using CdSe/CdS/ZnS QDs. QDs encapsulated by β-phospholipid micelle have exhibited non-toxic effects on the blood and biomarker when rhesus macaques were injected with the encapsulated QDs. Also, the major organs did not exhibit any abnormities after 3 months of the injection.[83]

1.2. Nanomedicine and drug delivery vehicles

One of the biggest challenges in nanomedicine is the development of carrier and transporter molecules to deliver nanoparticles or drugs toward targeted cells.[84] To date, different materials have been used as capsules and transporters, such as dendrimers, liposomes, DNA-based cages, virus-based nanoparticles and protein-like cages, Figure 1.6.[85]

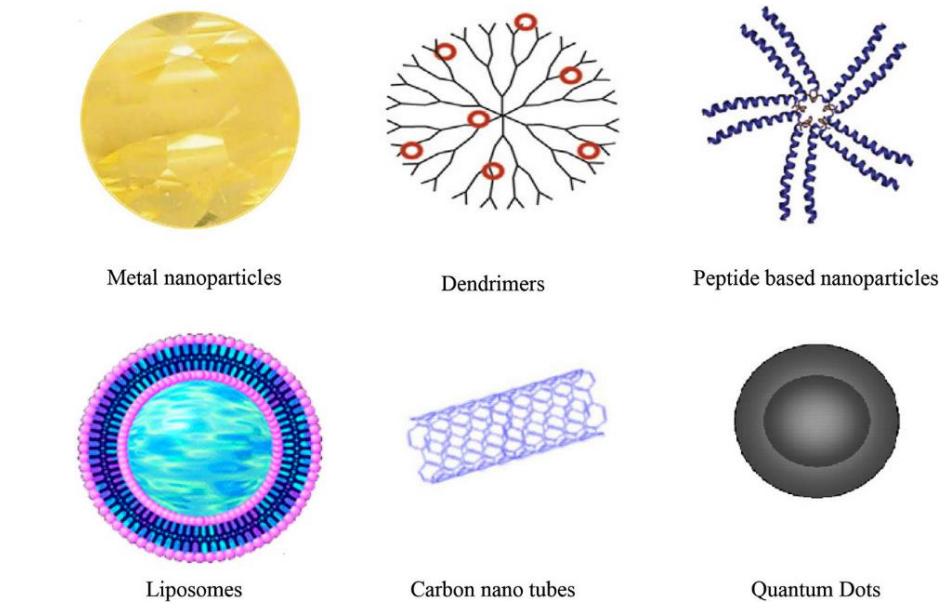


Figure 1.6. Different nanocarriers used for biological applications.[85]

Dendrimers are nanosized molecule, symmetric, homogeneous and monodisperse structures with many arms emanating from a central core that can load and transport small molecules such as drugs.[86] There are at least three strategies to transport nanoparticles in dendrimer cavities: 1) encapsulation in the inner cavity to supply host–guest systems, 2) attachment to the functional groups to provide dendrimer–guest conjugates, and 3) physical interactions between particles and dendrimers to supply dendrimer–guest complexes.[87] Dendrimers had been used to encapsulate different nanoparticles such as gold nanoparticles, Figure 1.7.

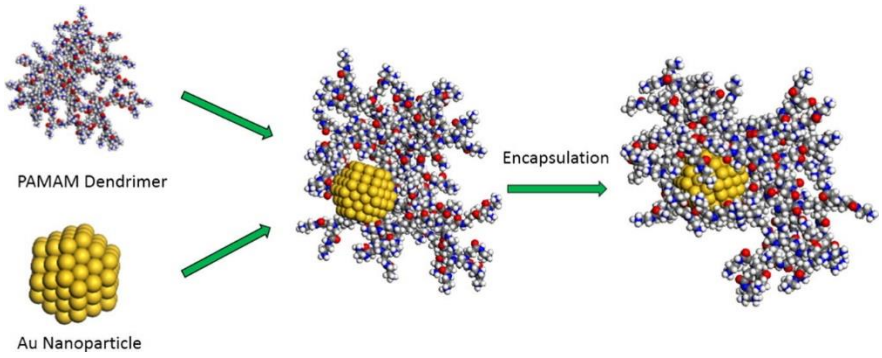


Figure 1.7. Schematic diagram illustrating dendrimer encapsulation of gold nanoparticle.[88]

Liposomes are spherical micro or nanometric vesicles that are composed mostly of lipids or phospholipids and form one or more concentric bilayers where they expose the hydrophilic tail to the outside layer while the hydrophobic parts remain in the inner layer.[89] Liposomes have versatile features in terms of size, surface charge and lipid composition. Liposomes were used to encapsulate drugs, such as cisplatin anticancer agents by forming a bilayer of lipids.[90]

Another capsule has been reported to encapsulate QDs or another nanoparticles is tetrahedral cage of DNA, which is self-assemble of oligonucleotides and forming a rigid structure with tetrahedral shape (Figure 1.8). An efficient encapsulation of CdSe/ZnS core/shell QDs had been achieved with insignificant populations of free oligoes and higher molecular weight complexes (< 20%).[91] A DNA-based cage has also been used to encapsulate gold nanoparticles and QDs.[92]

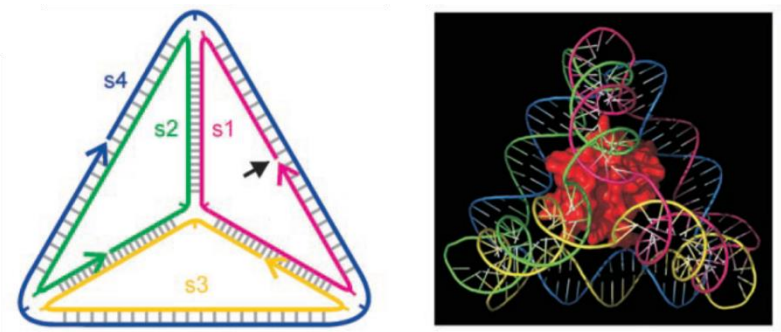


Figure 1.8. A scheme showing the tetrahedral cage of DNA.[93]

Viruses from the chemical standpoint are highly ordered assemblies of biomacromolecules, with known structures and sizes ranging from tens to hundreds of nanometres. Viruses or virus-like particles form hollow cages from multiple capsid protein copies. Various nanoparticles have been encapsulated within these cages such as Ag_2S QDs and gold nanoparticles within the simian virus 40 (SV40) cage.[94]

These capsules may encapsulate drugs or nanoparticles, however, the physiological pathogenesis and the immune response by the living tissues are a challenge to their use. Therefore, native proteins such as ferritins are beneficial for the biological applications. Ferritins are proteins that occur in most living organisms and represent a promising transporter. Many applications have been studied on the use of iron free ferritins, known as apoferritin, as a nanocarrier for various nanomedical purposes.[95,96]

The past few decades have seen strong advances in the development of nanocarrier properties to enable efficient drug delivery. Several

properties are required for potential nanocarriers: 1) they have nanoscale particle size to be absorbed by the cells and can penetrate to deep tissues;[97] 2) a large surface area is required for functionalising and improving their transportation; 3) an ability to protect drugs from degradation; and 4) ability to improve pharmacokinetics, reduce toxicity and improve solubility.[98] The interesting features of useful nanocarriers are summarised in Figure 1.9 and include stability under different physical and chemical conditions, ability to be functionalised and deliver a variety of cargo to targeted tissues.

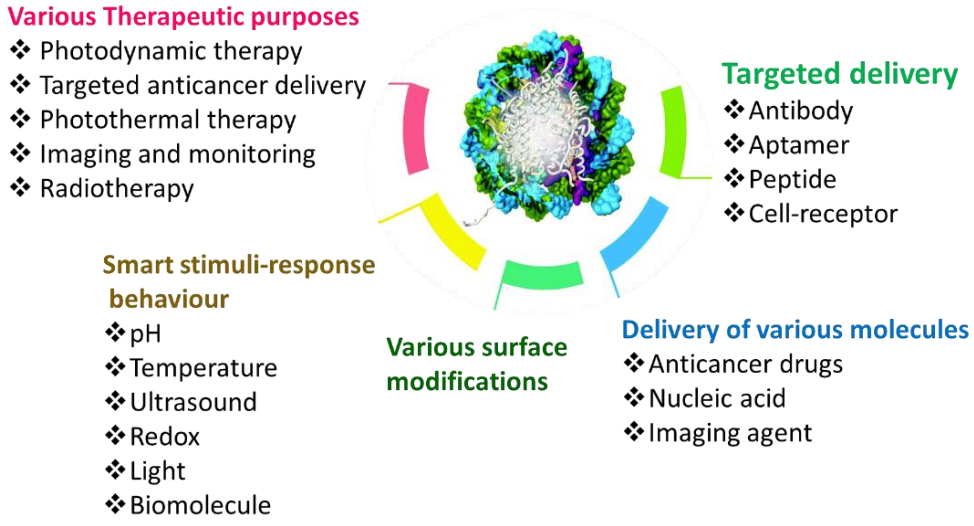


Figure 1.9. Schematic illustration presenting a wide range of capabilities and applications of caged nanoplatforms in nanomedicine and DDSs for delivery of various therapeutic drugs and imaging agents.[99]

1.2.1. Ferritin family

Ferritin was first isolated from horse spleen in 1937 by the French scientist Victor Laufenberg.[100] Since the discovery of ferritins,

numerous studies have been conducted to understand their structures and properties. Ferritin is the major iron storage capsule in living organisms, and responsible for detoxifying the living organisms from excess of iron (II) which leads to damage of living cells through the formation of reactive oxygen species. [101]

Although iron is a necessary mineral in biological systems and processes, it can be toxic at high concentrations due to its role in the generation of reactive oxygen species (ROS), which can result in cell damage from the formation of free radicals. Increasing levels of Fe^{2+} in living tissue and its reaction with hydrogen peroxide leads to the production of a highly reactive hydroxyl radical ($^{\cdot}OH$) through the Fenton reaction. In addition, the formation of non-soluble ferric (Fe^{3+}), which usually precipitates as a ferrihydrite crystal due to its low solubility under physiological conditions (Scheme 1.1).[102,103]

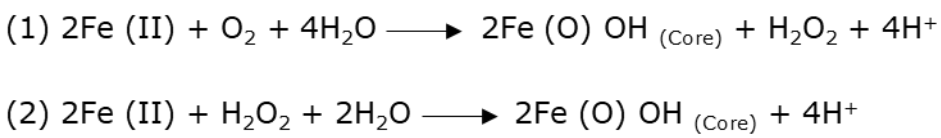
$$Fe^{2+} + H_2O_2 \longrightarrow Fe^{3+} + OH^- + {}^{\bullet}OH \text{ (Fenton reaction)}$$

$$Fe^{3+} + H_2O_2 \longrightarrow Fe^{2+} + HOO^{\bullet} + H^+$$

Scheme 1.1. The formation of the reactive oxygen species and the ferric ions through the fenton reaction.

The main role of ferritins is detoxifying the increase in the ferrous (Fe^{2+}) ions by isolating them inside its cage in the form of ferric (Fe^{3+}) ions. This process starts with the transfer of Fe^{2+} into the cavity through the 3 fold channels (hydrophilic channels) of apoferritin.[104] Then, ferroxidation starts on the cavity surface of ferroxidase site

where Fe^{2+} and O_2 are used to generate insoluble Fe^{3+} compounds. The H_2O_2 produced from the oxidation of the Fe^{2+} ion has been used as an oxidant to produce more insoluble Fe^{3+} ions as ferrihydrite and thus can protect the cells from potential damage (Scheme 1.2).[105]



Scheme 1.2. Describion of the oxidation of Fe^{2+} ions catalysed by the ferroxidase centre of the H-chain AFt subunits

Ferritins are produced in most organisms from humans to invertebrates, plants and microorganisms.[106] Ferritins are classified according to their inner and outer diameter and their molecular weight as miniferritins and maxiferritins.[107] The mini-ferritins contain DNA binding protein from starved cells (Dps), which are 8 nm in diameter with a 5 nm inner cavity, are formed from 12 polypeptide subunits with a molecular weight ~ 240 kDa. The maxi-ferritins include the classical ferritins and the bacterio-ferritins, which are 12 nm in diameter with an 8 nm inner cage, formed from 24 polypeptide subunits with a molecular weight ~ 480 kDa.[108]

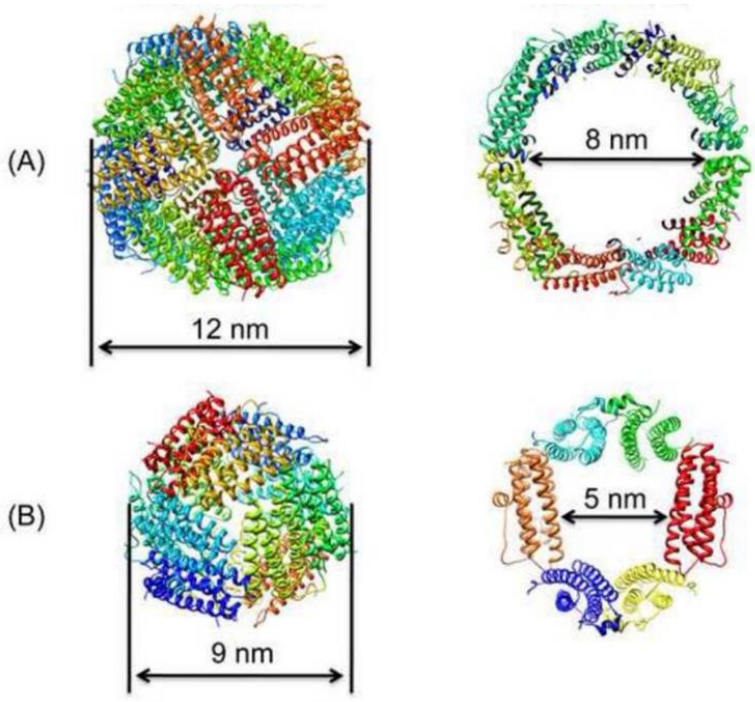


Figure 1.10. Ribbon diagrams showing the interior and exterior diameter for A) AFt (PDB 5N27) and B) Dps (PDB 2BJY).[109]

Mammalian ferritins consist of two types of polypeptide subunits, the heavy chain (H) polypeptide subunits and light chain (L) polypeptide subunits. The H-chain and L-chain subunits have (~ 50 %) similarity of their amino acids sequences.[110] Human ferritins are composed of heavy (22 kDa) and light (19 kDa) chains while bacteria and plants only have H-chain subunits exist.[95]

The heavy chain ferritin is responsible for the oxidation of Fe^{2+} to Fe^{3+} through the ferroxidase centre which exists within the internal hydrophilic region.[111] While the light chain is involved in the nucleation of the iron core by mineralizing the ferrihydrite Fe^{3+} core via the nucleation centre located at the inner surface of its cavity.[112]

Ferritin has an affinity to different receptors, the H-chain apoferritin subunits have an affinity to TfR1 receptors which are overexpressed on different tumour cells such as breast cancer cells (MDA-MB-231).[113] The TfR1 receptors are responsible for the uptake of iron to inside the cells.[114] The expression of TfR1 receptors on tumour cells has been found to be higher than normal cells in same uses due to the requirements of higher levels of iron by cancer cells to increase the metabolism and the DNA synthesis of the cancer cells.[95] While the L-chain subunits have an affinity to scavenger receptor class A member 5 receptors (SCARA5) which are overexpressed on tumour cells such as (MCF-7).[115]

1.2.2. Apoferritin

Apoferritin is the empty protein cage of ferritin (without iron). The apoferritin cage is remarkably stable at temperatures up to 60 ºC for H-chain[116] and a wide range of pH's (2.0–10.0).[117] The apoferritin structure consists of 24 subunits forming a spherical cage. Each subunit interacts with other subunits via noncovalent interactions to form the whole apoferritin cage with a molecular weight ~ 480 kDa, an outer diameter of 12, nm and an inner diameter of 8 nm, which can contain up to 4500 iron (III) atoms.[118]

In addition, another beneficial feature of apoferritin, which is widely used by researchers in nanomedicine, is due to the ability of the protein cage to dissociate reversibly in response to changes in the environment pH while retaining the therapeutic agent in its cavity.[119] This feature provides the option for apoferritin to encapsulate QDs in

its cavity by changing the environmental conditions. The protein cage can be disassociated to its 24 subunits by lowering the pH to < 3.0, and these subunits can be reassemble to form the cage by increasing the pH to > 5.0, Figure 1.11.[117]

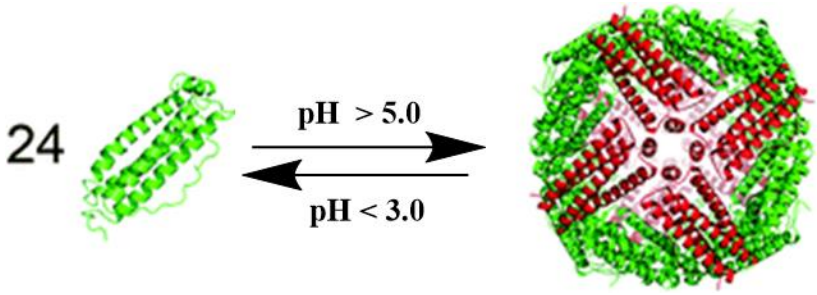


Figure 1.11. Assembling and disassembling of apoferritin cage depends on the pH value.

In addition, apoferritin is stable upon exposure to various denaturants such as urea, sodium hydroxide and guanidinium chloride.[120] These unique features are due to the fact that ferritin contains large numbers of salt bridges and hydrogen bonds that form between its subunits.[121]

One of the interesting properties of apoferritin is the existence of channels between the surface and the interior cage. The six hydrophobic channels are referred to as fourfold channels and their 4 Å diameter is formed by interactions of twelve leucine residues (three from each subunit).[122] The eight hydrophilic channels are referred to as threefold channels and their 3 Å diameter is formed by interactions of the glutamate and aspartate residues in the three N-termini of the AFt subunits (Figure 1.12). These channels have a

negative charge at physiological pH (7.4), which allows them to control the entry and exit of cationic ions into the apoferritin.[95] The threefold and fourfold channels play an essential role in the iron entry and exit in the internal cage. The 3-fold channels essential to load the Fe (II) into the cage while the 4-fold channels are involved in transferring the required oxygen for the ferroxidation.[112]

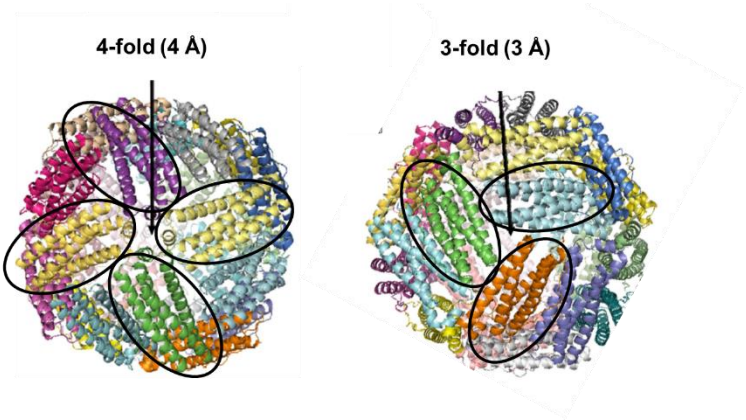


Figure 1.12. Ribbon structure presenting the hydrophilic and hydrophobic channels of human heavy chain ferritin.[122]

1.2.3. Applications of apoferritin in biomedicine

The apoferritin cage is promising as a carrier of nanoparticles and drugs, as it is a native human protein. Therefore, it is biocompatible and is non-immunogenic. The nanoscale size of the protein is also beneficial as it may have a longer circulation half-life and better accumulation in cancer regions.[123] In addition, the interesting properties of the AFt structure mentioned in the previous chapter about the disassembly-reassembly and the channel existence can play significant role in employing the AFt to encapsulate drugs or nanoparticles inside the cage.[124,117]

Furthermore, easy modification of the apoferritin surface either chemically or genetically has potential benefits for the targeting and selection of specific cells.[125] Different molecules can be linked to the apoferritin surface such as dye molecules, peptides and fluorescence quenching molecules to develop the apoferritin use in bioimaging.[126]

The use of drugs or contrast agents in biological applications requires efficient carriers to protect them from degradation and / or release, which might cause side effects.[95] Apoferritin has been used as a bio-template to control the size of the nanoparticle and achieve biocompatible and restricted size nanoparticles.[127] Furthermore, the amount of AFt taken up can be quantified when the cage is loaded with MRI contrast agents, such as gadolinium (III).[95]

Makino *et al.*[128] suggested the use of gadolinium (III) as an MRI contrast agent after its successful encapsulation by apoferritin. The surface of the apoferritin was modified by dextran, which can prolong the time that AFt-Gd (III) is retained in the targeted cells, and can improve clearance from the body, avoiding accumulation in the liver.[128]

Apoferritin modified with manganese has been used to encapsulate gadolinium and prepare a highly sensitive MRI contrast agent to detect hepatocellular carcinoma depending on its uptake by the liver through SCARA5 receptors. [129] When manganese-apoferritin was injected into mice with hepatitis B virus-transgenic and spontaneously developed hepatocellular carcinoma, their liver tissues

were clearly distinguished for the healthy and malignant cells by MRI.[129]

The first use of apoferritin to encapsulate an anticancer drug was published by Simsek *et al*. in 2005.[130] Doxorubicin was encapsulated into the apoferritin cavity by dissociation of the protein into its subunits and reforming the cage in the presence of the doxorubicin by changing the pH of the protein. The apoferritin-doxorubicin complex exhibited non-significant leakage after a few days of storage.[130]

Dostalova *et al.*[131] demonstrated a novel approach to targeting prostate cancer by using an apoferritin cavity to encapsulate doxorubicin. The surface of the apoferritin was modified by using gold nanoparticles and antibodies against specific membrane antigens linked via a specific heptapeptide linker. The functionalised apoferritin-doxorubicin targeted the prostate cancer tissues through the SCARA5 overexpressed receptors. The encapsulation complex was shown to have no effect on the cells comparing to the doxorubicin.[131] In addition, the same nanocage carrier can be used to encapsulate another chemotherapeutic such as daunomycin[132] and curcumin[133], (Figure 1.13).

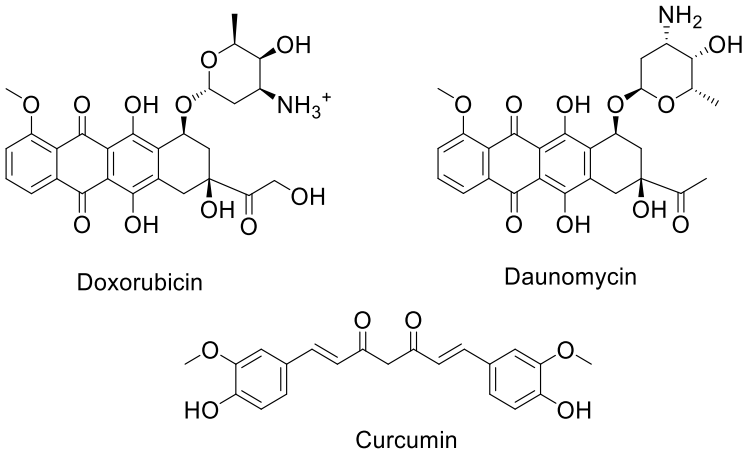


Figure 1.13. Chemical structures of doxorubicin, daunomycin and curcumin.

AFt was also used for encapsulation of nanoparticles, such as gold nanoparticles and semiconductor QDs. Ferritin was used to encapsulate Au nanoparticles to target specific cancer tissues. The localisation of gold nanoclusters into the ferroxidase site in the H-chain apoferritin. This complex showed low cytotoxicity and a high biocompatibility.[134]

Furthermore, PbS QDs can be efficiently encapsulated by apoferritin and was reported by Bradshaw *et al.*[135] to inhibit the growth of colorectal cancer cells. The apoferritin advantage in this study was to increase the biocompatibility of the encapsulated QDs and increase their uptake by the cancer cells. In addition, it reduced the systematic toxicity associated with systemic therapy.[135] Furthermore, apoferritin-PbS QDs were tested on different types of breast cancer cells and showed selective targeting to their receptors.[136]

Apoferritin was introduced for use in photothermal therapy by He *et al.*[137] who developed a composite of CuS-apoferritin-MBA. The CuS

nanoparticles were encapsulated inside the AFt cage with a modified surface containing MBA dye for use in imaging-guided photothermal therapy. This composite was utilized on a tumour bearing mouse. The results showed high uptake of the composite by the cancer cells and it has been suggested this composite can be used in photothermal therapy and bioimaging.[137]

Apoferritin is used to encapsulate photosensitizers so they can be applied in photodynamic therapy (PDT). PDT requires three components, a photosensitizer, radical oxygen and light. The photosensitizer is excited by a specific laser light wavelength to produce reactive oxygen species that are causing cellular death.[138] Apoferritin with a surface modified with the RGD4C peptide motif was used to encapsulate zinc hexadecafluoro-phthalocyanine ($ZnF_{16}Pc$) and the *in vivo* studies showed remarkable anticancer accumulation and growth inhibition.[139]

The developments in nanotechnology have also played important roles in vaccine improvement over the past 10 years. The utilization of nanomolecules in vaccine formulations may lead to improved antigen stability and immunogenicity, selective delivery and slow release properties.[140] Among the different molecules used for this purpose, ferritin, with regards to its uniform structure and the ability to modify its inner and/or outer surface is playing a significant role in vaccine development such as for influenza vaccines.[141]

1.2.4. Affibody

Affinity proteins are valuable candidates in the development of therapeutics and imaging agents. Their ability to selectively bind a known molecular structure with high affinity is important for using them in both *in vitro* and *in vivo*.[142] Until the last decade, antibodies were the most successful and highly used affinity molecules for biological applications. However, their use has some limitations that are summarised in the table below.[143,144]

Table 1.2. Advantages and limitations of using antibodies in targeted biological applications.

Advantages	**Limitations**
Natural proteins generated against many antigens	Large size (~ 150 kDa)
High affinity (nanomolar – picomolar)	Multidomain structure consisting of several peptides cannot be produced heterolopusley in *E. coli*.
Two binding sites (IgG)	Depends on disulfide bonds to stabilize the Y shape structure and the antibody folding
Avidity effect	Low stability at high temperatures
	Difficult and expensive to produce.

Therefore, new alternative affinity protein scaffolds such as single chain fragment variable (scFv), Darpin and affibody have been used

to reduce the limitations of antibodies usage.[145] ScFvs are artificial structure consist of linking the variable regions of heavy (V_H) and light (V_L) chains of the antibody by an un-natural peptide linker, Figure 1.14. The length of the peptide linker could affect the activity of the ScFvs, the short linker prevents the physical association of the two domains while the long linker results in weak association. In addition, scFvs have low solubility in aqueous solutions.[146]

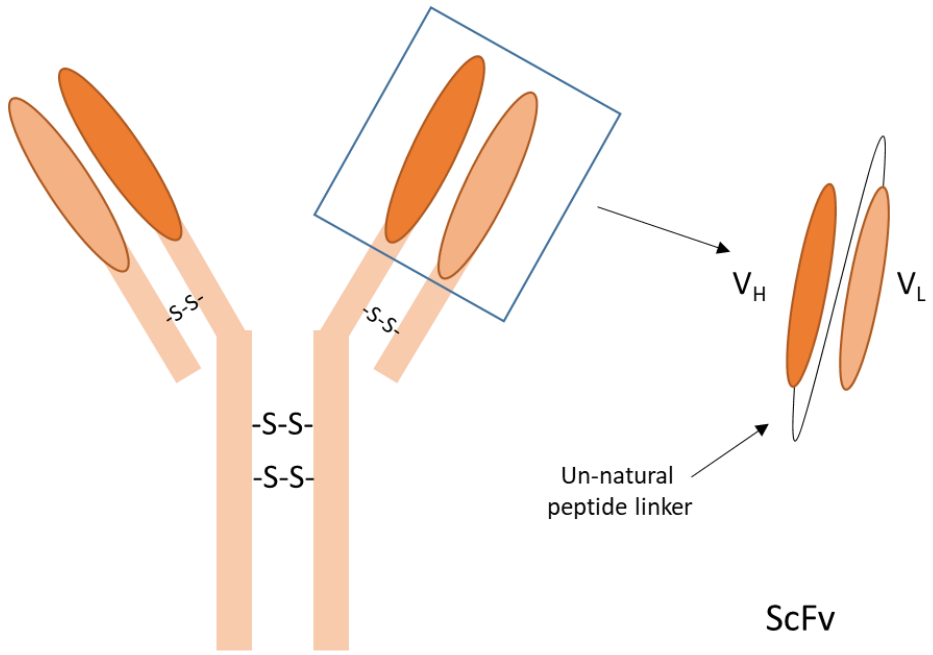


Figure 1.14. A schematic diagram showing antibody and scFv fragment.

Several alternative binding scaffolds, such as darpins, have been developed in recent years to target specific cells. Darpins are formed from Ankyrin repetition, which is the most common protein – protein binding in nature and responsible for cell signalling and receptor binding. Darpins consist of repetition (2 – 4 times) of 7 residues of ankyrin and are produced with a molecular weight ranging from 14 –

18 kDa. Darpins can be expressed heterologously in *E. coli* bacteria and produced in a high concentration with high aqueous solubility.[146]

An affibody molecule is a small protein consisting of 58 amino acids derived from staphylococcal protein A (SPA). Affibodies have molecular weight ~ 6.5 kDa and folded in three helixes as shown in Figure 1.15. Affibody was engineered by the Swedish group of Löfblom *et al.*[143] to overcome the limitation of the antibody usage. An affibody has a single domain, lack of disulfide bond and can be expressed genetically by bacteria in a high quality and quantity.[145,147] Furthermore, affibodies have the ability to combine with other proteins and nanoparticles through their functional groups and improve the signalling and the metabolic pathways in living bodies, therefore, they can be used as a drug carrier to specific cancer cells.[148]

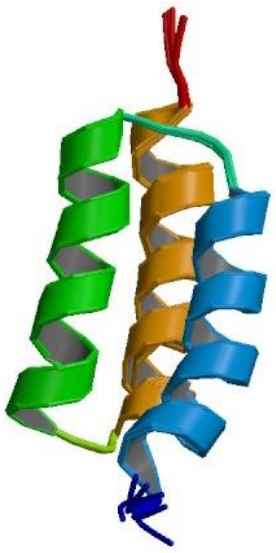


Figure 1.15. Three helix bundles of affibody.[143]

Since the discovery of this affibody, more than 400 studies have been published about the development of other affibodies and their usage in various medical applications such as bioimaging and targeted delivery of toxic molecules.[149] Some studies can be summarised in Figure 1.16.

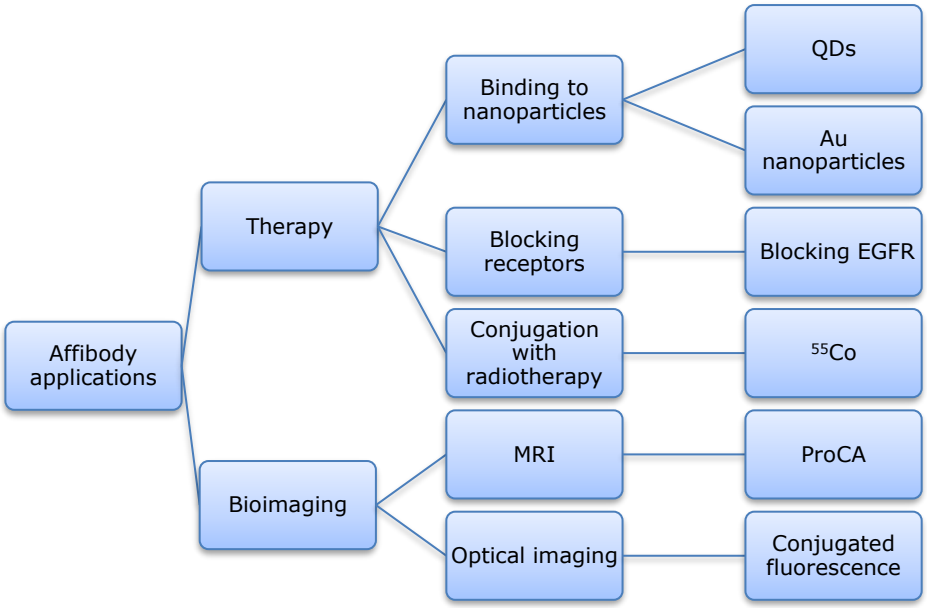


Figure 1.16. A diagram representing the applications of affibodies in biological applications in both therapy and bioimaging with examples of each application.[144]

An affibody has been designed with high affinity to the human epidermal growth factor receptor 2 (HER2), which is overexpressed in several cancers: 9 – 32 % of ovarian cancers, 20 % of breast cancers, and 15 – 30 % of gastric cancers. Therefore, binding between HER2 and the affibody can be utilized for diagnostics and cancer therapy.[150,151]

According to the significant selectivity of the affibody to targeted specific cancer cells receptors, affibodies have been widely used in therapeutic and imaging studies. The combination of the affibody to the nanoparticles such as QDs can be employed in both therapeutic and imaging applications. Gao *et al.*[152] designed two nanoprobes modified with the affibody $Z_{HER2:342}$. InAs/InP/ZnSe QDs core/shell/shell with emission in the NIR region and iron oxide nanoparticles were used in this study. They demonstrated the nanoparticles could be applied for *in vivo* fluorescence imaging and MRI scanning. The study showed significant specificity of the modified nanoparticles towards the HER2 receptors on cancer cells such as MDA-MB-231 breast cancer cells.[152]

In this study, we are using affibody ($Afb_{ZHER2:342}$) fused to the N-terminus of human heavy chain apoferritin (Afb-AFt-) to encapsulate the synthesised PbS QDs and target HER2 receptors overexpressed on SKBR3 breast cancer cells. The encapsulated QDs can be applied for bioimaging of the targeted cancer cells. We expect to see a greater toxic effect of the QDs encapsulated by Afb-AFt- on SKBR3 cells than on MDA-MB-231 cells, demonstrating the selectivity of the Afb-AFt- carrier protein.

1.3. Breast cancer and the role of HER2 receptors

Breast cancer is the most common cancer among women worldwide.[153] More than 1.5 million women are affected by breast cancer each year and around 570,000 women died from breast cancer in 2015 according to the World Health Organisation records,

which is 15 % of the total number of deaths among women with all types of cancer.[154] Different treatments have been used for breast cancer, such as chemotherapy, radiotherapy and surgery.[153] However, these treatments may cause side effects among the healthy cells, and therefore developing chemotherapy with targeted molecules is required to reduce the unwanted side effects.[155]

The human epidermal growth factor receptor (HER) family, which consists of four members (HER1, HER2, HER3 and HER4), plays an important role in the pathogenesis of several human cancers. The HER family controls cell growth, survival and differentiation of the cells.[156] Lack of control of HER receptors can result in many human diseases, cancer being the most common one. The structure of the HER family is related to tyrosine kinase proteins, and all members contain an extracellular ligand binding site, a transmembrane lipophilic domain, and an intracellular protein tyrosine kinase domain.[157]

According to the structure and the function of the HER receptors and their central role in human cancer, they have been proven to be useful as targets for cancer treatments.[158] There are eleven known ligands which can be bind selectively to HER receptors. HER2 has no known ligand. The activation of HER receptors is induced by binding of the ligand to the extracellular domains and then the intracellular segments of the HER receptors undergo homo-dimerization or hetero-dimerization and transphosphorylation.[159] The mechanism of function of HER receptors are strongly dependent on the interaction

between the extracellular domains and the activating ligands of their dimerization partner.[159]

Most of the studies on HER2 have been performed in breast cancer because it has been found to stimulate mammary carcinogenesis *in vitro* and *in vivo*. The HER2 gene is overexpressed in 15 – 30 % of breast cancer cells.[160] Two breast cancer cell lines were used in this study: MDA-MB-231 and SKBR3.

MDA-MB-231 cells are from human breast cancer and were isolated from a pleural effusion in a 51-year-old woman with metastatic breast adenocarcinoma.[161] MDA-MB-231 cells have a spindle-shaped structure and lack expression of HER2 receptors (~ 20 k HER2 per cell), and therefore were selected as a negative control for the HER2 targeting.[162]

SKBR3 is a human breast cancer cell line obtained from a pleural effusion from a 43-year-old woman with breast adenocarcinoma.[161] SKBR3 cells express between 1,000,000 and 3,000,000 HER2 receptors per cell, whereas normal cells express ~ 0 – 1 k HER2 receptors per cell.[162] Therefore, the SKBR3 cell line was selected for use as a positive control in HER2 targeting. In addition, SKBR3 cancer cells are a suitable preclinical model for screening therapies that can target HER2.[163]

1.4. Aims and Objectives

Despite strong interest in optical properties of QDs, their use in bioimaging of deep tissues remains challenging due to the size related toxicity and biocompatibility. The aim of the project was to synthesise biocompatible targeted PbS QDs.

The objectives of this project are as follows:

1. To develop the synthesis of biocompatible PbS QDs with a diameter of d_{QDs} ~ 2–4 nm with stable photoluminescence emission in the first NIR window of the low absorption of biological tissues (700–950 nm).
2. To prepare and characterise pure AFt- and Afb-AFt-- capsules to use as carriers and for targeting certain tissues.
3. To encapsulate the QDs inside the AFt- and Afb-AFt- cages.
4. To study the cytotoxicity of the produced QDs alone and in their encapsulation forms.

In order to achieve biocompatible QDs with optical active emissions, PbS QDs surfaces were passivated with different capping ligands containing thiols. The AFt- capsule was used as a carrier protein to encapsulate PbS QDs and to improve stability, aqueous solubility and biocompatibility of the QDs and to deliver them to specific cancer cells.

Efficient encapsulation was required to obtain QD solution with long term colloidal stability and use the QDs in the *in vitro*. In order to achieve that, different encapsulation routes were used: the pH reassembly, nanoreactor and urea reassembly route.

Determination of the cytotoxicity of the PbS QDs before and after the encapsulation was required to understand the effect of the QDs and to estimate the concentrations that could be used in future *in-vivo* studies. Therefore, MTT assay was used to determine the cell viability and estimate the growth inhibition factors (GI_{50}) values in human derived cell lines.

The development of the targeting proteins was needed to reduce potential side effects and systematic toxicity. Therefore, AFt- capsule with approximately 4 Afb copies on the surface was used to encapsulate the PbS QDs (Figure 1.17). The Affibody-Apoferritin (Afb-AFt-) capsule was used as a QD carrier for targeting of the HER2 receptors.

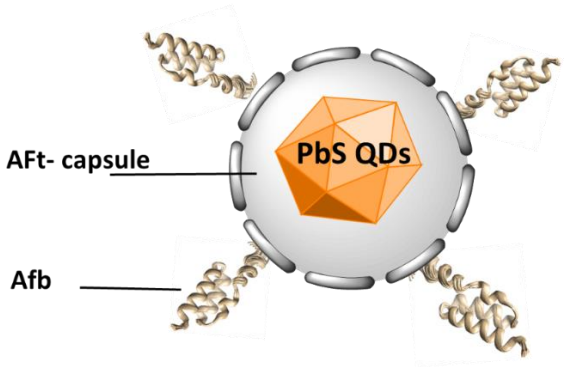


Figure 1.17. Design of Afb-AFt- encapsulated PbS QDs.

The selectivity of the targeted protein, Afb-AFt-, was determined by examining the effect of the encapsulated QDs on two types of breast cancer cells, MDA-MB-231 and SKBR3 as a negative and positive control to HER2 receptors, respectively. The MTT assay was used for the PbS QDs before and after the encapsulation and the GI_{50} values are estimated.

Chapter 2

2. Materials and methods

This chapter includes the procedures and the protocols followed in this study for the synthesis and experimental studies of PbS QDs with different capping ligands; expression and purification of proteins; encapsulation methods and *in vitro* studies of the encapsulated QDs.

2.1. PbS QDs synthesis

Table 2.1. Chemicals used for PbS QDs synthesis

Chemical	Formula/Abbreviation	Company
Lead acetate trihydrate	$Pb(CH_3COO)_2.3H_2O$	Sigma-Aldrich
Sodium sulfide 99%	Na_2S	
Thioglycolic acid 99%	$HSCH_3COOH$ / TGA	
Thioglycerol	$HOCH_3CH(OH)CH_3SH$ / TGL	
Dithioglycerol	$HOCH_3CH(SH)CH_3SH$ / DTG	
L-Cysteine 98%	$HSCH_3CH(NH_2)COOH$ / L-Cys	Acros
Lead (II) nitrate 99%	$Pb(NO_3)_2$	Fluka
L-Cysteine methyl ester hydrochloride	$HSCH_3CH(NH_2)COOCH_3$ / L-CysOMe	Alfa-Aesar
Thioacetamide 98%	$CH_3C(S)NH_2$ / TAA	
Glutathione 99%	GSH	

The chemicals listed in Table 2.1 were used to synthesise the PbS QDs. All chemicals were used as supplied without any further purification.

2.1.1. Thioglycolic acid capped PbS QDs

To synthesise PbS QDs capped with TGA, $Pb(NO_3)_2$, TGA and thioacetamide were used. Following the procedure reported by Martinez-Mancera *et al.*[39], lead(II) nitrate (662 mg, 1.0 mmol) was dissolved in deionized water (20 mL) and filtered using a 0.2 µm syringe filter, then the solution was degassed with nitrogen for 20 min. Thioglycolic acid (0.28 mL, 2.0 mmol) was added to the colourless Pb^{2+} solution and the pH was adjusted to 11.0 by adding triethylamine (~ 0.1 mL). The solution was mixed for 15 minutes under N_2 flow. Thioacetamide (0.1 M) was prepared in deionised water and 2.0 mL, 1.5 mL and 1.0 mL were added to different 5 mL quantities of the Pb-ligand to achieve QDs with Pb:S molar ratios of 1:0.4, 1:0.3 and 1:0.2, respectively. The solutions were degassed with nitrogen under vigorous stirring for 30 min. The synthesised PbS QDs were stored under a nitrogen atmosphere at T = 4 ºC in the dark for further studies.

2.1.2. L-Cysteine capped PbS QDs

To synthesise PbS QDs capped with L-cysteine (L-Cys PbS QDs), lead (II) nitrate, L-cysteine and thioacetamide were used. Lead nitrate (33.1 mg, 1 mmol) was dissolved in deionised water (10 mL) and filtered through a 0.2 µm syringe filter and the solution was degassed

with nitrogen for 20 min. Free L-cysteine (24.2 mg, 2 mmol) was dissolved in deionized water (10 mL) and was added to the $Pb(NO_3)_2$ aqueous solution and the pH was adjusted to 11.5 by addition of NaOH (1 M). The colour changed from white to colourless, and the solution was left stirring for 20 min whilst being degassed with nitrogen. Thioacetamide (0.1 M, 3.0 mL) was added to the solution and the solution was mixed for 5 hours. The solution started to turn brown after ~ 4 h and formed the PbS QDs. The colloidal PbS QDs solution produced had molar ratio of Pb:L-Cys:S = 1:2:0.3 was stored under a nitrogen atmosphere at T = 4 ºC in the dark.

Different Pb:L-Cys molar ratios were used to optimise the synthesis of L-Cys PbS QDs to produce QDs with optical emission in the first NIR window. The QDs were synthesised following the procedure described above. The QDs with molar ratios of L-Cys:Pb of 2.0, 2.2, 2.5 and 3.0 were prepared by the addition of 4.0 mL, 4.4 mL, 5.0 mL and 6.0 mL of L-Cys (0.04 M) to different 4.0 mL aliquots of the $Pb(NO_3)_2$ (0.02 M), respectively. Thioacetamide 0.3 mL was added to each sample to achieve a Pb:S molar ratio of 1:0.3.

Different sulfur molar ratios to Pb^{2+} (0.3–0.9) were used to synthesise L-Cys PbS QDs. L-Cys molar ratios of 2.2 and 2.5 were chosen for the optimisation. Thioacetamide was added with volumes of 0.2 mL, 0.25 mL, 0.3 mL, 0.35 mL, 0.4 mL, 0.45 mL and 0.5 mL to different 5 mL of Pb-L-Cys precursor with Pb:L-Cys molar ratios of 2.2 and 2.5 at pH 11.0 to achieve Pb:S molar ratios of 0.3, 0.4, 0.5, 0.6, 0.7, 0.8 and 0.9, respectively. The solutions were mixed for

5 hours under nitrogen and forming a pale brown solution which were stored under a nitrogen atmosphere at *T* = 4 ºC in the dark.

2.1.3. L-CysOMe PbS QDs

To synthesise L-CysOMe PbS QDs in aqueous solution, $Pb(NO_3)_2$, L-CysOMe and thioacetamide were used. Different L-CysOMe molar ratios to Pb^{2+} (2–6) were used to optimise the synthesis of PbS QDs. Solutions of L-CysOMe (0.05) with volumes of 4.0 mL, 6.0 mL, 8.0 mL, 10.0 mL and 12.0 mL were added to different 5.0 mL aliquots of $Pb(NO_3)_2$ (0.02 M). The pH of each solution was adjusted to 11.0 by adding NaOH (1 M). The solutions were left stirring under nitrogen flow for 15 min. Thioacetamide (0.1 M, 0.3 mL) was added to the Pb-L-CysOMe solutions, to prepare QDs of Pb:S molar ratio of 1:0.3, and left stirring for 5 hours and the solutions' colour changed to brown. Finally, the PbS QDs solutions were stored under a nitrogen atmosphere at *T* = 4 ºC in the dark.

2.1.4. PbS QDs capped with mixed ligands

TGA/L-CysOMe PbS QDs

To synthesise PbS QDs capped with TGA/L-CysOMe, $Pb(NO_3)_2$ (0.02 M), L-CysOMe (0.05 M), thioacetamide (0.1 M) and TGA were used. QDs with Pb:S molar ratio of 1:0.3 were produced with Pb:TGA/L-CysOMe molar ratio of 1:2.5. Different QDs of Pb:TGA:L-CysOMe molar ratio of 1:2.0:0.5, 1:1.5:1 and 1:1:1.5 were achieved by adding 0.014 mL, 0.01 mL or 0.007 mL of TGA with 1.0 mL, 2.0 mL or 3.0 mL of L-CysOMe, respectively, to separate 5.0 mL of $Pb(NO_3)_2$.

The pH of the $Pb(NO_3)_2$ with ligands mixtures were adjusted to 11.0 by adding NaOH (1 M) and they formed colourless solutions of Pb-ligands and were left stirring for 15 min under nitrogen. Thioacetamide (0.3 mL) was added to the mixtures to obtain Pb:S molar ratios of 1:0.3 and left stirring under nitrogen flow for 5 hours and pale brown solutions gradually formed. Finally, the solutions were stored at T = 4 ºC under a nitrogen atmosphere.

TGL/DTG PbS QDs

TGL/DTG PbS QDs were synthesised by following the procedure published by Bakueva *et al*.[164] $Pb(CH_3COO)_2$ (0.016 M) and Na_2S (1 M) were used as sources for Pb^{2+} and S^{2-}, respectively. The synthesis was performed under N_2 at room temperature. $Pb(CH_3COO)_2.3H_2O$ (126 mg, 0.332 mmol) was dissolved in deionised water (20 mL). The TGL (0.17 mL) and DTG (0.07 mL) were added to the Pb^{2+} solution and the pH of the solution was adjusted to 11.0 by adding triethylamine. Colourless solution was formed. Sodium sulfide (0.1 M) was added with volumes of 0.25 mL, 0.42 mL and 0.85 mL to different 5.0 mL aliquots of Pb-ligands precursor solution to synthesise PbS QDs with Pb:S molar ratio of 1:0.3, 1:0.5 and 1:0.7, respectively. The colour of the solutions changed directly from colourless to dark brown. The reaction mixture was stirred for 30 minutes and stored in vials under a nitrogen atmosphere at T = 4 ºC.

2.1.5. GSH PbS QDs

GSH PbS QDs were synthesised by following the procedure published by Nakane *et al.*[165] Lead acetate (3.6 mM), GSH (7.2 mM) and Na_2S (0.05 M) solutions were used in this synthesis. GSH (47.3 mg, 0.16 mmol) was dissolved in 22 mL of deionised water and added to $Pb(CH_3COO)_2.3H_2O$ (30 mg, 0.08 mmol) dissolved in 22 mL of deionised water. The mixture was left stirring for 5 minutes under N_2 in an ice bath. The pH was adjusted to 6.0 by adding ~ 0.1 mL of 1 M NaOH and was left mixing for 5 minutes. Different molar ratios of Pb:S = 1:(0.3, 0.5, 0.8 and 1.0) were produced by adding 0.11 mL, 0.18 mL, 0.29 mL and 0.36 mL of Na_2S (9.7 mg dissolved in 2.5 mL of deionised water) to 10 mL of the Pb-GSH mixture. The colour changed directly to brown. The solution was left stirring for 30 minutes. Also, different pH values were used for the synthesis (6.0, 7.0 and 8.0) to examine the effect of pH on the QDs emission wavelength. The synthesised QDs were stored under a nitrogen atmosphere at T = 4 ºC.

2.2. Optical and morphological characterisation

2.2.1. Photoluminescence measurements

Photoluminescence (PL) measurements were performed using a Horiba Jobin Yvon (HR800) LabRam Setup. The system is equipped with a HeNe laser (λ = 633 nm) with a power of 14 mW. The laser beam reaches the sample through a 50× objective microscope. Two detectors were used with the system, Peltier cooled CCD camera with

a detection range from 200 nm to 1100 nm and liquid nitrogen cooled InGaAs array detector with a detection range from 800 nm to 1600 nm. QDs samples were dropped on a clean glass slide and left to dry at room temperature (~ 2 h), then the PL emission were measured. The principle of the PL measurement has been described in Chapter 1.1.2.

2.2.2. Dynamic Light Scattering (DLS)

A Malvern Nano Zetasizer DLS instrument was used to determine the size and charge of the PbS QDs. A sample with volume (1 mL) was filtered through a syringe filter (0.22 μm) and then loaded in optically translucent disposable plastic cuvette with a path length of 1 cm. The standard operating procedure was used. Each measurement was repeated 3 times to estimate average size and the standard deviation. The data was analysed using Microsoft Excel.

This technique relies on measuring the diffusion speed of the particles or molecules in the samples by illuminating them with He-Ne laser (3 mW, 633 nm). The scattering light intensity fluctuates with time at a specific angle and are detected by a sensitive avalanche photodiode detector (APD). The changes in the intensity of scattered light are analysed with a digital autocorrelator that generates a correlation function. The Stokes-Einstein-equation is used to estimate the particle size:

$$d = \frac{kT}{3\pi\eta D} \qquad (2)$$

Where *d* is hydrodynamic diameter, *k* = 1.38064825 x 10^{-23} J/K is Boltzmann constant, *T* is absolute temperature, *η* is viscosity and *D* is diffusion coefficient.

For surface charge measurements, the same device was used with the zeta potential surface charge cuvettes (Figure 2.1). Each measurement was repeated 3 times.

Zeta potential is determined by measuring the velocity of particles moving towards the electrode with the opposite charge under applied electric field. The velocity (or electrophoretic mobility) determined using laser Doppler velocimetry and applied to the Henry equation to obtain the zeta potential:

$$U_E = \frac{2\varepsilon z f(ka)}{3\eta} \qquad (3)$$

were U_E is electrophoretic mobility, *ε* is dielectric constant, *z is* zeta potential, *ƒ(ka)* is Henry's function and *η* is viscosity.

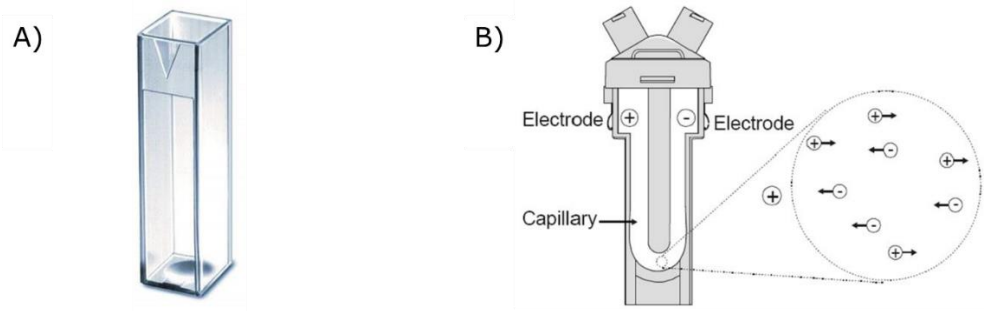


Figure 2.1. A) A plastic cuvette is used to measure the nanoparticle size by DLS and B) A surface zeta potential cuvette is used to measure the surface potential.

2.3. Protein preparations

2.3.1. Transformation of plasmids and protein expression

Escherichia coli BL21 (DE3) cells, were transformed with a designed plasmid to express the AFt- or the Afb-AFt- gene by following the method of Sambrook *et al*.[166] *E. coli* BL21 (DE3) cells (50 µL) were thawed on ice and 5 µL of ~ 150 ng/mL of plasmid DNA, which was designed by Dr Lei Zhang (The University of Nottingham),[167] was added to the bacteria. The plasmid map is presented in Figure 2.2. The cells were incubated on ice for 30 min. A heat shock of the cells was performed for 42 seconds at 42 ºC to get a high transformation efficiency. The cells were then incubated on ice for 5 min. Luria-Bertani (LB) broth 500 µL was added and the cells were incubated at 37 ºC for 60 min, shaking at 180 rpm. Then, 25 µL of the *E. coli* cells were spread on a Petri dish that contained LB agar with the resistant antibiotic (either 100 µg/mL ampicillin or 50 µg/mL kanamycin) and incubated overnight at 37 ºC. For LOBSTR (low background strain) cells, the procedure above was performed to express Afb-AFt-, and chloramphenicol (25 µg/mL) was added along with kanamycin to the plate.

Table 2.2. *E. coli* strains used to express the proteins, with their genotype.

Bacterial Strain	Description / Genotype Protein	Source
BL21 (DE3)	Protein expression strain F-, ompT, hsdSβ(rβ-mβ-), dcm, gal, (DE3) tonA	Invitrogen

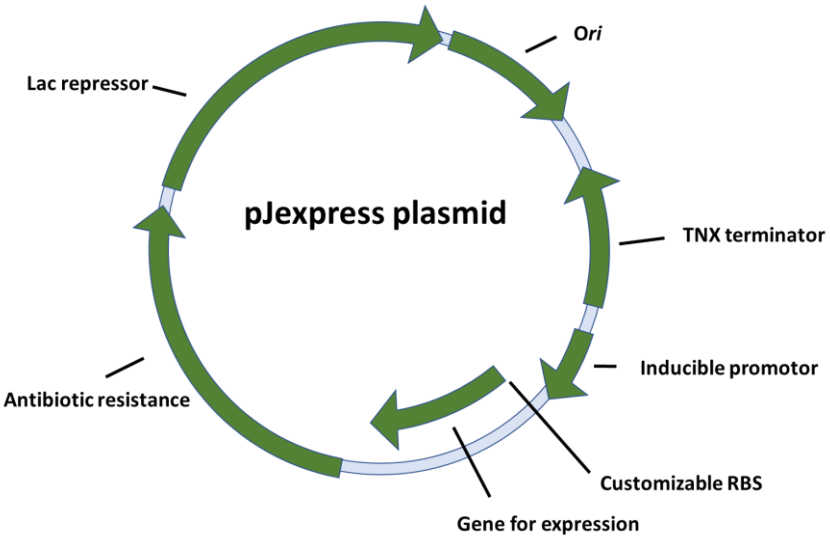


Figure 2.2. Plasmid map of pJexpress vector which was used to design the proteins. The inducible promoter is T7 promoter. *Ori* is origin of replication. RBS is ribosome binding site.

In order to prepare 1 mL of glycerol stock bacteria, a single colony of *E. coli* cells from the Petri dish was added to 10 mL of LB media with the resistant antibiotic (either 100 µg/mL ampicillin or 50 µg/mL kanamycin). Then, the culture was incubated overnight at 37 ºC, shaking at 180 rpm. The bacterial suspension was centrifuged at 4000 x *g* for 10 min. Finally, the media was removed, and the

bacteria were suspended in 50% (v/v) glycerol. The glycerol stock bacteria was stored at T = – 80 ºC.

To express the protein, a small starting culture from the glycerol stock bacteria was grown in 10 mL of LB broth media with 10 µL of the antibiotic the resistant antibiotic (either 100 µg/mL ampicillin or 50 µg/mL kanamycin). Then, the culture was incubated at 37 ºC, shaking at 180 rpm overnight. Then the small culture was transferred to the large scale culture.

The large scale of LB broth media (1 L) was used to express large amounts of protein. Antibiotics (ampicillin 100 mg/mL or kanamycin 50 mg/mL) (1 mL) were added to the media and the small culture was added to the large one. The culture was incubated for ~ 3 hours, shaking at 180 rpm until the optical density (OD) reached 0.6 as measured by UV-Vis spectroscopy at λ = 595 nm. Isopropyl β-D-1-thiogalactopyranoside (IPTG) 1 mL, with a final concentration of 1 mM, was added to the culture and the culture was incubated for 4 hours at 37 ºC, 180 rpm or overnight at 30 ºC. The culture was centrifuged at 4000 x g for 25 min to separate the cells from the supernatant. The supernatant was discarded, and the precipitated cells were dissolved in ~ 35 mL of buffer (20 mM Tris, 10 mM imidazole, pH 8.8). The collected pellet was frozen and stored at T = - 80 ºC.

2.3.1. Sodium dodecyl sulphate polyacrylamide gel electrophoresis

Discontinuous denaturing SDS gels were prepared with 5 % (w/v) stacking gel and 15 % (w/v) resolving gel (Table 2.3). Solutions of 30 µL of the purified protein were mixed with 10 µL of SDS loading buffer (Table 2.4), boiled at 90 ºC for 10 min, then 10 µL was loaded onto the gel. Molecular weight marker (ThermoFisher) was run on the gel to give bands ranged from 11 kDa to 260 kDa. Running SDS buffer (Table 2.4) was used, and a voltage of 180 V was applied across the gel for ~ 2 h. The gel was stained with GelCode™ Blue Stain Reagent (ThermoFisher) for 30 min with shaking, then the gel was de-stained using distilled water 3-times until the stain was removed from the background. An image was taken of each gel by using the Geneflow gel imaging system.

Table 2.3. Compositions of stacking and resolving SDS PAGE.

Composition	**5% (w/v) Stacking gel (mL)**	**15% (w/v) Resolving gel (mL)**
dH_2O	3.4	3.4
30% (w/v) acrylamide	0.83	7.5
1.5 M Tris pH 8.8	0.63 (1 M)	3.8
10% (w/v) SDS	0.05	0.15
10% (w/w) APS	0.05	0.15
TEMED	0.005	0.006

Table 2.4. Loading and running buffers for SDS PAGE.

Loading buffer	200 mM Tris-HCl pH 6.8 1 M DTT 8% (w/v) SDS 0.1% (w/v) bromophenol blue 50% (v/v) glycerol
Running buffer	25 mM Tris base pH 8.8 250 mM glycine 0.1% (w/v) SDS

2.3.1. Polyacrylamide gel electrophoresis of native proteins

Native PAGE gels were prepared with 4 % (w/v) stacking and 6 % (w/v) resolving gels (Table 2.5). Samples of 30 µL protein were mixed with 10 µL of loading buffer (Table 2.6). A running buffer without SDS (Table 2.6) was used and a voltage of 120 V was applied across the gel (10 cm X 10 cm X 1.0 mm) for ~ 3 h. Gels were stained, de-stained and imaged as described for SDS PAGE (Chapter 2.3.1).

Table 2.5. Compositions of stacking and resolving native PAGE.

Compositions	4% (w/v) Stacking gel (mL)	6% (w/v) Resolving gel (mL)
dH_2O	2.88	6.66
30% (w/v) acrylamide	0.5	2
1.5 Tris pH 8.8	0.94	3
10% (w/w) APS	0.06	0.15
TEMED	0.006	0.015

Table 2.6. Loading and running buffer for native PAGE.

Loading buffer	50 mM Tris-HCl pH 6.8 100 mM DTT 50% (v/v) glycerol 0.1% (w/v) bromophenol blue
Running buffer	25 mM Tris base 200 mM glycine

2.3.2. Nickel-immobilised metal ion affinity chromatography

The proteins were designed with a hexa-histidine tag (His-tag) at its N-termini, which has an affinity to chelate metal ions and therefore the Nickel-immobilised metal ion affinity chromatography (Ni-IMAC) technique was used for the purification. Ni-IMAC, a pre-packed 5 mL column of HiTRAP chelating HP affinity resin (GE Healthcare Life Sciences) with the ÄKTA prime system (GE Healthcare Life Sciences, Amersham), was used for Ni-IMAC purification. This column was

charged with 50 mM nickel sulfate ($NiSO_4$), then the column was washed with 30 mL water and binding buffer (20 mM Tris, 10 mM imidazole, pH 8.8) for the soluble proteins and with the addition of 8 M of urea for non-soluble proteins before loading the crude protein. When the lysate was loaded, the absorbance at λ = 280 nm increased and the flow through was collected and checked by sodium dodecyl sulfate polyacrylamide gel electrophoresis (SDS-PAGE). When all of the proteins had been loaded on the column, the column was washed with the binding buffer until it reached the baseline, which means all proteins without a His-tag were eluted from the column. To elute the targeted protein, elution buffer containing 1.5 M imidazole was added. After the collection of the protein, the column was washed with the binding buffer and then with water.

2.3.3. Size Exclusion Chromatography

Size exclusion chromatography (SEC) chromatography is a separation technique that depends on the differences in the size and shape of the molecules. A separation column with gel particles or a porous matrix is in equilibrium with the mobile phase of the molecules that need to be separated. The molecules move through the separation column and the separation is performed via the pores of the gel. Fractions with a low molecular weight or smaller size move slower than the large molecules through the column, i.e. the large molecules passes the column first.[168]

After the Ni-IMAC, the protein was further purified using SEC. The column Hiload 26/600 Superdex 200 pg was used. The column was

left overnight to be charged with binding buffer (20 mM Tris pH 8.3, 50 mM NaCl) then the protein was loaded onto the column. The binding buffer was loaded again through the column and the fractions with high absorbance were collected and run on SDS PAGE.

2.3.4. Ammonium sulfate precipitation

Ammonium sulfate precipitation was used for purifying and concentrating the proteins. This method depends on 'salting out', i.e. decreasing the solubility of the protein by addition of high concentration of salt: high concentration of salts leads to a loss of the correct folding of the protein and loss of the hydration layer.[169] However, small proteins and peptides require a higher concentration of salt to be added than large protein molecules, and therefore this method can be used to purify the larger proteins from the smaller ones. In addition, it can be used to increase the concentration of the protein because the volume of the buffer used to re-dissolve the precipitated protein can be controlled.

A series of protein samples were prepared with 10% – 70% of 100% (v/v) saturated ammonium sulfate (10 µL of ammonium sulfate was mixed with 90 µL of protein, 20 µL of ammonium sulfate was mixed with 80 µL of protein, etc.). Samples were centrifuged at 13000 rpm for 10 min and the soluble and insoluble fractions were separated. Insoluble fractions were dissolved in 100 µL of buffer (20 mM Tris, 8 M urea). SDS PAGE was run for all soluble and insoluble fractions to identify the purest fraction.

2.3.5. Protein concentration measurements

To determine the concentration of the purified proteins two methods were used, nanodrop and Bradford assay. Nanodrop ND-1000 UV spectrometry was used to measure the absorbance of protein at 280 nm. The concentration of protein was calculated using the Beer-Lambert law, where $A = \varepsilon c l$ (where A is the absorbance, ε is the extinction coefficient, which is determined theoretically by the ExPASy website based on the amino acid sequences of the proteins, c is the concentration, and l is the path length).

For the Bradford assay, a standard calibration curve was constructed by measuring a series of BSA samples with known concentrations (0.1, 0.2, 0.4, 0.8 and 1.0 mg/mL). A 96 well plate was used to mix each 10 µL of BSA with 140 µL of Bradford reagent per well. Then, the absorbance of the complex formed between the Bradford reagent and the protein was measured at 595 nm using a microtiter plate reader (PerkinElmer Precisely-Envision 2104 multilabel reader). Each sample was measured 3 times and the average absorbance was plotted against the concentrations in Excel. The linear fit was used to determine the concentration of the unknown samples.

Protein samples were prepared following the procedure used for the BSA: 10 µL of protein with 140 µL of Bradford reagent. The protein concentration was calculated using the BSA standard curve.

2.3.6. Matrix Assisted Laser Desorption/Ionisation Time- of-Flight mass spectrometry

The molecular weights of the protein samples were determined using Bruker Matrix Assisted Laser Desorption/Ionisation Time-of-Flight (MALDI-TOF) mass spectrometry. The samples were prepared by mixing 5 µL of the protein with 10 µL of saturated sinapic acid (sinapic acid was dissolved in a solvent of 1:2 acetonitrile + 0.1% (v/v) trifluoroacetic acid). The samples were loaded onto the plate and dried at room temperature. The spectrum was determined according to the LP-44 kDa method and was analysed using flexControl (Ultraflex) Ver 3.0 software and the molecular weight of the protein was determined

2.3.7. Purification of AFt-, Afb and Afb-AFt-

Purification of apoferritin and affibody

To purify the AFt- and Afb, the phenylmethylsulfonyl fluoride (PMSF) was added to a final concentration of 0.5 mM. (Chapter 2.3.1). Then the pellet was sonicated (20 kHz, probe 6 mm) on ice for 10 min (1 min on and 1 min off), followed by centrifugation at 40000 x *g* for 25 min. The soluble fraction was collected for purification and the non-soluble pellet was discarded.

An ÄKTA prime system (GE Healthcare Life Sciences, Amersham), was used to purify the apoferritin. The ÄKTA was washed with 40 mL of degassed deionised water to remove the ethanol. Buffer A (Table 2.7) ~ 15 mL was loaded, and a Nickel column was connected to the

ÄKTA and washed with buffer A. Crude protein was loaded into the ÄKTA, and when the conductivity was increasing the waste solution was collected. After all protein was finished, buffer A was loaded into the ÄKTA until the conductivity reached the baseline (< 0.01). Next, protein chelates to the column was eluted using a gradient of increasing imidazole concentration (buffer B, Table 2.7) the eluted protein was analysed using an SDS PAGE. The collected protein was dialysed twice against 20 mM Tris pH 8.8 for at least 4 hours. The concentration was measured as described in Chapter 2.3.5, and the protein was snap frozen in liquid N_2 and stored at T = - 80 ºC.

Table 2.7. Composition of buffers A, B, C and D.

Buffer A	20 mM Tris, 10 mM imidazole pH 8.8
Buffer B	20 mM Tris, 1.5 M imidazole pH 8.8
Buffer C	20 mM Tris, 4 M urea and 10 mM imidazole pH 8.8
Buffer D	20 mM Tris, 4 M urea and 1.5 M imidazole pH 8.8

Purification of Affibody-Apoferritin

Afb-AFt- was expressed in and purified from *E. coli* BL21 (DE3) bacteria. The protein was purified from the non-soluble fraction by Ni-IMAC. PMSF was added to a final concertation of 0.5 mM and the pellet was sonicated (20 kHz, probe 6 mm) in ice for 10 minutes (1 min on - 1 min off). The sonicated pellet was centrifuged at 30000 x *g* for 25 minutes. The soluble fraction was run on SDS PAGE while the non-soluble fraction was dissolved in buffer C (Table 2.7) and

centrifuged at 40000 x *g* for 10 minutes. The solution was filtered using a 0.45 µm syringe filter before being loaded to the Ni column. To elute the protein, buffer D (Table 2.7) was used and the protein was eluted between 40 – 50 % of mixing buffers C/D. The protein was collected in 7 mL fractions and these fractions were run on SDS PAGE to confirm their molecular weight and purity. After the purification, Afb-AFt- was collected and dialysed against 20 mM Tris at pH 10.3 twice for at least 4 hours each time. Finally, the protein concentration was measured using Nanodrop at 280 nm as described in Chapter (2.3.5). The protein was snap frozen in liquid N_2 and stored at T =− 80 ºC.

2.3.8. Preparation of affibody-apoferritin with an average of 4 copies of affibody on the surface

To prepare Afb-AFt- with an average of 4 copies of affibody on the surface, AFt- and Afb-AFt- were used. Both proteins were dialysed against 0.15 M NaCl at pH 2.0 for 4 hours to disassemble the proteins. Molar ratio of 20:4 of AFt-:Afb-AFt- was used to achieve approximately 20 polypeptide subunits of AFt- and 4 polypeptide subunits of Afb-AFt- per protein capsule. NaOH (5 M) was added to increase the pH to ~ 9.0 to ensure all subunits were reassembled. The protein was dialysed against 2 L of 20 mM Tris at pH 8.8, and then was run on a native gel and compared with the native AFt- cage to determine the cage formation. The concentration of the protein was determined by Bradford assay. The protein was snap frozen in liquid N_2 and stored at T = – 80 ºC.

2.3.9. Improving the purity of the Afb-AFt-

To improve the purity of the Afb-AFt-, the expression and purification methods were optimised, and the following criteria were used for the final protein expression and purification.

1) LOBSTR cell

The plasmid DNA of the Afb-AFt- was transformed into LOBSTR cells, which are derived from the *E. coli* strain BL21 (DE3) and carries gnomically modified copies of arnA and slyD. Proteins arnA and slyD are the most common *E. coli* contaminants and contain multiple histidine tag, which can attach to the Ni column and can be purified with the targeted protein [170] After the transformation, a glycerol stock of LOBSTR cells expressing the Afb-AFt- plasmid was prepared using the same procedure described in Chapter 2.3.1. Additionally, the temperature of the induction was changed to 25 ºC.

2) Temperature of the induction

In order to reduce the aggregation and the degradation of the desired protein, the temperature of the induction was reduced. Lowering the temperature of the induction leads to a reduced rate of transcription, translation, cell division, and also protein aggregation and degradation. Therefore, after the addition of IPTG to the large-scale expression of Afb-AFt-, the temperature of the incubation was reduced to 20 ºC instead of the usual 30 ºC to slow the protein expression and can results in a reduction in the degradation of proteolytically sensitive proteins.

3) Concentration of IPTG

Lower concentration of IPTG was used to reduce the rate of the protein induction and produce a purer protein. Total concentration of IPTG of 0.8 mM was used instead of 1 mM to express the protein. The same conditions were used to purify the protein from the non-soluble fraction.

4) M9 mineral medium

Table 2.8. Composition of M9 mineral medium in 1 L

Sterile water
M9 salt solution Na_2HPO_4 (3.37 mM) KH_2PO_4 (2.20 mM) NH_4Cl (0.935 mM) NaCl (0.855 mM)
0.4% (w/v) Glucose
1 mM $MgSO_4.7H_2O$
0.3 mM $CaCl_2.2H_2O$
Biotin (10 µg/mL) Thiamine.HCl (10 µg/mL)
Trace elements solution (100×) EDTA (0.134 mM) $FeCl_3.6H_2O$ (0.031 mM) $ZnCl_2$ (6.2 µM) $CuCl_2.2H_2O$ (0.76 µM) CoCl2.6H2O (0.42 µM) H_3BO_3 (0.162 µM) $MnCl_2.4H_2O$ (0.081 µM)

M9 mineral medium was used to grow the bacteria instead of LB broth. This medium is composed of the minimal nutritional requirements for bacteria to grow. The M9 medium is used to reduce the speed of growth of bacteria and slower the protein expression, permitting the protein to fold correctly. The mineral medium was prepared with composition summarised in the Table 2.8.

5) Imidazole concentration in buffer A

As mentioned in the Chapter 2.3.1, during purification based on the His-tag, the concentration of imidazole in the binding buffer (buffer A) was increased from 10 mM to 40 mM. The increasing of the imidazole could help to elute protein fragments with low number of histidine, which could chelate the Ni ions in the column.

6) Concentration of urea

In order to dissolve the non-soluble fraction of the crude protein, buffer with urea (8.0 M) was used. The high concentration of urea might have caused degradation of the protein; therefore, the concentration of urea was reduced to 4.0 M in both buffers A and B, which was found to solubilise the protein. The SDS PAGE was used to assess the purity and the molecular weight of the protein, confirming that no degradation of protein was incurred.

2.3.10. Western blot

The western blot technique is widely used to detect and analyse proteins depending on their ability to bind to specific antibodies. A

western blot is electrically transferring the protein from the SDS gel to a solid supporting nitrocellulose membrane. The transferred proteins are able to bind to primary antibody to target a specific region such as His-tag. Secondary antibody labelled with enzyme are covalently bind to the primary antibody and produce a coloured reaction which can be characterised and imaged.

The western blot technique was performed to identify the purified proteins with their histidine tag. The principles of a western blot are dependent on the primary antibody that is used in the procedure. The transfer buffer used has a composition of 25 mM Tris, 192 mM glycine, 0.038 % (w/v) SDS and 20 % (v/v) methanol. The TBS-T solution has a composition (20 mM Tris pH 7.6, NaCl 137 mM and 0.05 % (v/v) Tween-20) and 10 % (w/v) non-fat milk (5 g non-fat powder milk in 50 mL TBS-T).

First, two SDS PAGEs were run with the same proteins (AFt-, positive control, BSA) to compare to the western blot image. BSA was used as negative control. Then, 8 filter papers and one nitrocellulose membrane were soaked in the transfer buffer for 30 min in two lots (4 filter papers each, one of them with the membrane). After the SDS gels running was finished, one gel was subjected to staining and the other was transferred to the membrane.

In the transfer machine compartment, 4 filter papers with the nitrocellulose membrane on top were inserted and any air bubbles were removed. The gel was gently laid on the membrane and covered with the other 4 filter papers. The proteins were transferred from the

gel to the membrane using the transfer machine. After the transferring was finished, the membrane was incubated with 8 mL of milk solution in a sealed plastic bag at room temperature for 1 hour. The milk was discarded, and the membrane was incubated at 4 ºC overnight in 1 mL of a mixture of milk and primary antibody (mouse anti-tetra His antibody) with ratio of antibody:milk = 1:1000.

The next day, the solution of milk and antibody was removed, and the membrane was washed with TBS-T solution three times for 5 min each. Then, the membrane was incubated with 8 mL of a mixture of secondary antibody (anti-mouse horseradish peroxidase conjugate antibody) and milk (2 µL antibody with 8 mL milk) in a new plastic bag for 1 hour at room temperature. The membrane was washed with TBS-T solution three times for 5 min each.

Finally, ECL reagents were warmed to room temperature and mixed in a ratio of 1:1 (0.5 mL each) and added to the membrane for 5 min. The membrane was placed on the reader and covered with the ECL solutions before scanning on high sensitivity.

2.4. PbS QDs encapsulation by AFt- and Afb-AFt-

Reassembly methods were used to encapsulate the PbS QDs. AFt- and Afb-AFt- with an average of 4 affibody copies were used to encapsulate PbS QDs (Table 2.9). Two routes of reassembly were performed, pH reassembly and urea reassembly.

pH reassembly is dependent on decreasing the pH of AFt- and Afb-AFt- to 2.0 to disassemble the proteins before adding them to the

QDs while the urea method is dependent on disassembling the protein by using 8.0 M urea.

AFt- and Afb-AFt- were prepared by dialysis against 1 L of 0.15 M sodium chloride (NaCl) solution and the pH was adjusted by adding NaOH.

The urea route was performed by adding 8 M urea with a volume equal to the volume of the AFt- or Afb-AFt- and mixing at 4 ºC for 2 hours before mixed with the PbS QDs. After the mixing of the protein and the QDs the urea was removed by dialysis of the encapsulation solution against 2 L of 20 mM Tris buffer at pH 8.8.

Table 2.9. List of QDs encapsulated with proteins and the method that was followed

PbS QDs	Pb:S molar ratio	pH method	Urea method
L-Cys	1:0.3	AFt-	AFt-
	1:0.8	Aft-	AFt-
L-CysOMe	1:0.3	AFt-	AFt-
TGA/L-CysOMe	1:0.3	AFt-	AFt-
		Afb-AFt-	X
GSH	1:0.5	AFt-	AFt-
		Afb-AFt-	X

The nanoreactor routes was used to synthesise PbS QDs inside the AFt- cage. Pb-L precursor at pH 10.0 was added to AFt- at pH 6.0.

Then, S^{2-} source was added slowly under vigorous stirring and left for 30 min stirring. The final solution was dialysed against 20 mM Tris at pH 8.8 to remove the excess of the ions n the solution.

2.4.1. L-Cys PbS QDs

AFt- (7.2 mg/mL, 4.0 mL) was added slowly to L-Cys PbS QDs (2 mg/mL, 1.0 mL) with molar ratio of Pb:L-Cys:S = 1:2.5:0.8 under vigorous stirring. The pH was adjusted to (9.0 - 10.0) by adding (1 M) NaOH, (each 1 mL protein required ~ 0.01 mL NaOH). The AFt-PbS encapsulation solution was left stirring for 30 min under N_2 flow. The encapsulation solution was dialysed twice against 2 L of 20 mM Tris at pH 8.8 for at least 4 h for each. Finally, the encapsulated PbS QDs were stored in a vial under a N_2 atmosphere at 4 ºC in the dark.

2.4.2. L-CysOMe PbS QDs

AFt- (3 mg/mL, 3.2 mL) was added slowly to L-CysOMe PbS QDs (1.5 mg/mL, 1.0 mL) with molar ratio of Pb:L-Cys:S = 1:6:0.3 under vigorous stirring. The same procedure described in Chapter 2.4.1 was followed for the encapsulation.

2.4.3. TGA/L-CysOMe PbS QDs

AFt- (12.7 mg/mL, 3.7 mL) was added slowly to TGA/L-CysOMe PbS QDs (3 mg/mL, 2.1 mL) with molar ratio of Pb:TGA:L-CysOMe:S = 1:1.5:1:0.3 under vigorous stirring. The same procedure described in Chapter 2.4.1 was followed for the encapsulation.

For the encapsulation into Afb-AFt-, protein (7.2 mg/mL, 6.8 mL) was added slowly to the PbS QDs (3 mg/mL, 3.7 mL) under vigorous stirring. The same procedure described in Chapter 2.4.1 was followed for the encapsulation.

2.4.4. GSH PbS QDs

AFt- (7.2 mg/mL, 6.5 mL) was added slowly to GSH PbS QDs (2.7 mg/mL, 1.5 mL) with molar ratio of Pb:GSH:S = 1:2.0:0.5 under vigorous stirring. The encapsulation was performed using an ice bath and the pH was kept ~ 6.5 using (1 M) NaOH. The same procedure described in Chapter 2.4.1 was followed to complete the encapsulation

The urea reassembly method was applied by mixing AFt- (7.2 mg/mL, 3.25 mL) with (3.5 mL) of 8 M urea for 2 h at 4 ºC. The AFt- was added slowly to GSH PbS QDs (2.7 mg/mL, 0.75 mL) under vigorous stirring. The same procedure above was followed to complete the encapsulation.

For the encapsulation into Afb-AFt-, protein (7.2 mg/mL, 4.4 mL) was added slowly to the PbS QDs (2.7 mg/mL, 0.5 mL) under vigorous stirring. The encapsulation was performed using an ice bath. The same procedure described in Chapter 2.4.1 was followed for the encapsulation.

2.5. *In vitro* studies

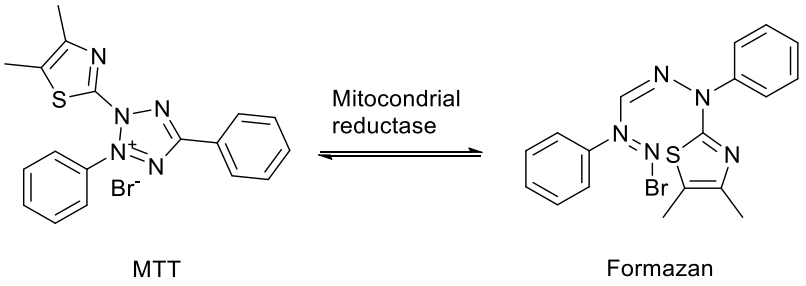
Two human-derived breast cancer cell lines were used in this study, MDA-MB-231 and SKBR3. Both cell lines were obtained from ATCC®, and maintained in RPMI-1640 medium containing 10 % (v/v) fetal bovine serum (FBS), 1 % (v/v) penicillin at 37 °C with 5 % (v/v) CO_2.

2.5.1. Subculturing cell lines

The cells were subcultured when their confluency reached approximately 70 – 80 %. The medium was removed from the flask and the cells were washed with 5 mL of PBS buffer. Then 1 mL of 1× trypsin-EDTA solution was added to the flask and incubated for ~ 5 – 7 minutes at 37 ºC, 5 % CO_2 until the cells detached. Then, 5 mL of RPMI 1640 (Sigma) fresh medium was added to re-suspend the detached cells. An aliquot (0.5 – 1.0 mL) of the re-suspended cells was added to fresh media in a new flask. The remaining cells were used for *in vitro* studies.

2.5.2. MTT assay

3-(4,5-Dimethylthiazol-2-yl)-2,5-diphenyltetrazolium bromide (MTT) assays were performed to determine the cell viability by measuring the optical density of the purple formazan solution that results from the conversion of the tetrazolium salt of MTT into formazan crystals through the mitochondrial hydrogenases of viable cells (Scheme 2.1). The formed formazan crystals are solubilised and absorbance is measured.[171]



Scheme 2.1. Mitochondrial reduction of MTT to formazan.

The detached cells from the flask were re-suspended gently and the cells were counted using a haemocytometer. The cells were mixed with RPMI 1640 medium that contained 1 % (w/v) L-glutamine and 10 % (w/v) foetal bovine serum (FBS) and seeded into a 96-well plate at a density of approximately 3×10^3 cells in 180 µL of medium per well. The wells at the edges of the plate were filled with 250 µL of the medium only, to reduce the evaporation from the experimental wells. The cells were allowed to adhere for 24 hours before the treatment. An additional plate was also set up to determine the absorbance at the time of the treatment (T-zero).

To study cytotoxicity, serial dilutions of PbS QDs, AFt-PbS QDs, Afb-AFt- PbS QDs and the proteins alone were prepared in RPMI-1640 medium with concentrations listed in Table 2.10.

Table 2.10. Concentrations of PbS QDs and proteins used for the treatments with equivalent proteins measured in mg/mL.

PbS QDs (mg/mL)	AFt-QDs (mg/mL)		Afb-AFt-QDs (mg/mL)		AFt- (mg/mL)	Afb-AFt- (mg/mL)
	QDs	AFt-	QDs	Afb-AFt-		
0.001	0.001	0.0072	0.001	0.0077	0.0072	0.0077
0.01	0.01	0.072	0.01	0.077	0.072	0.077
0.05	0.05	0.36	0.05	0.385	0.36	0.385
0.1	0.1	0.72	0.1	0.77	0.72	0.77
0.2	0.2	1.44	0.2	1.54	1.44	1.54

All agents with volume (20 µL) were added per well to achieve the targeted concentration in 200 µL total volume. One column of wells was left without treatment, 20 µL of medium was added to achieve the same 200 µL volume and was used as a control. The plates were incubated for 72 hours at 37 ºC in an atmosphere of 5 % CO_2. Following treatment, 50 µL of MTT solution (2 mg/mL MTT prepared in PBS buffer) was added to each well and incubated for 3 hours at 37 ºC. Finally, the medium with the MTT solution was aspirated from each well and 150 µL of DMSO was added to dissolve the formazan crystals. The plates were shaken for 5 minutes using a plate shaker (Amersham) to ensure complete formazan solubilisation. The absorbance of the formazan was measured with a microplate reader (EU Vision 2104 multilabel reader) at 550 nm. The data were plotted

by Graph Pad Prism. The growth inhibition factor GI_{50} values were calculated using the equations (4 – 5):

$$A_{GI50} = \frac{A_0 - A_{T-0}}{2} + A_{T-0} \qquad (4)$$

$$GI_{50} = \left(\frac{A_1 - A_{GI50}}{A_1 - A_2}\right)(C_1 - C_2) + C_2 \qquad (5)$$

were A_{GI50} is absorbance of GI_{50}, A_0 is absorbance of control, A_{T-0} is absorbance of T-zero, A_1 is highest absorbance where GI_{50} falls, A_2 is lowest absorbance where GI_{50} falls, C_1 is highest concentration where GI_{50} falls and C_2 is lowest concentration where GI_{50} falls.

Chapter 3

3. Synthesis of PbS QDs with different capping ligands

3.1. Introduction

PbS QDs with optical emission in the NIR window are promising for biological applications due to the low absorbance by biological tissues in this wavelength region. In addition, water soluble QDs with high quantum yield are needed for biological applications. However, to achieve these properties, QDs need to be prepared in aqueous solutions with controlled size giving narrow emission.

Previously, QDs were successfully prepared in organic solvents;[13] however, organic solvents limit the usage of QDs for biological applications due to their hydrophobicity. Therefore, modifications of the surface of the QDs by using capping ligands was necessary to increase their hydrophilicity and increase the solubility in aqueous solutions.

Aqueous PbS QDs were prepared by a ligand exchange method.[58] The QDs were formed first with an oleic acid capping ligand and then the oleate was exchanged with a water soluble ligand, such as L-Cys or dihydrolipoic acid (DHLA).[172] Direct synthesis of PbS QDs in aqueous solution was achieved by using hydrophilic ligands to modify the surface of the QDs. Ligands containing thiol groups were used to achieve this.[173]

In this study, PbS QDs capped with different ligands were synthesised in different compositions molar ratios and pH values to produce bright, optically active, stable and reproducible PbS QDs. L-cysteine (L-Cys), L-cysteine methyl ester (L-CysOMe), thioglycolic acid (TGA), glutathione (GSH) and mixed ligands were used for the synthesis in aqueous solutions (Figure 3.1).

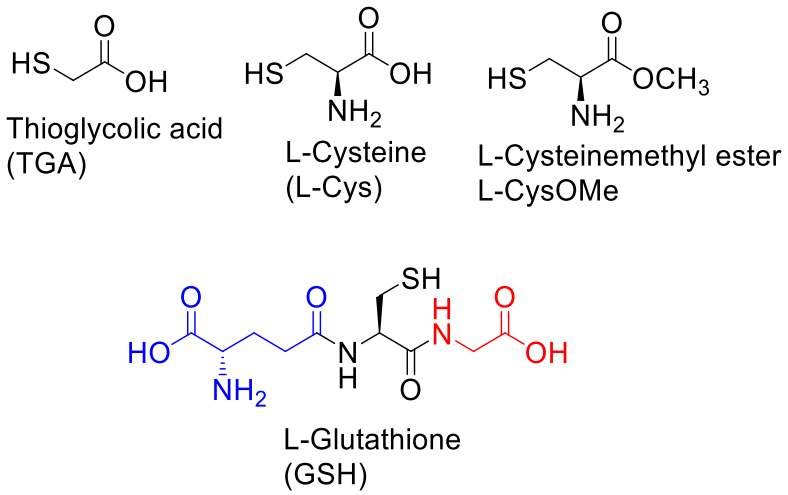


Figure 3.1. Chemical structures of the ligands used to passivate the PbS QDs surface. Mixed ligands were also used in the synthesis.

This chapter will present details of the PbS QDs synthesised, their PL emission and size characterisation.

3.2. TGL/DTG PbS QDs

A mixture of ligands of TGL/DTG was used to passivate the surface of PbS QDs and to control their size.[164] TGL/DTG PbS QDs with different molar ratios of Pb:S were synthesised in aqueous solution. The PL peak position for the PbS QDs was in the range from 1040 nm to 1090 nm for QDs with molar ratios of Pb:S of 1:0.3, 1:0.5 and

1:0.7, respectively, (Figure 3.2). The observed PL peak position increased with increasing the S molar ratio, i.e. *E* of PL decreased with increasing the S and the QDs size can be tuned by controlling the composition materials which is in agreement with previously reported data.[164]

The size of these QDs were estimated theoretically from the dependence of the PL energy on the QD size from the curve in Figure 1.4 and indicated that the formed QDs had diameter of ~ 3 nm for Pb:S molar ratio of 1:0.3, which increased to ~ 12 nm for the ratio 1:0.7.

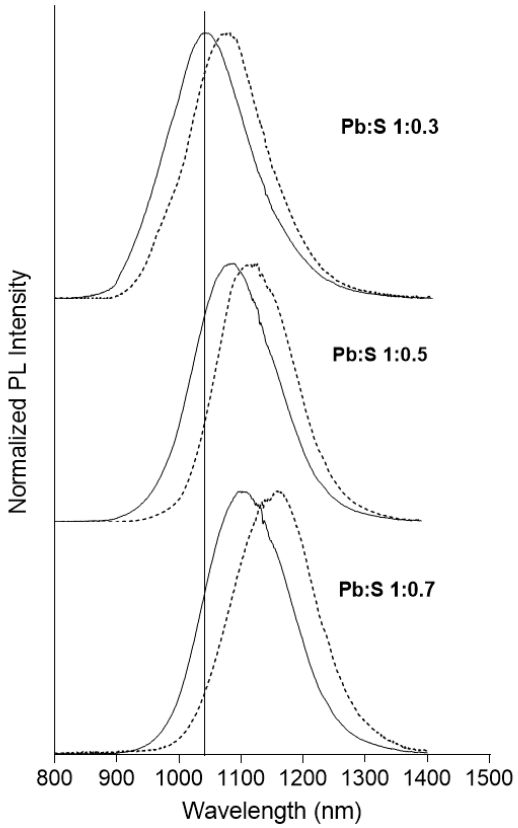
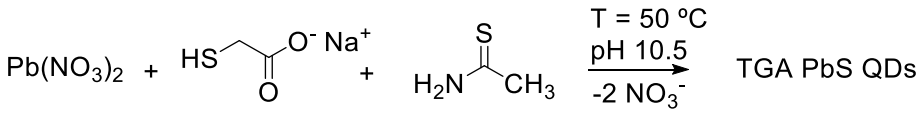


Figure 3.2. Room temperature PL spectra of PbS QDs capped with TGL/DTG with different Pb:S molar ratio on the 3rd day (solid lines) and 10th day after the synthesis (dashed lines).

The stability of the PL emission of the PbS QDs synthesised was assessed over time. The PL emission wavelength observed for the QDs after 10 days are shifted by ~ 30 nm to higher wavelength, (Figure 3.2). The main reason for PL peak shift to higher wavelength may be the result of an increase in the QD size due to Ostwald ripening. The Ostwald ripening is a process during which smaller particles are digested by larger particles, hence the average size of the nanoparticle ensemble increases. The driving force for observed changes is the difference of surface energy between nanoparticle with different sizes.[174] Other possible reasons for the PL emission shift might be due to the instability of the capping layer, this instability might lead to an increase in the number of surface defects, and resulting in PL emission shift. However, we do not see colloidal instability expected from the loss of capping layer, hence we envisage that Ostwald ripening is the key reason. These QDs remain stable in solution for at least 3 months.

3.3. TGA PbS QDs

TGA PbS QDs were prepared according to the reaction below[39], Scheme 3.1. A mixture of lead (II) and TGA was prepared and then thioacetamide, a source of S^{2-}, was added to form the brown PbS QDs. A procedure published by Martinez-Mancera *et al*.[39] to synthesis PbS QDs with PL emission in the 1st NIR window was followed. The PbS QDs were prepared with Pb:TGA:S molar ratio of 1:2:0.5 with heating to 50 ºC.



Scheme 3.1. Chemical reaction of the synthesis of TGA capped PbS QDs.

TGA PbS QDs were produced to select the composition molar ratios and the condition of the synthesis to produce QDs with emission in the 1st NIR optical widow. Similar ratio and synthesis conditions will be used to produce L-Cys PbS QDs due to the similarities between the TGA and the L-Cys. Synthesis following the reported conditions[39] did not produce QDs with emission in the first NIR. The synthesis produced a black precipitate when the solution was heated to 50 ºC. However, avoiding the heat results in the formation of colloidal QDs with PL peak position at ~ 1260 nm. Therefore, conditions were optimised, such as the molar ratios of composition and the temperature.

PbS QDs with the Pb:S molar ratios of 1:0.1, 1:0.2, 1:0.3 and 1:0.4 were used. According to the literature, decrease of the sulfur molar ratio leads to a decrease in the size of the PbS QDs.[175]

The observed PL results of the TGA PbS QDs are presented in Figure 3.3. A significant shift towards a lower wavelength is observed when the molar ratio of Pb:S was changed from 1:0.4 to 1:0.3. The observed λ_{max} emission wavelengths were 1300, 900 and 780 nm for QDs of Pb:S molar ratios of 1:0.4, 1:0.3 and 1:0.2, respectively. Although QDs with a Pb:S molar ratio of 1:0.2 had a PL peak at 780

nm, the fluorescence intensity was weak and difficult to detect. In addition, no measurable PL emission was detected for PbS QDs with a Pb:S molar ratio of 1:0.1.

Based on the PL results, the sample with a Pb:S molar ratio of 1:0.3 is considered the most promising because the fluorescence was within the detection range (λ_{max} < 900 nm).

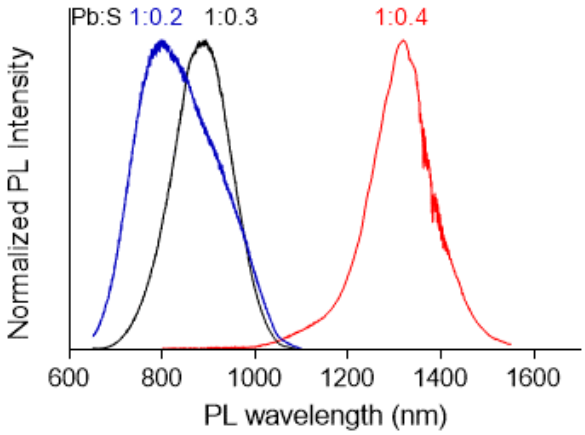


Figure 3.3. Room temperature PL spectra of PbS QDs capped with TGA with different Pb:S molar ratios (72 h after synthesis). A significant shift in emission wavelength can be seen between the 0.3 and 0.4 sulfur molar ratios.

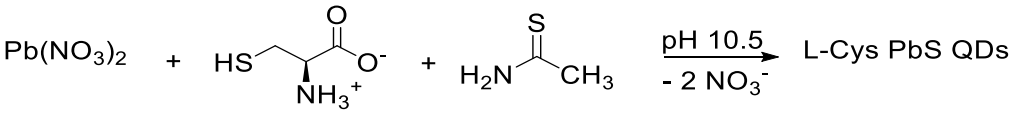
The stability of the TGA PbS QDs was assessed over a period of 15 days after the synthesis. The PL peak was observed at ~ 920 nm for QDs of Pb:S of the 1:0.3 molar ratio samples. This shift of PL properties is associated with QDs size change due to Ostwald ripening. Also, it has been found that heating of the solution during the synthesis resulted in QDs precipitating, and therefore, synthesis

were performed at room temperature. TGA PbS QDs were stable in solution for at least 3 weeks before they started to precipitate.

The TGA PbS QDs with molar ratio of Pb:TGA:S = 1:2:0.3 were selected for further work.

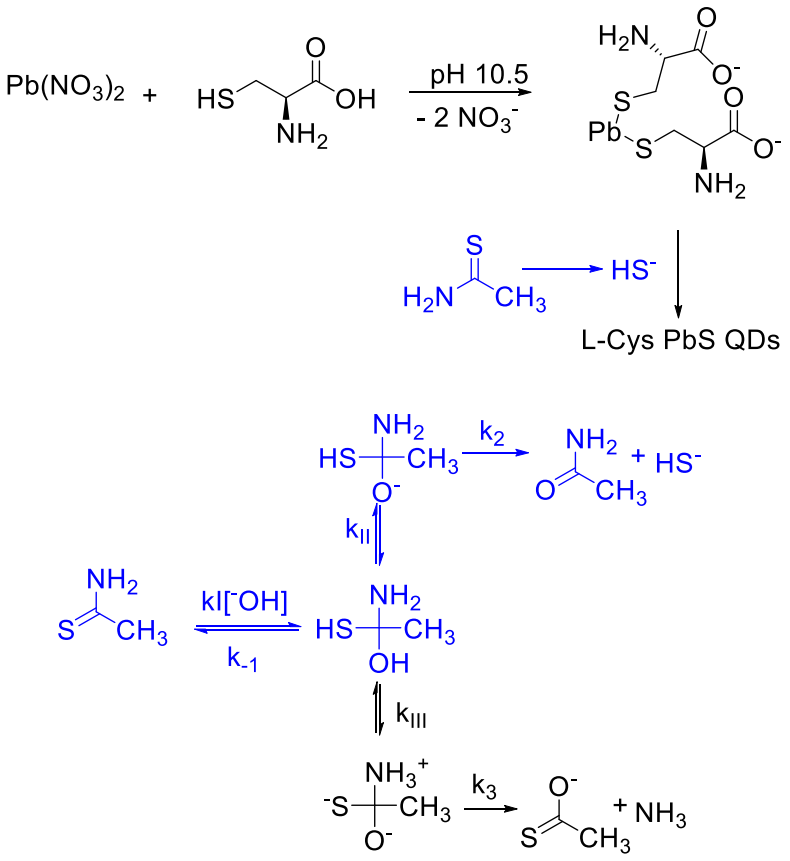
3.4. L-Cys PbS QDs

The procedure used for TGA PbS QDs synthesis was modified to synthesise L-Cys PbS QDs according to the reaction in Scheme 3.2. A precursor solution of lead (II) and L-Cys was prepared first then thioacetamide was added.



Scheme 3.2. Chemical reaction of the L-Cys PbS QDs synthesis.

The suggested mechanism of the L-Cys PbS QDs growth can be seen in Scheme 3.3. The colourless mixture of lead (II) with the ligand was prepared at pH 10.5 and then thioacetamide are slowly decomposed at basic conditions to produce S^{2-} that is needed to form the brown colloidal PbS QDs capped with the L-Cys ligand.



Scheme 3.3. Synthesis of L-Cys PbS QDs from $Pb(NO_3)_2$ and thioacetamide.

The same conditions (room temperature and pH (11.0)) and compositions (1:2:0.3) ratio of TGA PbS QDs were used to synthesise L-Cys PbS QDs. The Pb:L-Cys molar ratio of 1:2 did not produce a colloidal QDs solution even at a high pH (8.5, 9.0, 10.0, 11.0, 12.0 and 13.0). A white suspension solution of Pb^{2+} with L-Cys was formed and did not result in colourless solution by increasing the pH, and a black precipitate formed directly after the addition of thioacetamide. We envisage that the Pb^{2+} ion did not produce a soluble complex when was mixed the L-Cys at this ratio, which is in agreement with the literature[176] as a molar ratio of Pb:L-Cys > 1:2.1 is required to

produce Pb-L-Cys complex in aqueous solution. Therefore, the procedure was optimised to achieve formation of soluble QDs.

A series of higher ligand molar ratios of Pb:L-Cys were explored (2.2, 2.5, 2.8 and 3.0) to synthesise QDs. The Pb:S molar ratio was kept at 1:0.3 and 1:0.8. The observed PL emission of the synthesised QDs showed good size stability by increasing the ligand molar ratio.The λ_{max} emission wavelength observed for different L-Cys PbS QDs showed a slight decrease in the PL peak position with increasing ligand molar ratio (Figure 3.3). The increasing of the ligand molar ratio leads to an increase in the number of ligands per unit surface. This increment leads to QD crystal synthesis with smaller diameter resulting in lowering the λ_{max} of the QDs. L-Cys PbS QDs with L-Cys molar ratios of 2.2 and 2.5 produced more stable QDs in colloidal solutions, while those with ratios 2.8 and 3.0 precipitated after ~ 10 days. The ratios of Pb:L-Cys = 1:2.2 and 1:2.5 were chosen for further optimisation.

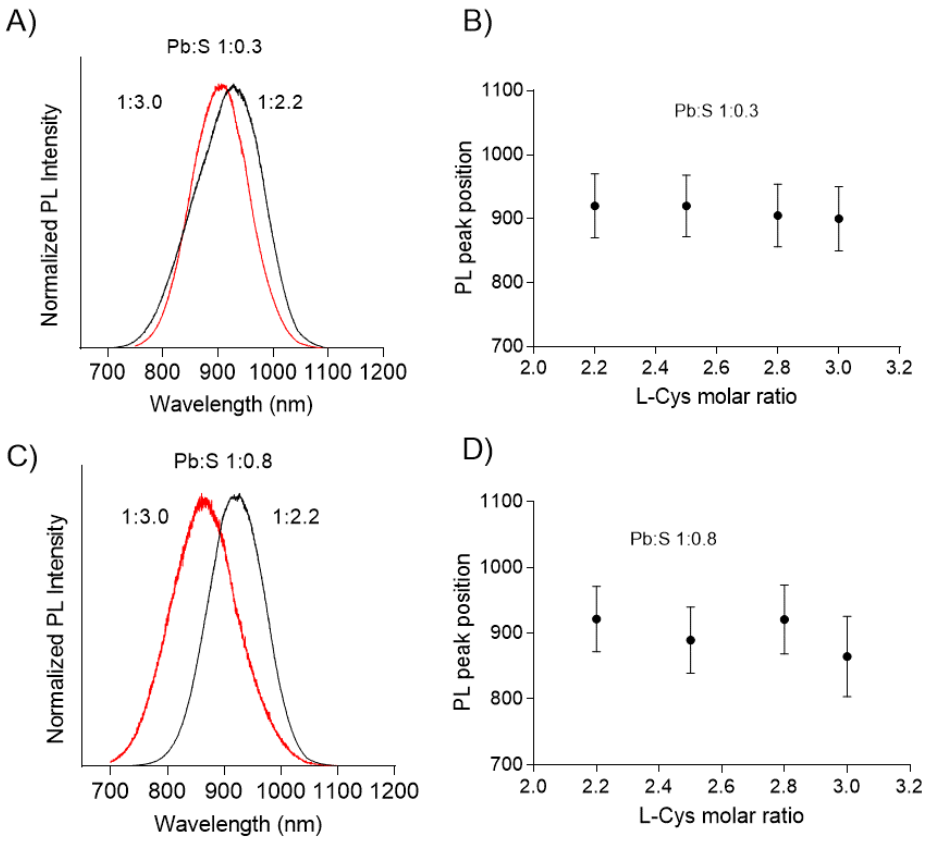


Figure 3.4. Room temperature PL spectra of L-Cys PbS QDs synthesised with Pb:S molar ratio of 1:0.3 (A) and 1:0.8 (C). (B and D) corresponding dependence of the PL peak position on Pb:ligand molar ratio. Error bars represent the standard deviation of the gaussian fit of the PL emission.

Further optimisation was attempted using different Pb:S molar ratios (1: 0.3 to 1:0.9) to control the size of the synthesised QDs through the limitation the amount of the S^{2-} which leads to stop the growth of the QDs. PbS QDs with a Pb:L-Cys molar ratio of 1:2.2 and 1:2.5 were used for optimisation. The observed PL emission of QDs with different Pb:S molar ratio is ranging between 910 - 930 nm, (Figure 3.5). It was found that increasing the S molar ratio leads to an increase in the size of the QDs (higher emission wavelength) which is in agreement with the literature.[177] Also, it was found that the QDs

with Pb:S ratio of 1:0.3 and 1:0.8 have the highest optical and chemical stability.

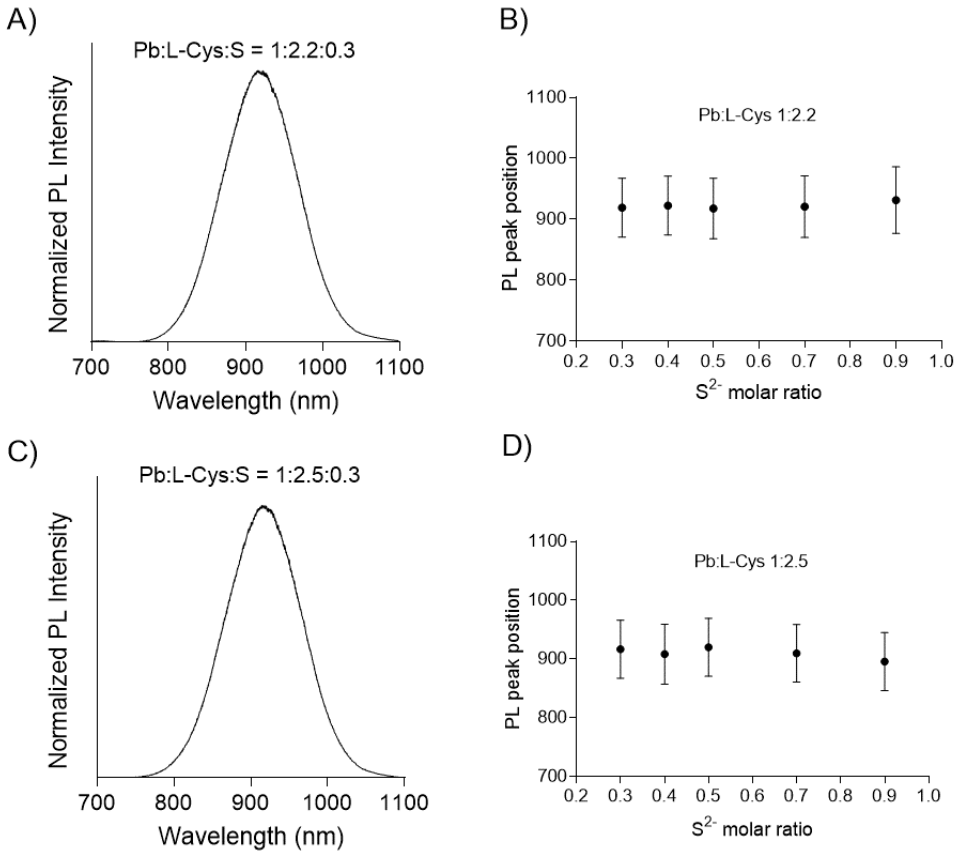


Figure 3.5. Room temperature PL spectra of L-Cys PbS QDs prepared with Pb:L-Cys:S molar ratio = 1:2.2:0.3 (A) and a dependence of maximum peak position (B) on Pb:S molar ratio. C) is the PL spectra of L-Cys PbS QDs prepared with Pb:L-Cys:S molar ratio = 1:2.5:0.3 and D) is dependence of maximum peak positions on Pb:S molar ratios. Error bars represent the standard deviation of the gaussian fit of the PL emission.

As was shown for TGL/DTG PbS QDs (Chapter 3.2) and confirmed by theory (Equation 1), we expect to form larger QDs by increasing the S molar ratio. However, the PL emission wavelengths did not reveal significant change in the PL peak position with increasing the S molar ratio indicating that the size of optically active nanocrystals is

comparable in both samples. On the other hand, the DLS measurements show larger hydrodynamic size changing from 14 ± 5 to 18 ± 5 for QDs of Pb:S molar ratio of 1:0.3 and 1:0.8 respectively, Figure 3.6. We envisage that additional S is not incorporated into the crystalline core of the QDs but is forming an amorphous nanocrystal shape. We propose that the interaction of capping ligands with QDs could be responsible for the decreasing in size and merits further investigation.

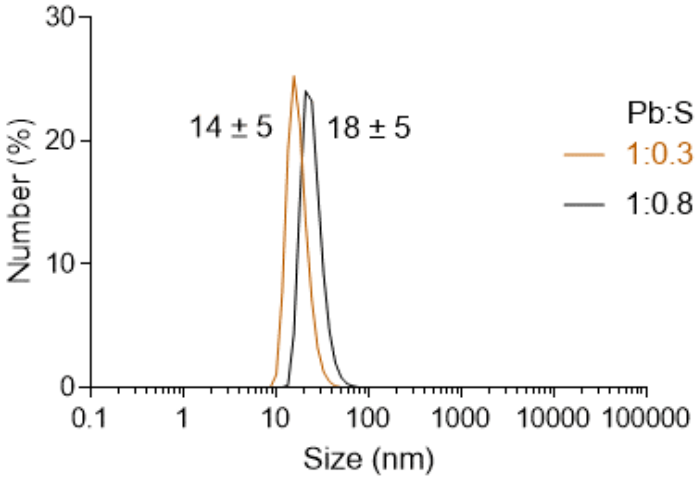


Figure 3.6. The size distribution profile of the PbS QDs of Pb:L-Cys molar ratio of 1:2.5 with 1:0.3 and 1:0.8 molar ratio of Pb:S.

The stability of the PL peak position and the QDs size of L-Cys PbS QDs was examined over time by monitoring the PL properties. PbS QDs of Pb:L-Cys:S molar ratio of 1:2.5:0.3 were stable for at least 17 days, while QDs of Pb:L-Cys:S molar ratio of 1:2.5:0.8 were observed PL stability for at least 31 days (Figure 3.7), then the PL intensity decreased. The observed shift to a higher wavelength is due

to the Ostwald ripening which results in an increase of the QDs diameter.

However, the QDs were remaining stable in aqueous solution for ~ 50 days before the appearance of black precipitate in the colloidal solution. The precipitation of the colloidal QDs is likely due to the loss of the ligand shell which affects the stability in the aqueous solution and leads to QDs aggregation.

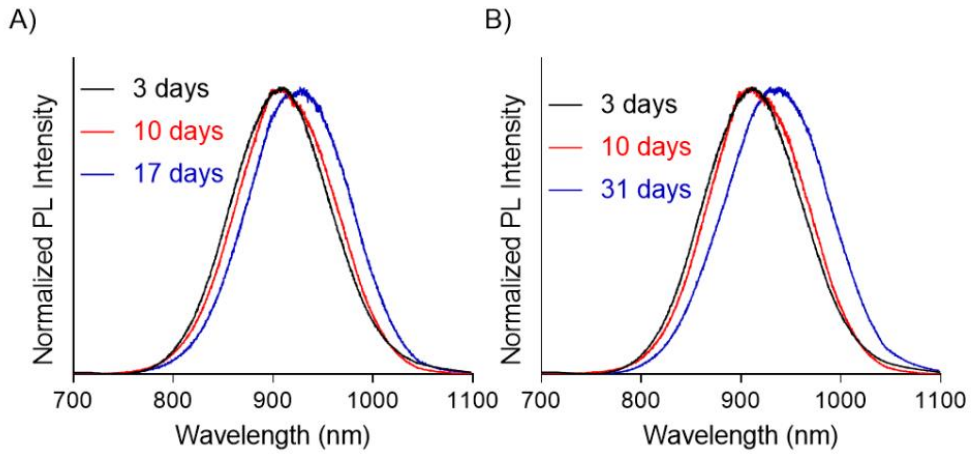


Figure 3.7. Room temperature PL spectra of L-Cys PbS QDs with Pb:L-Cys:S molar ratio of 1:2.5:0.3 (A) and 1:2.5:0.8 (B) measured over a period up to 31 days.

The effect of pH on the stability of the QDs solutions was checked at pH values from 9.5 to 11.0. L-Cys PbS QDs stored at pH > 10.0 had precipitated in ~ 3 days. The precipitation could be results of reduction of the surface charge which can lead to reduce the electrostatic repulsive between the particles and limited their stability in solution. The QDs of Pb:L-Cys:S molar ratio of 1:2.5:0.3 and 1:2.5:0.8 showed higher stability at pH 10.5.

The size of the L-Cys PbS QDs were affected by the pH used in the synthesis. QDs produced at pH 11.0 had PL peak position higher than PL of QDs synthesised at pH 10.5 (Figure 3.8). The quick formation of the QDs at higher pH due to the formation of a higher amount of the Pb-Ligand was the more likely reason for the higher PL achieved.

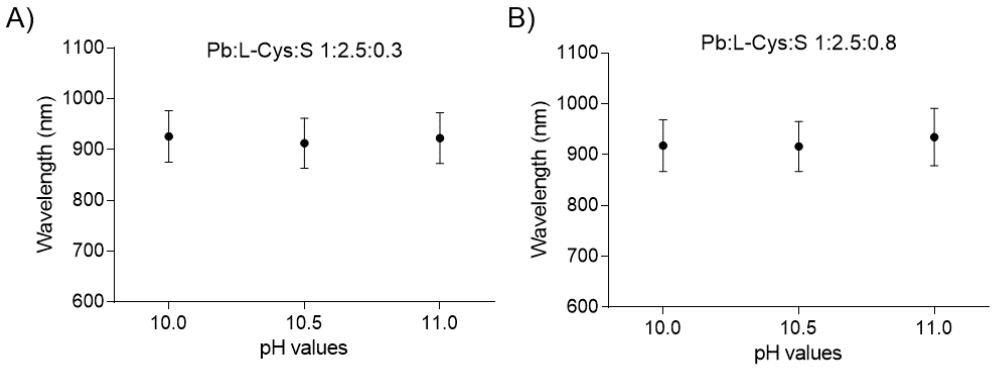


Figure 3.8. Room temperature PL peak position of L-Cys PbS QDs with Pb:L-Cys 1:2.5 synthesised at different pH for QDs with Pb:S ratio of 1:0.3 (A) and 1:0.8 (B). Error bars represent the standar deviation of the gaussian fit of the PL emission

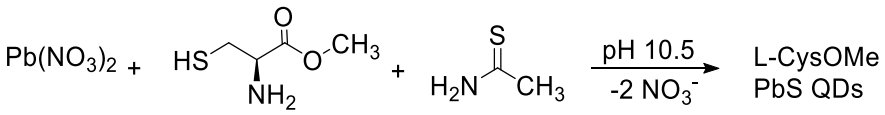
The reproducibility in the synthesis of the PbS QDs was checked. Synthesis was performed at least 3 times, therefore we can say the L-Cys PbS QDs are reproducible with Pb:L-Cys molar ratio of 1:2.2 and 1:2.5 with both Pb:S molar ratios of 1:0.3 and 1:0.8.

The value of the surface charge of the QDs is important for the encapsulation inside the AFt cage, which has a negatively charged interior. The surface charge of the L-Cys PbS QDs was also measured using a surface zeta potential DLS zetasizer. L-Cys PbS QDs had a strongly negative surface charge (− 50 mV). The free carboxylic

group on the surface of the QDs has a negative charge under basic pH conditions. Modifying the ligand on the surface could be used to reduce the negative charge of the QDs. L-CysOMe, an ester derivative of L-Cys was chosen to cap the QDs. From the observed results we thus conclude that L-Cys PbS QDs are water soluble, stable and reproducible in colloidal solutions and their optical properties are promising for further studies.

3.5. L-CysOMe PbS QDs

L-CysOMe PbS QDs are produced according to the reaction below; a mixture of lead (II) nitrate and L-CysOMe is prepared, then thioacetamide is added:



Scheme 3.4. Chemical reaction of L-CysOMe PbS QDs synthesis.

The suggested mechanism for the synthesis is similar to the mechanism of the synthesis of the L-Cys PbS QDs shown in the Scheme 3.3. Thioacetamide provides a source of S^{2-}; the solution turns brown upon the addition of thioacetamide indicating the formation of the L-CysOMe PbS QDs.

In order to reduce the negative charge on the surface of the PbS QDs, the L-CysOMe was used as a capping ligand. Pb:L-CysOMe molar ratios from 1:2 to 1:6 were used for the synthesis. The ratio of Pb:L-

CysOMe of 1:2, 1:2.5 and 1:3 did not produce PbS QDs and instead, a white precipitate was formed, which is likely lead oxide PbO_2. By increasing the molar ratios of the Pb:L-CysOMe to 1:4, 1:5 and 1:6, a clear colloidal brown solution of PbS QDs was formed. The photoluminescence studies for these QDs (Figure 3.9) reveal a shift of PL peak from 1240 nm to 930 nm for PbS QDs with Pb:L-CysOMe of 1:4 and 1:5, respectively.

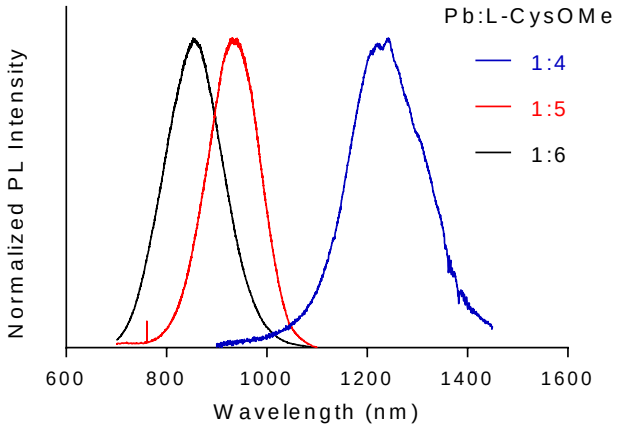


Figure 3.9. Room temperature PL spectra of L-CysOMe PbS QDs with different Pb:L-CysOMe molar ratios. The ratio of Pb:S = 1:0.3.

The size distribution of the L-CysOMe PbS QDs was measured by DLS. The hydrodynamic size distribution observed for QDs with Pb:L-CysOMe molar ratio of 1:5 was 14 ± 6 nm, while for QDs with a 1:6 molar ratio it was 12 ± 4 nm (Figure 3.10). We found that the QDs with a higher ligand molar ratio had a smaller diameter.

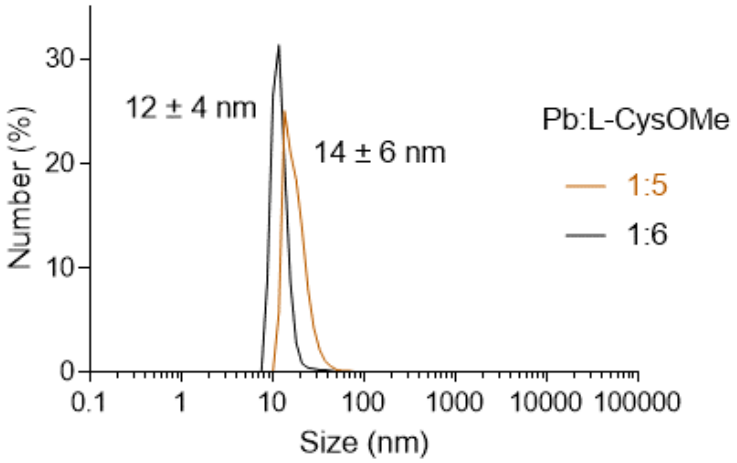


Figure 3.10. Hydrodynamic size distribution of L-CysOMe PbS QDs measured by DLS for different L-CysOMe molar ratios. The ratio of Pb:S = 1:0.3.

The charge of the QDs was monitored by measuring their zeta potential using the DLS. The charge increased from − 50 mV for PbS QDs with L-Cys to − 30 mV for PbS QDs capped with L-CysOMe. PbS QDs capped with L-Cys OMe at 1:6 ligand molar ratio had the same hydrodynamic size as L-Cys PbS QDs and also nearly the same λ_{max} as L-Cys PbS QDs (~ 860 nm). However, the lower negative charge achieved for the L-CysOMe PbS QDs could make these QDs promising for their encapsulation by AFt, where no strong electrostatic repulsion would be expected between the nanocrystal and the charge on AFt interior.

L-CysOMe PbS QDs with a Pb:L-CysOMe 1:6 molar ratio had low optical stability. The PL peak position of these QDs was slightly red-shifted and intensity was very weak after 10 days. Some precipitation was observed. However, QDs with a Pb:L-CysOMe 1:5 molar ratio

were stable for at least 17 days with respect to their optical properties, as shown in Figure 3.11.

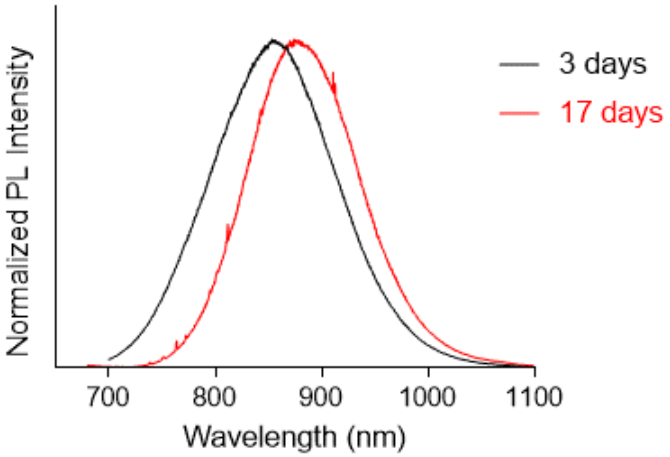
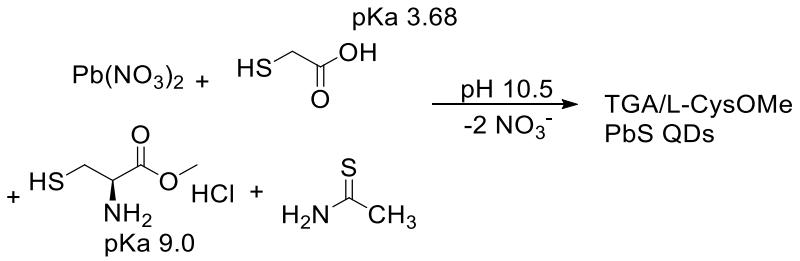


Figure 3.11. Room temperature PL spectra of L-CysOMe PbS QDs of Pb:L:S 1:5:0.3 measured in the 3rd day of the synthesis and the 17th days.

The colloidal and optical stability, and the reduction of the negative charge on the QDs surface make these QDs promising candidates for encapsulation.

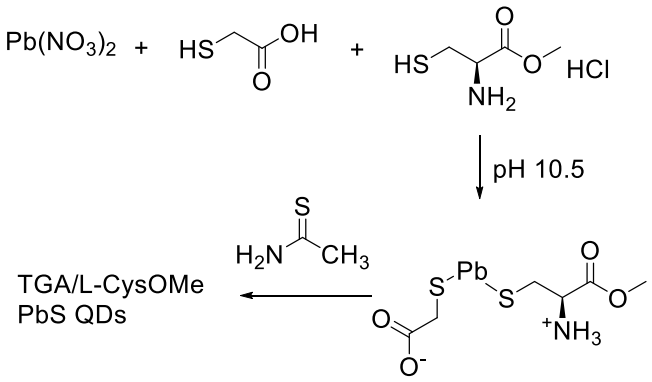
3.6. TGA/L-CysOMe PbS QDs

A mixture of TGA/L-CysOMe ligands were used to passivate the QDs surface. It is expected that presence of the L-CysOMe will reduce the negative surface charge of the QDs and will facilitate efficient QD encapsulation into the AFt. PbS QDs are produced according to the equation below. A complex of lead and TGA/L-CysOMe is produced first then thioacetamide is added:



Scheme 3.5. Chemical reaction of TGA/L-CysOMe PbS QDs.

The suggested mechanism of the synthesis starts with the formation of a colourless mixture formed upon adding TGA and L-CysOMe to the Pb^{2+} ion which indicated the coordination of the ligands with the lead ion. Then thioacetamide is added producing a brown solution of PbS QDs that started to form slowly after mixing for 4 h under nitrogen. The PbS QDs were synthesised in water at room temperature (Scheme 3.6).



Scheme 3.6. Synthesis of PbS QDs capped with TGA/L-CysOMe PbS QDs.

In order to produce stable PbS QDs, mixing of TGA and L-CysOMe ligands was investigated. The maximum peak emission wavelength observed for TGA PbS QDs was ~ 860 nm; however, the low stability

of the synthesised TGA PbS QDs lead us to think about modifying the surface of the QDs using a mixture of TGA and L-CysOMe with total ligand molar ratio of 2.5. A range of TGA/L-CysOMe molar ratios has been used (2:0.5, 1.5:1, 1:1.5 and 1:1). However, only two ratios (1.5:1 and 1:1) formed QDs as colloidal solutions while the others formed precipitates.

The optical stability of these QDs was examined for a period of time by monitoring the PL emission. The observed λ_{max} emission of PbS QDs with ligands ratio of TGA:L-CysOMe = 1.5:1 was monitored and the PL wavelength was stable for at least 2 months and detectable at 860 nm, Figure 3.12. These QDs have been reproduced at least 3 times with the same PL wavelength region area.

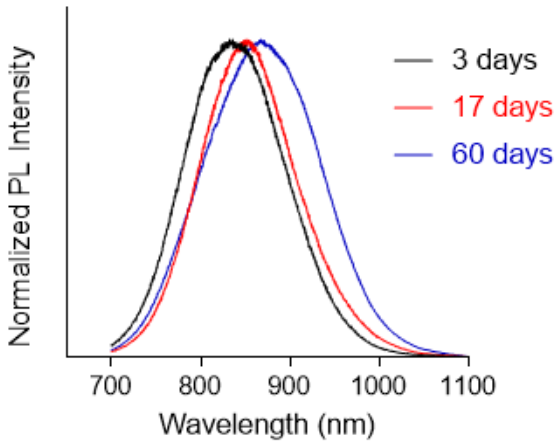


Figure 3.12. Room temperature PL spectra of PbS QDs of Pb:TGA:L-CysOMe:S 1:1.5:1:0.3 measured in period between the 3rd day of the synthesis and 60th days.

The hydrodynamic size was determined using DLS. The observed hydrodynamic diameter for TGA/L-CysOMe PbS QDs was 6 ± 2 nm,

shown in Figure 3.13. Although TGA/L-CysOMe PbS QDs have nearly the same PL emission like L-Cys PbS QDs of the same ligand ratio (Pb:L-Cys:S = 1:2.5:0.3) (~ 900 nm), the distribution size profile measured by the DLS was determined to be a smaller size for the TGA/L-CysOMe PbS QDs. The difference in the size distributions is likely due to the differences in the size of ligands capping the QDs. Also, the amount of water molecules can surround the QD core and the surface ligands. In addition, different pH and concentration can effect the size distribution. Therefore, different QDs with the same PL emission can have different hydrodynamic sizes measured by the DLS.

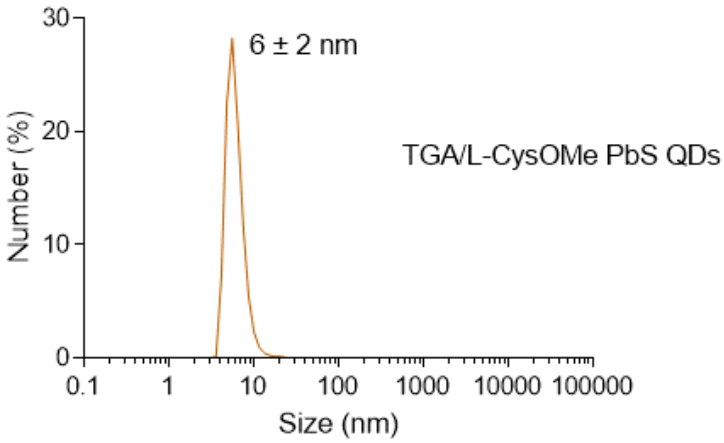


Figure 3.13. Size distribution of the TGA/L-CysOMe PbS QDs of Pb:TGA/L-CysOMe:S molar ratio of 1:1.5:1:0.3 measured by DLS.

TGA/L-CysOMe PbS QDs with a molar ratio of Pb:TGA:L-CysOMe of 1:1:1 was synthesised. This ratio was chosen to compare it to the total Pb:TGA molar ratio of 1:2.0 used in the literature.[39] The maximum peak emission observed for these QDs was 870 ± 50 nm.

These QDs showed stability for at least 24 days. They were reproduced twice and have a λ_{max} emission that is promising for further studies.

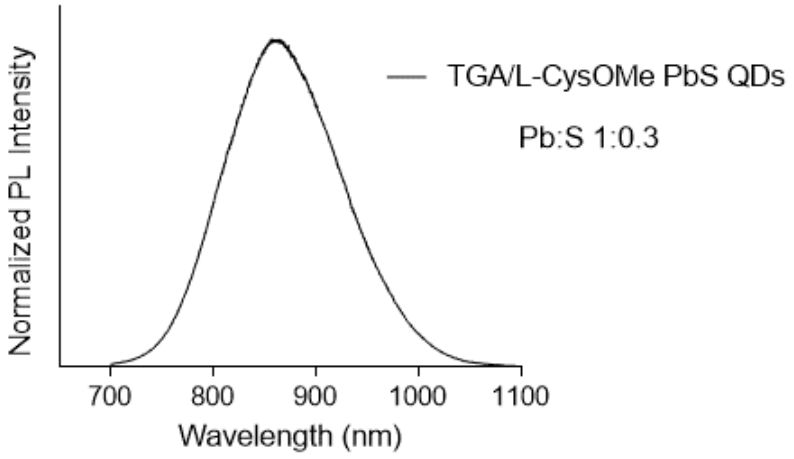


Figure 3.14. Room temperature PL spectra of TGA/L-CysOMe PbS QDs of 1:1:1:0.3.

The size distribution of these QDs observed using DLS was 9 ± 3 nm (Figure 3.15). The size of the TGA/L-CysOMe PbS QDs of Pb:TGA:L-CysOMe molar ratio of 1:1:1 is larger than PbS QDs of Pb:TGA:L-CysOMe molar ratio of 1:1.5:1. This result is more likely due to the difference in TGA molar ratio and the length of the capping ligands.

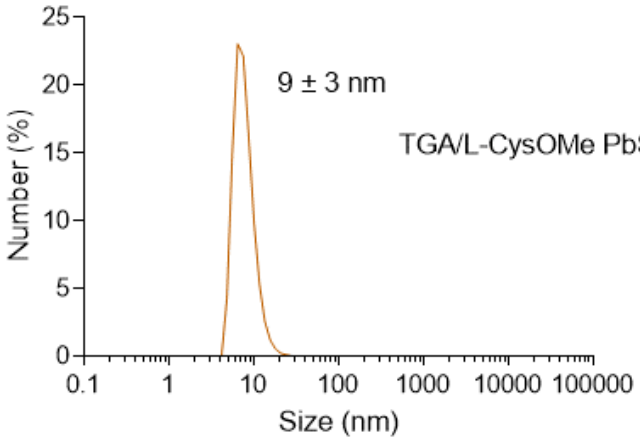


Figure 3.15. Size distribution profile of TGA/L-CysOMe PbS QDs was measured by DLS. The ratio of Pb:TGA:L-CysOMe:S = 1:1:1:0.3.

Finally, the results suggested that TGA/L-CysOMe PbS QDs are soluble, stable, reproducible and optically active. Furthermore, these QDs showed longer-term stability than those capped with individual ligands, TGA or L-Cys or L-CysOMe, which made them promising candidates for encapsulation and further studies.

3.7. GSH PbS QDs

The last ligand which was used to stabilize the PbS QDs surface was glutathione (GSH), which is a tripeptide consisting of three amino acids: L-glutamate (L-Glu), L-cysteine (L-Cys) and glycine (Gly), shown in Figure 3.16. GSH is present in living cells at up to 1 mM and it represents a high source of non-proteinogenic amino acids. GSH has various functions in most biological organs such as protecting cells against oxidative stress, reacting with toxic compounds as a coenzyme and as a transporter of amino acids in the metabolism of

therapeutic drugs and carcinogens.[178,179] In addition, the chemical structure of GSH contains two carboxyl groups and one primary amino group, which can provide the opportunity for nanoparticles coated with GSH to be conjugated to a biological compound such as an antibody.[180]

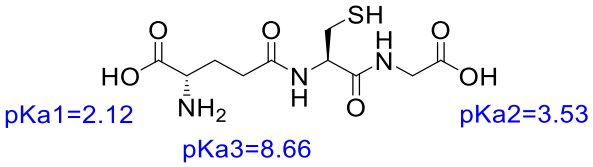
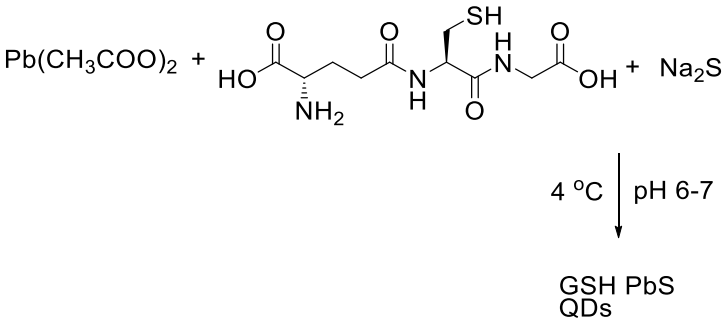


Figure 3.16. Chemical structure of GSH.

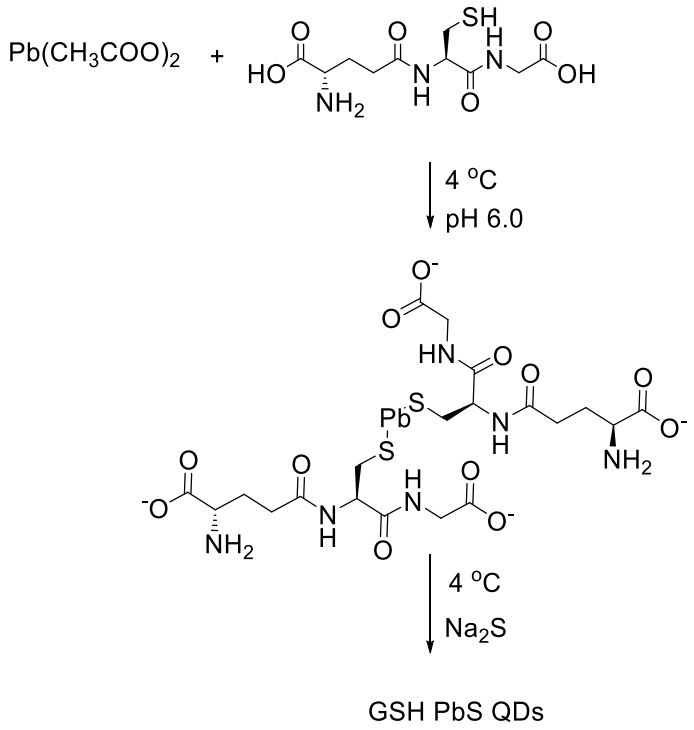
GSH PbS QDs were synthesised in water following the reaction below.[165] Sodium sulfide was added after the formation of the colourless mixture of the lead (II) acetate with the glutathione at *T* = 4 ºC.



Scheme 3.7. Chemical reaction of GSH PbS QDs synthesis.

The GSH PbS QDs were prepared with Pb:GSH:S molar ratios of 1:2:0.5 by following the procedure published by Nakane *et al*.[165] The suggested mechanism for the synthesis is mixing the GSH with the

lead ion (Pb^{2+}) through the thiol group and forming a colourless solution at pH 6.0. Then S^{2-} from the sodium sulfide is added to directly form the PbS QDs brown solution. The scheme below represents this procedure (Scheme 3.8).



Scheme 3.8. Synthesis of PbS QDs capped with GSH ligand

The observed λ_{max} emission wavelength for the GSH PbS QDs is monitored at 890 nm (Figure 3.17) giving QDs with an estimated diameter ~ 3.5 nm. The optical stability was examined over a period of 31 days and high stability was observed for the GSH QDs. In addition, these QDs were stable in solution for at least 60 days.

GSH PbS QDs were prepared at a low temperature (4 ºC) to reduce the formation rate of the QDs and control the size of the synthesised QDs.

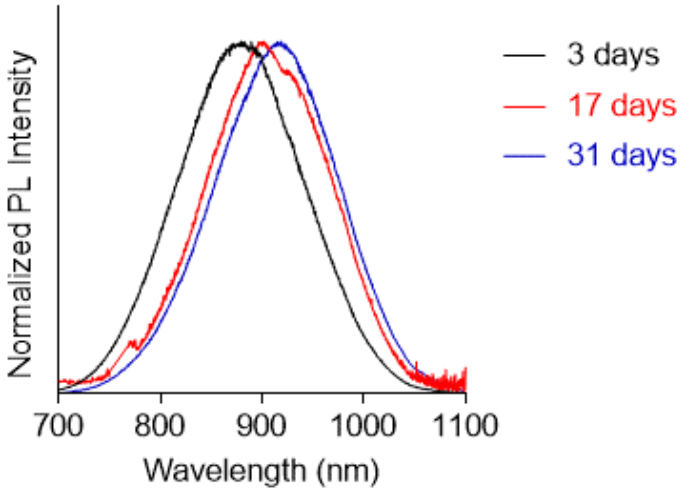


Figure 3.17. Room temperature PL spectra of GSH PbS QDs with Pb:GSH:S molar ratio 1:2:0.3 prepared at pH 6.5, and measured at different periods of time.

The conditions of synthesis for the GSH PbS QDs were optimised to prepare stable PbS QDs with a PL wavelength below 900 nm by using different sulfur molar ratios (0.3, 0.5, 0.8 and 1.0). The obtained results showed that maximum emission peaks starts to shift to the second NIR window after increasing the S molar ratio from 0.5 to 0.8 (Figure 3.18) which is in agreement with the literature that increasing the sulfur molar ratios lead to produce larger QDs (QDs with higher PL wavelength).[177] Furthermore, the PbS QDs with Pb:S molar ratios of 1:0.3, 1:0.8 and 1:1 showed less stability in solution than QDs of Pb:S molar ratio of 1:0.5, and the PbS QDs were precipitated after fewer than 17 days. Therefore, PbS QDs with Pb:S molar ratio of 1:0.5 were selected to synthesise the GSH PbS QDs for additional studies.

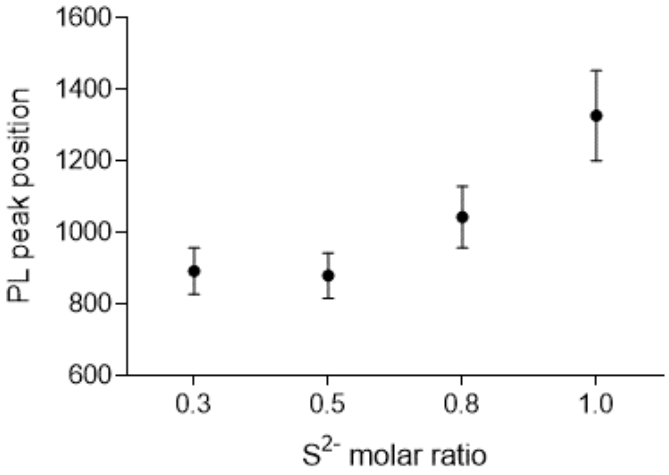


Figure 3.18. Room temperature PL peak position of PbS QDs synthesised with different Pb:S molar ratios with Pb:GSH of 1:2 molar ratios at pH 6.0.

Different pH values (6.0 and 8.0) were used for the GSH PbS QDs synthesise. The results obtained (Figure 3.19) showed a clear shift towards the 1st NIR window when a low pH (6.0) was used to synthesis the QDs. The use of a pH higher than 8.0 resulted in formation of higher concentration of sulfhydryl group which lead to a high speed of QDs formation.[181]

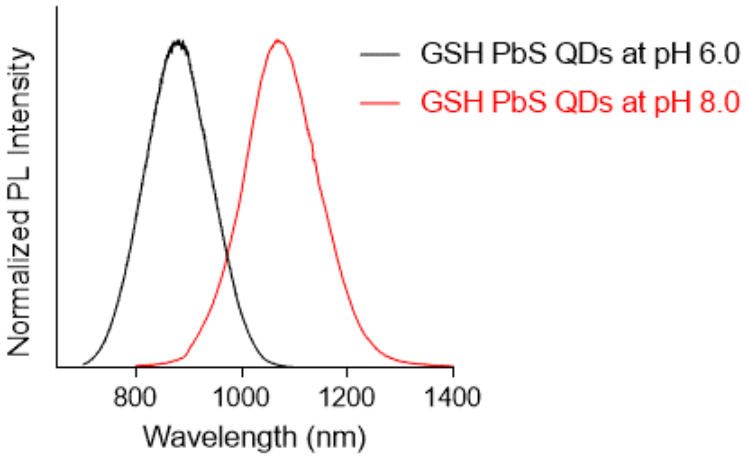


Figure 3.19. Room temperature PL spectra of GSH PbS QDs of Pb:GSH:S 1:2:0.5 at pH 6.0 and 8.0.

The hydrodynamic size distribution of the GSH PbS QDs was measured by DLS. The observed hydrodynamic diameter of the QDs was 7 ± 2 nm. The difference between the expected size estimated from the PL is 3.5 nm and the observed hydrodynamic size is 7 ± 2 nm. The difference is more likely due to monitoring of the QD core, ligand and water molecules surrounding QD by using the DLS.

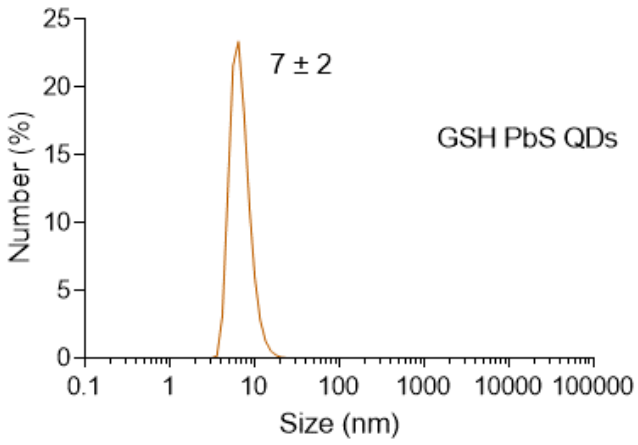


Figure 3.20. Size distribution profile of GSH PbS QDs measured by DLS.

These results indicate the best conditions to synthesise PbS QDs capped with GSH that emit at less than 900 nm with the highest stability. The synthesis was applied by controlling the composition of the Pb:GSH:S molar ratios of 1:2:0.3, and controlling the pH values of the synthesis (6.0) in addition to the temperature of the reaction (4 ºC). These conditions were selected to synthesis PbS QDs for additional studies.

3.8. Comparison between the different synthesised PbS QDs

PbS QDs capped with different thiol capping ligands were synthesised with PL emission wavelengths between 860 and 920 nm that are in the 1st NIR window (Figure 3.21). These PbS QDs have colloidal and optical stability and they are reproducible. The best conditions and the PL emission of the synthesis are presented in the Table 3.1.

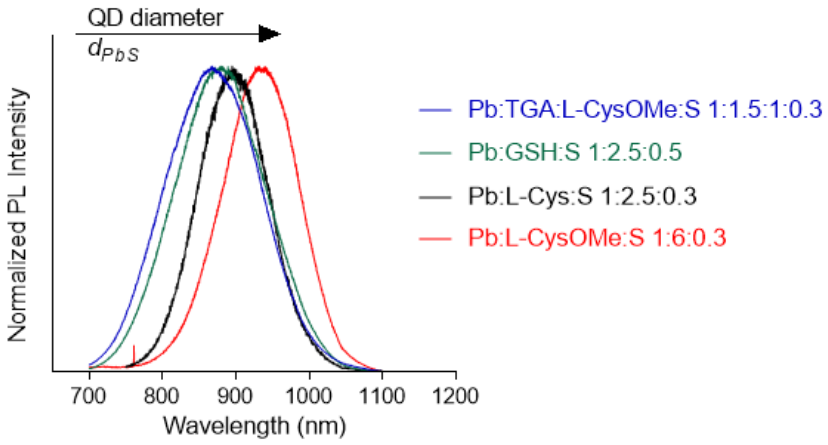


Figure 3.21. Room temperature PL spectra of PbS QDs capped with different thiol ligands and synthesised with Pb:S molar ratio = 1:0.3.

Table 3.1. The synthesised PbS QDs with different capping ligands, with optimised conditions and PL peak position.

Ligands	Pb:L	Pb:S	pH	*T* (ºC)	Stability (week)	λ_{max} (nm)	Zeta potential (mV)
TGA	1:2	1:0.3	1.5	25	2	900	x
L-Cys	1:2.5	1:0.8	10.5	25	4	900	- 50
L-CysOMe	1:6	1:0.3	10.0	25	2	860	- 30
TGA/L-CysOMe	1:1.5:1	1:0.3	11.0	25	8	870	x
GSH	1:2	1:0.3	6-7	4	8	890	x

The PbS QDs synthesised were prepared and stored under N_2 atmosphere at 4 ºC for further studies.

Although the PbS QDs were synthesised with maximum peak emission wavelengths ~ 900 nm, the DLS measurements to determine the hydrodynamic size of the QDs was slightly different. The results observed for the size of the L-Cys PbS QDs and L-CysOMe PbS QDs were 14 – 18 nm and 12 - 14 nm, respectively, while for TGA/L-CysOMe PbS QDs and GSH PbS QDs were 6 - 7 nm, respectively. These differences are probably due to the synthesis of the QDs at different concentrations, which has an effect on the distribution of the QDs in their solution. In addition, the DLS measures the hydrodynamic size distribution of the QDs, which

represents the QDs core with ligands and the attached water molecules to the free functional groups on the surface, which can be affected by the pH of the solution.

3.9. Conclusions

PbS QDs with promising size and optical properties were synthesised with different capping ligands containing thiol groups. QDs surfaces were efficiently passivated by controlling the ligand molar ratio to Pb^{2+} ion to observe stable QDs. It was found that smaller PbS QDs diameter can be achieved by increasing the ligand molar ratio to Pb and reducing the S molar ratio to Pb.

PbS QDs capped with TGL/DTG, TGA, L-CysOMe, TGA/L-CysOMe and GSH capping ligands are synthesised with PL emission in the first NIR window except the QDs with TGL/DTG which are emitting in the second NIR. QDs with TGA/L-CysOMe and GSH capping ligands are more stable in aqueous solutions than QDs with other ligands probably due to the availability of the free functional groups and the repulsion between the QDs in the solution due to their negative charge. The produced QDs are promising for encapsulation inside the AFt- cage due to their small sizes and high stability.

Chapter 4

4. Apoferritin purification and characterisation

4.1. Introduction

Ferritin plays a significant role in iron storage and transportation to control cellular iron homeostasis in animals, plants, bacteria and humans.[182] Recently, ferritin has been used as a nanocarrier in molecular imaging and drug delivery.[106] Application of AFt for cargo delivery has several significant advantages such as homogenous size, controlled pH dependent release, solubility and selectivity in physiological solvents.[183]

A version of cysteine free AFt was designed by Dr Lei Zhang (University of Nottingham)[167] by mutating the 3 cysteine residue in the C90, C102 and C103 with Arginine (R90), Alanine (A102) and Serine (S130), respectively to prevent aggregation that may occurs due to the formation of the disulphide bond. The human heavy chain apoferritin cysteine free (AFt-) has been used in this study.

An affibody (Afb) is a small protein with molecular mass of ~ 6.5 kDa that has an affinity to target specific cellular receptors and was recently used for targeted delivery imaging agents and cancer therapies.[143,184]

A fusion of heavy chain apoferritin cysteine free AFt- and affibody protein was designed by Dr Lei Zhang (University of Nottingham)[167] to have one Afb per AFt- subunit, i.e. each AFt- cage contains 24 Afb

on the surface to use in biological applications. An apoferritin cage was prepared with an average of 4 Afb copies by mixing AFt- and Afb-AFt- in a specific ratio. Afb-AFt- was used for the encapsulation of the PbS QDs. The usage of Afb-AFt- with average of 4 Afb copies instead 24 copies is to specify the selectivity of the carrier protein toward HER2 receptors and improve the avidity of the AF-Afb to bind with the HER2 receptors

In this study, cysteine free human heavy chain apoferritin (AFt-) and a fusion of affibody-apoferritin were selected. This chapter will present the expression and the purification studies of AFt- and Afb-AFt- with an average of 4 copies of Afb per cage.

4.2. Estimation of Aft- and Afb-AFt- native molecular weight

In order to determine the molecular weight of the native protein cages, AFt- was compared with horse spleen (HoS) apoferritin (Sigma) with known molecular weight (440 kDa). The observed image (Figure 4.1) was showing a band of the purified AFt- leveled between the HoS monomer and dimer AFt cage. These results indicated the molecular weight of the purified AFt- is ranged between 440 kDa and 880 kDa.

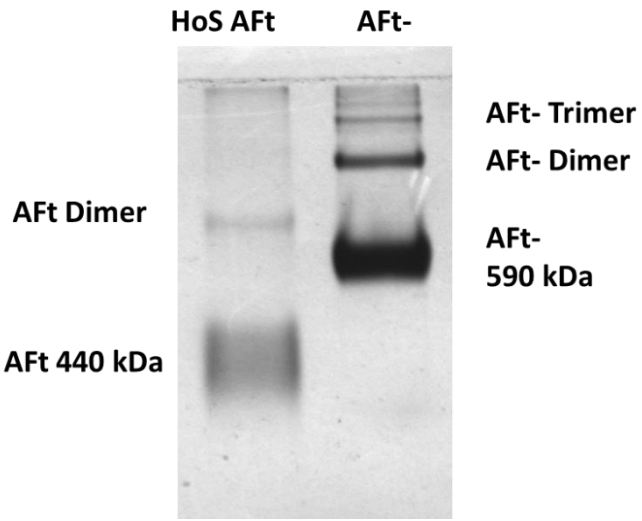


Figure 4.1. Native PAGE gel (10 cm x 10 cm x 1.0 mm, 6% (w/v), 120 V, 3 h) of horse spleen (HoS) AFt versus purified AFt-.

Furthermore, the molecular weight of the AFt- polypeptide subunit was determined by the MALDI-TOF mass spectrometry as 24.521 kDa, Figure 4.2. The AFt- cage consists of 24 polypeptide subunits and therefore we can calculate the molecular weight of the native AFt- to be ~ 590 kDa.

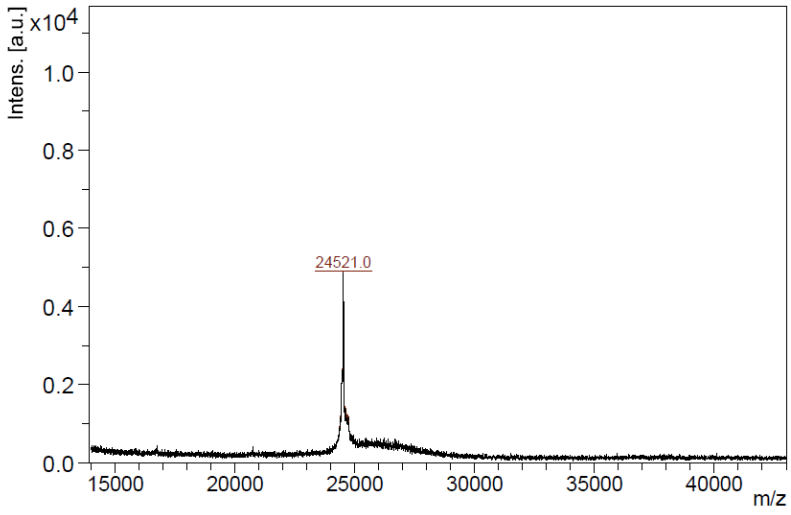


Figure 4.2. MALDI-TOF spectrum indicated the molecular weight of AFt-.

For the Afb-AFt- with an average of 4 Afb copies, a mixture of AFt- and Afb-AFt- was used with AFt-:Afb-Aft- ratio 20:4, i.e. each Afb-AFt- cage consist of 20 polypeptide subunit of AFt- (20 x 24.521 kDa) and 4 polypeptide subunit of Afb-AFt- (4 x 30.2 kDa). Therefore, we can estimate the molecular weight of the Afb-AFt- of 4 Afb copies to be ~ 611 kDa.

4.3. Expression and purification of human heavy chain apoferritin

E. coli (DE3) was used to express the AFt- with the amino acid sequence shown in Figure 4.3. The bacteria were grown in 1 L LB media at 37 ºC until an optical density of ~ 0.6 was achieved. IPTG was added to a final concentration of 1 mM to induce the bacteria to express the AFt-, (see also Chapter 2.3.1).

A histidine tag (His-tag) is required within the sequence of the designed protein for more efficient purification due to its high affinity towards the metal ions (Co^{2+}, Ni^{2+}, Cu^{2+}, Zn^{2+}), which are used in the immobilised metal ion affinity chromatography (IMAC) purification technique. His-tags are 6 histidine residues linked to the N-terminus or C-terminus of the protein.[184] In AFt-, the His-tag is located at the N-terminus.

Avi tag, which is an affinity tag, can be used for protein purification. The lysine residue in the Avi tag can be selectively biotinylated using biotin ligand. These provide a potential purification strategy using the highly specific biotin and streptavidin interaction.

1 MHHHHHHGLNDIFEAQKIEWHELVPRGSMTTASTSQVRQNYHQDSEAAI
50 NRQINLELYASYVYLSMSYYFDRDDVALKNFAKYFLHQSHEEREHAEKL
100 MKLQNQRGGRIFLQDIKKPDSDDWESGLNAMECALHLEKNVNQSLLELH
150 KLATDKNDPHLCDFIETHYLNEQVKAIKELGDHVTNLRKMGAPESGLAE
200 YLFDKHTLGDSDNES

Figure 4.3. Primary amino acid sequence used for expression of the AFt- subunit. Red: His tag, blue: Avi tag.

The AFt- can be purified from both soluble and insoluble fractions. The protein was purified from the soluble fraction. Two main reasons guided this selection: i) the concentration of the purified protein from the soluble fraction was > 7 mg/mL for each 2 L of grown bacteria while from the insoluble fraction only ~ 0.8 mg/mL was obtained; ii) both fractions had equivalently high purity when run on SDS PAGE. Therefore, the soluble fraction was selected.

The purified protein sections were collected and run on SDS PAGE to prove the molecular weight of the AFt- and its purity. The SDS PAGE in Figure 4.4 presents a typical band of the purified AFt- subunits with molecular weight ~ 24 kDa, which is comparable to the molecular weight of heavy chain AFt- subunits reported in the literature.[126]

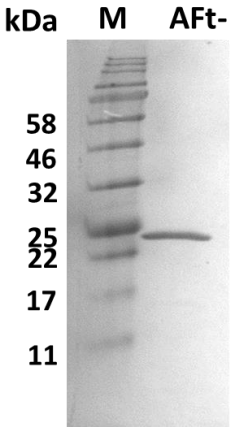


Figure 4.4. SDS PAGE of AFt- purified from the soluble fraction using the IMAC technique. M is molecular marker (Thermofisher).

Native PAGE was ran to examine the molecular weight of the purified native protein. The band corresponding to ~ 590 kDa molecular weight was observed for the purified AFt-. The purified AFt- cage was compared to AFt cage purified and characterised by Dr Lei Zhang (University of Nottingham)[167] with molecular weight of 590 kDa which indicates the correct formation of the 24-mer cage (Figure 4.5). The other bands with higher molecular weight are likely dimers and trimers of AFt- cages.[48]

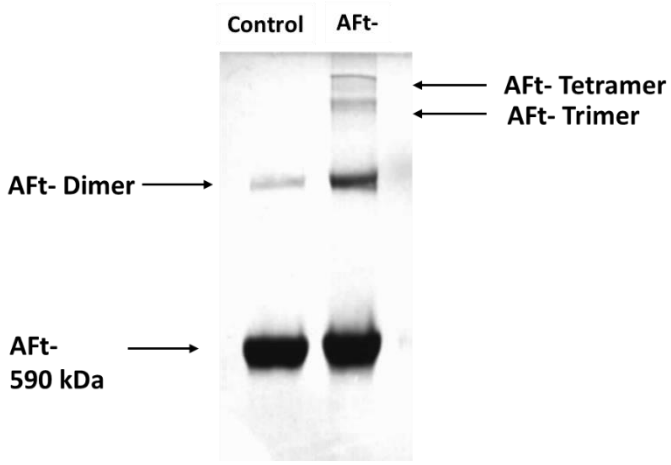


Figure 4.5. A native PAGE gel (10 cm x 10 cm x 1.0 mm, 6% (w/v), 120 V, 3 h) of purified AFt-. The control well was loaded with AFt- provided by Dr Zhang with molecular weight of 590 kDa.

The molecular weight of the prepared AFt- was also measured by MALDI-TOF mass spectrometry (Figure 4.2). The molecular weight was found to be 24521 Da which is comparable to the theoretical value of 24584 Da determined on the ExPASy Proteomics tool based on the amino acid sequence.

The difference between the theoretical and experimental molecular weight could be due to the accuracy of the MALDI-ToF mass spectroscopy to measure the molecular weight of large proteins. In addition, the accurate calibration of the MALDI-ToF could effect on its measuring.[185]

Table 4.1. Properties of cysteine free human heavy chain apoferritin (AFt-). The theoretical data were generated using ProtParam software (ExPASy Proteomics tools).

	No. of amino acids	pI	Theoretical M.wt	MALDI-TOF M.wt
AFt-	211	5.66	24584.33 Da	24521 Da

The size of the AFt capsule is expected to be 12 nm. In order to confirm the formation of the capsule cage, the size of the AFt- was measured using DLS. The hydrodynamic size distribution of the AFt- is shown in Figure 4.6. We noted the hydrodynamic size of the purified AFt- is 13 ± 4 nm, which is in good agreement to the hydrodynamic size of the AFt- measured by the DLS from the literature (12.9 nm).[186] The observed difference between the ideal size (12 nm) and the measured is due to the DLS technique, which determines the hydrodynamic size of the particles, i.e. the size of the capsule with solvent molecules.

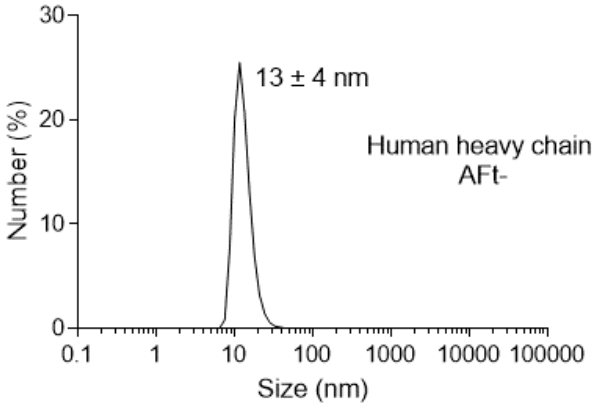


Figure 4.6. Size distribution of AFt- measured by DLS.

The Western blot technique was used to confirm the purified protein has a His-tag. An antibody specific for the His-tag was used to detect the protein (AFt-). A protein containing His-tag and Bovine serum albumin (BSA) were used as positive and negative His-tag control, respectively. The western blot image in Figure 4.7 observed the AFt- subunit (24 kDa) and for the positive control protein (39 kDa). This observation proves the purified protein is the AFt-.

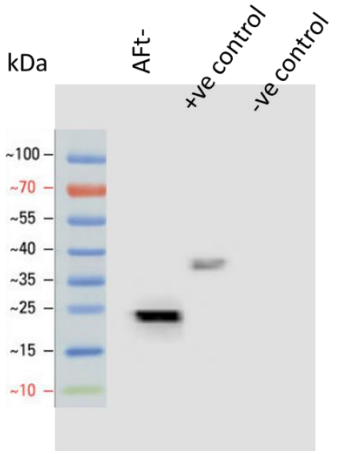


Figure 4.7. A photograph of western blot for the AFt- using the His-tag antibody. The +ve control: protein containing His-tag with molecular weight 39 kDa, -ve control: protein without a His-tag.

The purified AFt- was dialysed twice against 20 mM Tris at pH 8.8 to remove the imidazole and any possible impurity with M.wt < 8 kDa, and to form the cage of the AFt-. The concentration of the AFt- was measured using both nanodrop and Bradford assays and was observed ~ 9.2 mg/mL and 9.0 mg/mL (see Chapter 2.3.5 for details). AFt- was snap frozen in liquid N_2 and stored at T = – 80 ºC.

4.4. Expression and purification of affibody

The affibody with amino acids sequence shown in Figure 4.8 was expressed by *E. coli* (BL21) as described in Chapter 2.3.7. Bacteria was grown in LB broth medium (1 L) and the bacteria were induced to express the protein when the optical density reached ~ 0.6. The culture was then left for 4 hours at 37 ºC.

1 MAHHHHHHSSGLVPRGSLQVDNKFNKEMRNAYWEIALLPNLNNQQKRAFI
50 RSLYDDPSQSANLLAEAKKLNDAQAPKVD

Figure 4.8. Primary amino acid sequence of Afb. His-tag is shown in red.

The Afb was purified from the soluble fraction using the IMAC technique. The SDS PAGE of the Afb indicated a molecular mass ~ 9 kDa (Figure 4.9), which is comparable to the theoretical molecular mass (9.02 kDa) determined by ExPASy website using the amino acids sequence, Table 4.2. The SDS PAGE also indicated a high purity of Afb after purification by the IMAC technique. The concentration of the Afb was measured by nanodrop and Bradford assay, and the measured concentration was 2.5 mg/mL and 2.4 mg/mL, respectively. The final solution of the Afb was filtered through a 0.22 µm syringe filter then snap frozen by liquid N_2 and stored at – 80 ºC.

Table 4.2. Properties of Afb theoretically estimated using ProtParam software (ExPASy Proteomics tools) and measured using the amino acid sequence of the Afb.

	No. of amino acids	pI	Theoretical M.wt	MALDI-TOF M.wt
Afb	79	9.16	9027 Da	9027 Da

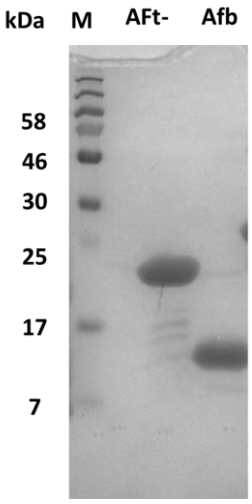
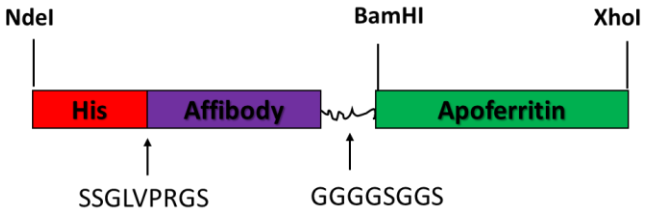


Figure 4.9. SDS PAGE of Afb purified from the soluble fraction. M is molecular weight markers and AFt- is apoferritin.

4.5. Expression and purification of affibody-apoferritin

The Afb-AFt- was expressed by BL21 *E. coli* bacteria as described in Chapter 2. The plasmid DNA was designed with the amino acid sequence described in Figure 4.10. Afb is linked to the N-terminus of the AFt- through a flexible peptide linker (GGGGSGGS), which is rich with glycine and serine residues to increase the polarity of the protein and achieve appropriate separation of the functional domains of both fused proteins.[187] The protein was purified from the non-soluble

fraction using the IMAC chromatography technique as described in Chapter 2.



1 MAHHHHHHSSGLVPRGSLQVDNKFNKEMRNAYWEIALLPNLNNQQKRAF
50 IRSLYDDPSQSANLLAEAKKLNDAQAPKVDGGGGSGGSMTTASTSQVRQ
100 NYHQDSEAAINRQINLELYASYVYLSMSYYFDRDDVALKNFAKYFLHQS
150 HEEREHAEKLMKLQNQRGGRIFLQDIKKPDRDDWESGLNAMEAALHLEK
200 NVNQSLLELHKLATDKNDPHLSDFIETHYLNEQVKAIKELGDHVTNLRK
250 MGAPESGLAEYLFDKHTLGDSDNES

Figure 4.10. Design and the primary sequences of the affibody-apoferritin protein. Red: His tag. Black: Thrombin cleavage site. Black underline amino acid indicates flexible linker between the two fusion proteins.

The purified Afb-AFt- was characterised by SDS PAGE to examine the purity of the protein. An unexpected band was observed at molecular weight of ~ 24 kDa, Figure 4.11. The unexpected band could be result of proteolysis of the Afb-AFt-, therefore, the purification steps did not provide desirable purity. Therefore, gel filtration was used to separate the small molecular size fractions from the main protein after reassembling the Afb-AFt- subunits and forming the cage. However, the purity of the Afb-AFt- as observed in SDS PAGE did not improve. Both gel filtration and Ni-IMAC purification did not result in a single band for the Afb-AFt- in the SDS PAGE.

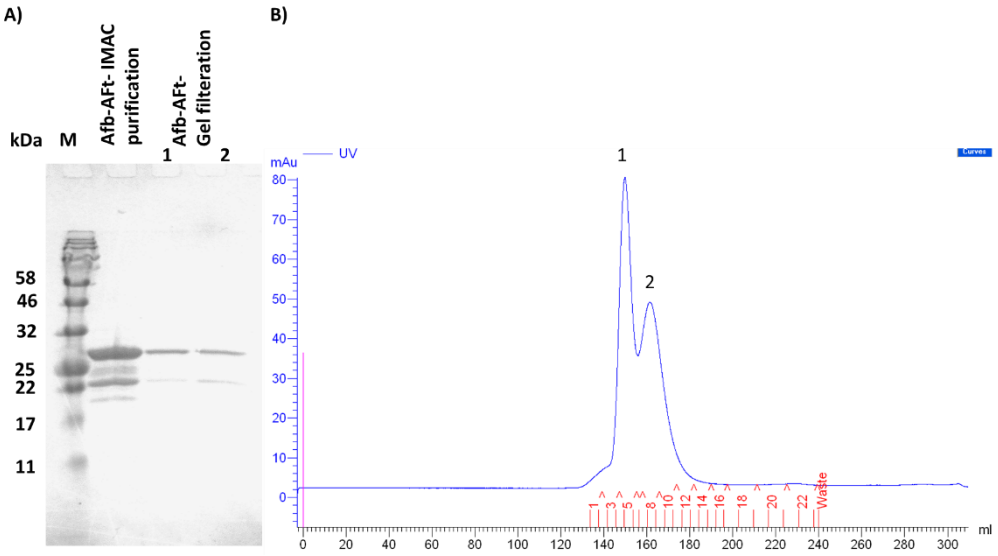


Figure 4.11. A) SDS PAGE of Afb-AFt- expressed by BL21 *E. coli* and purified by IMAC and GEL filtration. B) Absorbance of the Afb-AFt- purified using gel filteration.

The molecular weight of the purified protein was examined by using MALDI-TOF spectrometry and confirmed the results of the SDS. Two peaks with molecular weights of ~ 23 kDa and 30 kDa were observed (Figure 4.12). We envisage that the 23 kDa band observed in the SDS PAGE gel could be due to proteolysis during the expression or the purification of the Afb-AFt-, which should be confirmed in future work by western blot and peptide sequencing.

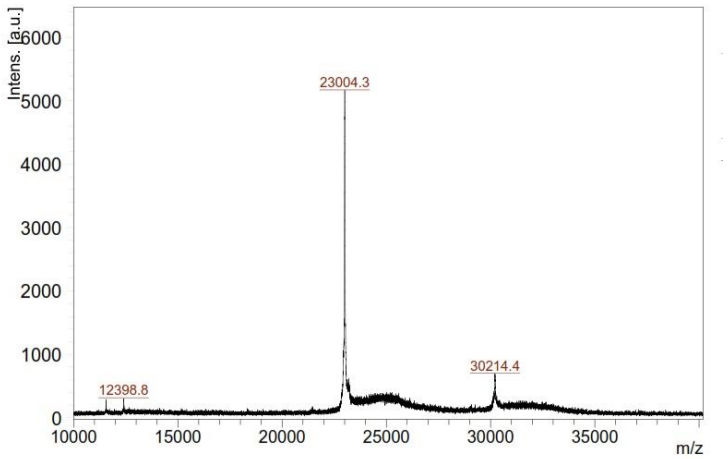


Figure 4.12. MALDI-TOF profile of Afb-AFt-purified from the non-soluble fraction using the IMAC technique.

The existence of the unexpected fragment indicated the importance of optimising the expression and the purification conditions.

4.5.1. Optimisation of the expression and purification of Afb-AFt-.

Different optimisation methods were applied to the Afb-AFt-expression and purification procedures to achieve a pure protein that could be used for further studies. The methods are listed in the table below and this section will present each of the methods' attempted.

Table 4.3. List of expression and purification methods.

Expression	Purification
Replacing the *E. coli* BL21 with LOBSTR cells	Different imidazole concentrations
Lower induction temperature (T = 25 ºC)	Lower the concentration of urea from 8 M to 4 M
Lower IPTG concentration (0.8 mM)	
Replacing LB medium for M9 media	

The expression conditions listed in Table 4.3 were used to improve the expression of the Afb-AFt- and reduce the proteolysis and other contaminants might produce through the expression of the protein. The LOBSTR cells were selected to express the protein instead of the *E. coli* cells. The LOBSTR cells were designed to reduce the expression of the proteins with His-tag < 4.[170]

The kinetic of the protein expression were reduced to improve the expression of the protein. The reduction of the temperature and the concentration of the IPTG were used separately, also M9 mineral media was used instead of the LB media. The temperature was reduced from 37 ºC to 25 ºC during the induction of the bacteria to express the protein to reduce the speed of the expression.

The concentration of the IPTG was reduced from 1 mM to 0.8 mM to induce the bacteria to express the protein. Decreasing the concentration of the IPTG could help to slower the protein expression.

M9 mineral medium consists of the minimal nutritional requirements bacteria need to grow and therefore slows the growth of the culture and the expression of proteins. The M9 mineral medium was used instead of LB to grow the *E. coli* and express Afb-AFt-.

The purification methods were also modified. The concentration of the imidazole was increased in the binding buffer to remove contaminant with His-tag < 4.

All these expression and purification optimisation methods did not produce high purity of Afb-AFt- using the Ni-IMAC and the gel filtration techniques, and the second band was remaining in the SDS PAGE gel and was detected by using MALDI-TOF mass spectroscopy, Figure 4.13.

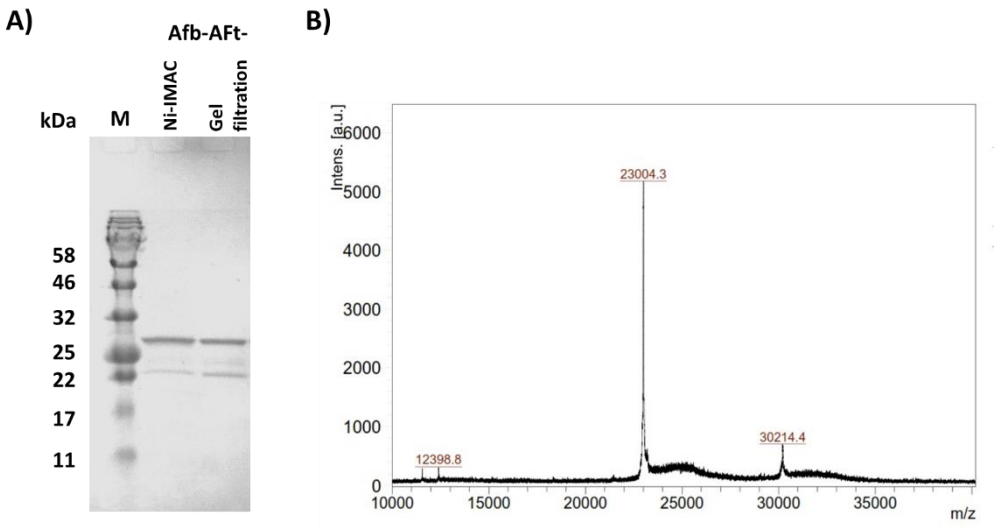


Figure 4.13. A) SDS PAGE gel of the Afb-AFt- expressed by the LOBSTR cells and purified using Ni-IMAC and the gel filteration techniques. B) MALDI-TOF spectrum of the purified Afb-AFt-

Afb-AFt- was purified from the non-soluble fraction by dissolving the protein in a buffer containing 8 M urea. In some cases, a high concentration of urea may result in denaturing the protein, and therefore, a lower concentration of urea was used to dissolve the protein. Buffer with 4 M urea was used during the purification. The purification was repeated at least 3-times using 4 M of urea and the results were promising. The SDS PAGE of the purified Afb-AFt- (Figure 4.14) did not reveal any impurity bands at 23 kDa.

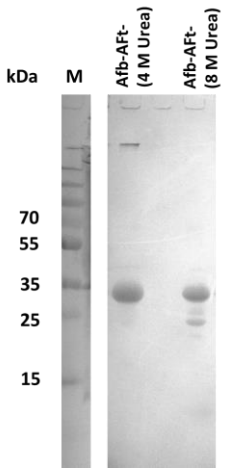


Figure 4.14. SDS PAGE of Afb-AFt- expressed by *E. coli* BL21 bacteria and purified using the IMAC technique. Urea (4 M) was used to dissolve the non-soluble protein and was compared to 8 M.

The size of the purified Afb-AFt- was examined by the DLS. The folded protein had an average size distribution of 14 ± 5 nm (Figure 4.15), which is comparable to the size of AFt- (12 nm).

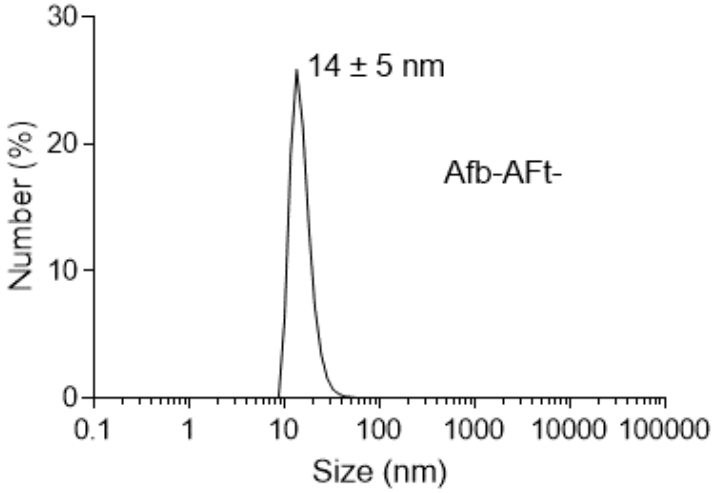


Figure 4.15. Size distribution profile of Afb-AFt- measured by DLS at room temperature.

These previous results suggest that the best conditions to purify the Afb-AFt- was by using low concentrations of urea in the purification buffers.

The purified protein was dialysed twice against 2 L of 20 mM Tris buffer at pH 9.0 then filtered through a 0.22 μm sterile syringe filter before being snap frozen in liquid N_2 and stored at – 80 ºC to be used for further studies.

4.5.2. Preparation of Afb-AFt- with 4 Afb copies

Afb-AFt- consists of 24 polypeptide subunits that can be disassembled and reassembled by changing the pH, and each subunit contains an affibody linked at the N-terminus. The Afb-AFt- cage contains 24 affibodies attached to the surface of the cage. In this study, a cage with ~ 4 copies of affibody per cage was required. Therefore, both proteins, AFt- and Afb-AFt-, were used to achieve a cage with 4 copies of Afb on the AFt- surface.

AFt- and Afb-AFt- were mixed with an AFt-:Afb-AFt- molar ratio of 20:4 to prepare the cage. The procedure used for preparing both proteins and mixing is described in Chapter 2.3.8. The molecular weight of the formed protein was characterised by native PAGE and compared to the AFt- cage. The native PAGE indicated that size of the Afb-AFt- with 4 Afb copies was slightly higher than the AFt- cage (Figure 4.16). The prepared protein concentration was measured using the Bradford assay and the protein was snap frozen in liquid N_2 and stored at T = – 80 ºC for further studies.

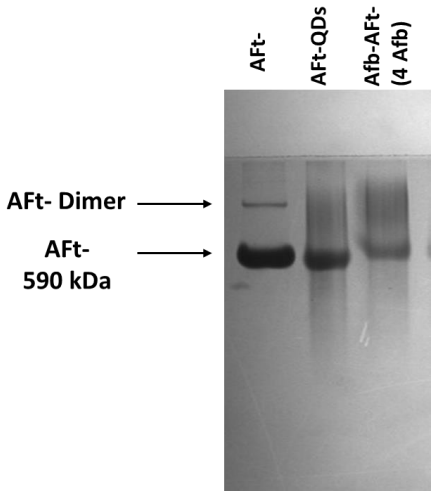


Figure 4.16. A native PAGE (10 cm x 1.0 mm, 6% (w/v), 120 V, 3 h) of Afb-AFt- with 4 Afb copies compared to AFt- cage and AFt-QDs.

The hydrodynamic size of Afb-AFt- was measured using DLS. The observed protein size with an average diameter of 15 ± 4 nm is monitored, which is comparable to the size of the AFt- which mean the protein is folded and the AFt- cages with Afb copies on the surface is formed, Figure 4.17.

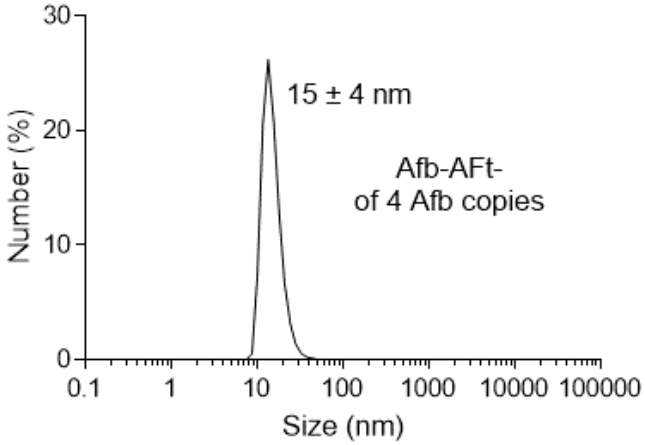


Figure 4.17. Size distribution profile of Afb-AFt- of 4 Afb copies measured by DLS at room temperature.

4.6. Conclusions

In order to achieve high purity and high concentrations of AFt- and Afb-AFt-, they were expressed by *E. coli* bacteria, at *T* = 37 ºC and IPTG concentration of 1 mM. In addition, pure Afb-AFt- was achieved by reducing the urea concentration form 8 M to 4 M in the purification buffers. Therefore, lower concentration of urea was used to reduce the protein proteolysis.

Afb-AFt- with an average of 4 Afb copies was prepared by reassembling AFt- cage from a mixture of AFt- and Afb-AFt-. The molecular weight of Afb-AFt- of an average 4 Afb copies was confirmed by comparing it with the AFt- cage using native PAGE. Also, the hydrodynamic size of the same protein was determined by DLS and found to be ~ 15 nm. The new structure of the Afb-Aft- of an average of 4 Afb copies has the ability of the encapsulation and the selectivity of Afb toward the HER2 receptors which will be presented in Chapters 5 and 6. Therefore, both AFt- and Afb-AFt- of 4 Afb copies cages are interesting to encapsulate the synthesised PbS QDs.

Chapter 5

5. Encapsulation of PbS QDs

5.1. Encapsulation methods

Apoferritin has been used in different biological studies as a carrier for drugs and contrast agents. Apoferritin may protect its cargo from degradation inside the blood stream or inside the living cells. in addition, AFt can sustainably release its cargo inside the targeted cells in the lysosome.[188,189] Therefore, apoferritin was used to encapsulate the PbS QDs.

Two routes have been used previously to encapsulate PbS QDs inside the apoferritin cages: pH dependent reassembly and nanoreactor.[177] The pH dependent reassembly method requires disassembling the apoferritin into its 24 polypeptide subunits by reducing the pH to < 3.5 and then reassembling the cage by increasing the pH to > 5.0. The nanoreactor method uses the threefold hydrophilic channels in the AFt- cage to diffuse the Pb^{2+} and S^{2-} ions inside the protein cage and grow the QDs inside the cage.[128,190]

An alternative urea-induced disassembly method has been reported in the literature to encapsulate up to 28 molecules of doxorubicin anticancer drug derivatives.[191] Urea with a concentration of 8.0 M has been used to dis-assemble the AFt- cage to its polypeptide subunits. It was reported that after encapsulation using this method, only insignificant drug leakage was observed during the first one or two

days. The encapsulation of doxorubicin by apoferritin results in formation of water soluble solution and the structure of the apoferritin was not affected.[192] Therefore, this method was also employed to encapsulate the QDs.

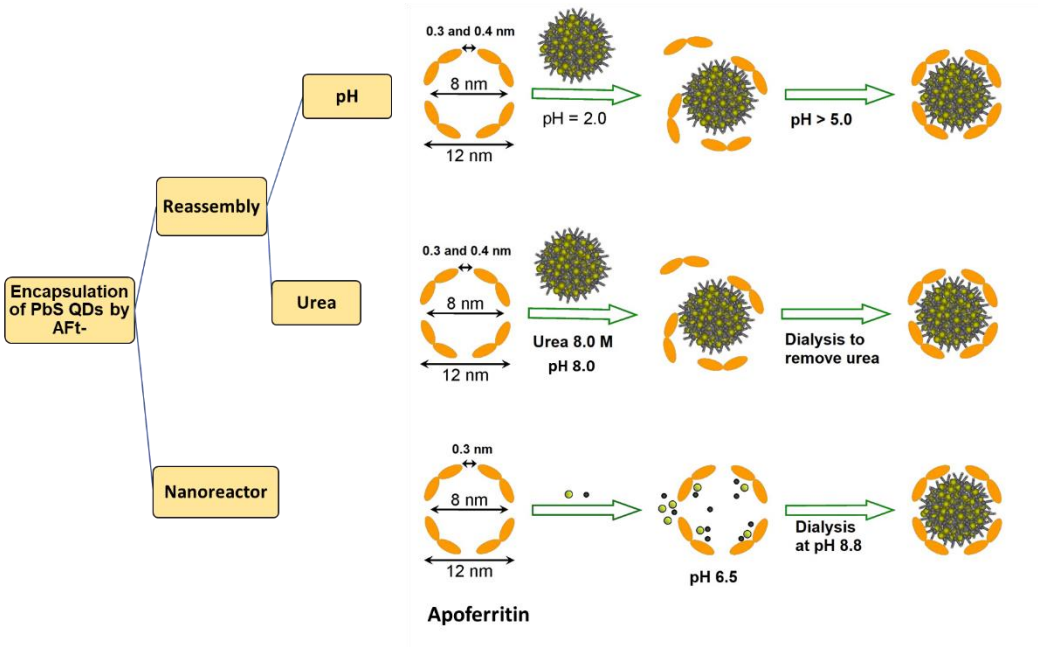


Figure 5.1. A scheme presenting the three possible encapsulation routes used to encapsulate the PbS QDs into AFt- cages.

Cysteine free human heavy chain apoferritin (AFt-) and affibody-apoferritin (Afb-AFt-) with an average of 4 Afb copies each were prepared and purified as described in Chapter 4. AFt- and Afb-AFt- were used separately to encapsulate the synthesised PbS QDs capped with L-Cys, L-CysOMe, TGA/L-CysOMe or GSH capping ligands. QDs were encapsulated following 3 routes, pH reassembly, urea reassembly and nanoreactor (Figure 5.1). Each encapsulation was repeated at least 3-times to assess the reproducibility of the encapsulation.

Because AFt- has no fluorescence in the same region as the PbS QDs, the optical activity of the QDs was monitored after the encapsulation to indicate if the encapsulation had an effect on the λ_{max} emission of the QDs. The optical properties were examined by recording the PL emission after the encapsulation. In addition, native PAGE gels were ran after the encapsulation to confirm the protein molecular weight compared to the original protein used. The size distribution of the encapsulated QDs were determined by using the DLS.

5.2. Human heavy chain apoferritin encapsulated PbS QDs

5.2.1. L-Cys PbS QDs and L-CysOMe PbS QDs

L-Cys PbS QDs were synthesised with a Pb:L-Cys:S molar ratio of either 1:2.5:0.3 or 1:2.5:0.8. The nanocrystal diameter was estimated to be ~ 4 nm, using PL energy dependence on QD size (Figure 1.4), and PL peak position at ~ 900 nm. To the best of our knowledge, L-Cys PbS has not been encapsulated in a protein cage before. Human heavy chain apoferritin (AFt-) was used to encapsulate and the encapsulation was performed following the pH reassembly method. However, the QDs were not successfully encapsulated by the AFt- and the solution precipitated after ~ 2 hours. The likely reason for that is the high negative charge on the L-Cys PbS QDs. QDs were repelled from the negative charge on the AFt- interior. Indeed, the potential measurements indicated that QDs had − 50 mV potential for the L-Cys PbS QDs solution. The AFt- cage

has a negative charge due to the presence of significant numbers of aspartate and glutamate on the interior surface.

In order to alter the potential negative charge, we have modified the surface of the PbS QDs with another ligand with a lower negative charge. The L-CysOMe capping ligand was selected to reduce the negative charge on the QDs and to encapsulate them inside the AFt-cage.

L-CysOMe capped PbS QDs with a Pb:L-CysOMe:S molar ratio of 1:6:0.3 were used and had PL peak position at 920 nm. Encapsulation was attempted by both pH reassembly and nanoreactor methods.

The optical stability of the AFt-QDs was examined by monitoring their PL wavelength. AFt-QDs were found optically stable for at least 5 days in colloidal solution with a PL peak position detected at ~ 900 nm (Figure 5.2). The PL peak position of the PbS QDs did not change following encapsulation, indicating that the presence of AFt- cage did not affect the size and/or confinement of the PbS QDs.

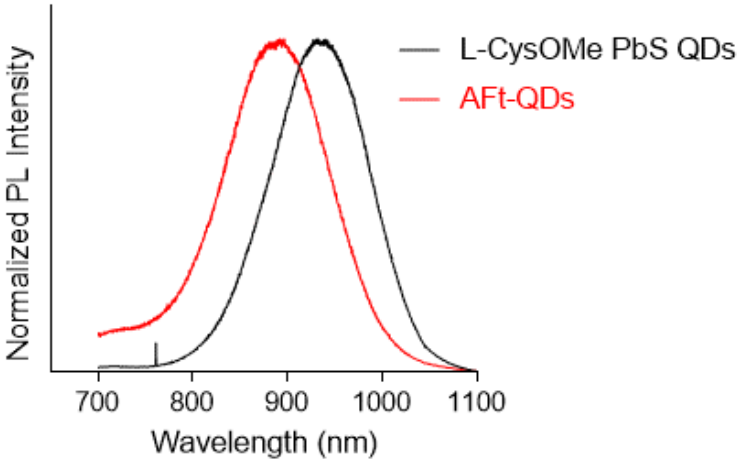


Figure 5.2. Room temperature PL spectra of AFt- encapsulated L-CysOMe PbS QDs prepared via the pH reassembly route. PbS QDs used were prepared with Pb:L-CysOMe:S molar ratios of 1:6:0.3.

From the native PAGE in Figure 5.3 we observed that AFt-QDs passed through the gel more quickly than the AFt- capsule. There are two possible reasons: (i) the AFt- did not refold correctly after mixing with the QDs; (ii) the interaction of the QDs core with the AFt- interface lead to charge redistribution and change in the overall surface charge of AFt-, hence affecting the migration of the construct through the gel. Therefore, it was concluded that the pH reassembly method is not suitable for encapsulation of L-CysOMe PbS QDs.

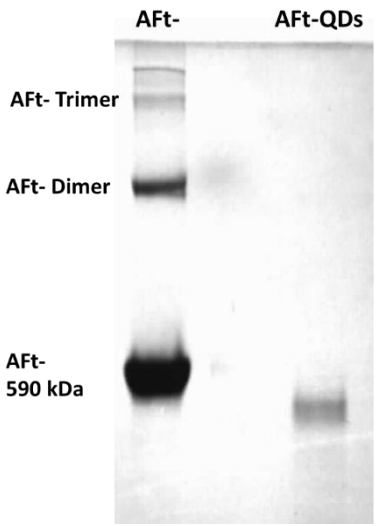


Figure 5.3. Native PAGE gel (10 cm x 10 cm x 1.0 mm, 6% (w/v), 120 V, 3 h) for AFt- and AFt- encapsulated L-CysOMe PbS QDs by following the pH reassembly route. L-CysOMe PbS QDs used were produced with Pb:L-CysOMe:S molar ratio of 1:6:0.3.

To avoid the unsuccessful encapsulation observed with the pH reassembly route, the nanoreactor route was used to encapsulate L-CysOMe PbS QDs. The PL emission of the PbS QDs following the encapsulation via nanoreactor route was undetectable; however, the native PAGE gel gives a band at the same position as for apoferritin (Figure 5.4), confirming the presence of QDs in the interior protein cage rather than outside. This encapsulation was attempted three times, but the PL emission was not detectable. These results suggest that PbS QDs were not successfully formed inside the AFt- cavity.

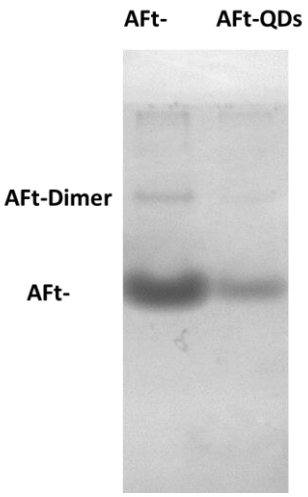


Figure 5.4. A native PAGE (10 cm x 10 cm x 1.0 mm, 6% (w/v), 120 V, 3 h) for the AFt- and AFt-PbS QDs encapsulated by using the nanorector route. PbS QDs used have Pb:L-CysOMe:S molar ratio of 1:6:0.3.

5.2.2. TGA/L-CysOMe PbS QDs

QDs capped with mixture ligands (TGA/L-CysOMe) were chosen for the encapsulation due to their stability and promising fluorescence in the NIR. In addition, the existence of the L-CysOMe with the surface ligands may reduce the negative charge of the QDs and increase the possibility for the encapsulation by the AFt- cage. TGA/L-CysOMe PbS QDs were synthesised with molar ratio of Pb:TGA:L-CysOMe:S of 1:1.5:1:0.3.

The protein capsules of AFt- were used to encapsulate the PbS QDs following the pH reassembly and the nanoreactor routes. The observed λ_{max} emission peaks of the QDs and AFt-QDs of both encapsulation routes are shown in Figure 5.5. The λ_{max} emission peak of the QDs was observed at ~ 890 nm and for AFt-QDs encapsulated using pH reassembly and nanoreactor routes, the PL peak positions

was at ~ 900 and 925 nm, respectively. The PL peak position, λ_{max}, for the QDs has not changed significantly, which means the QDs size is comparable. In addition, the wavelengths of PL emission of the PbS QDs after the encapsulation have remained in the 1st NIR region of the interest optical window.

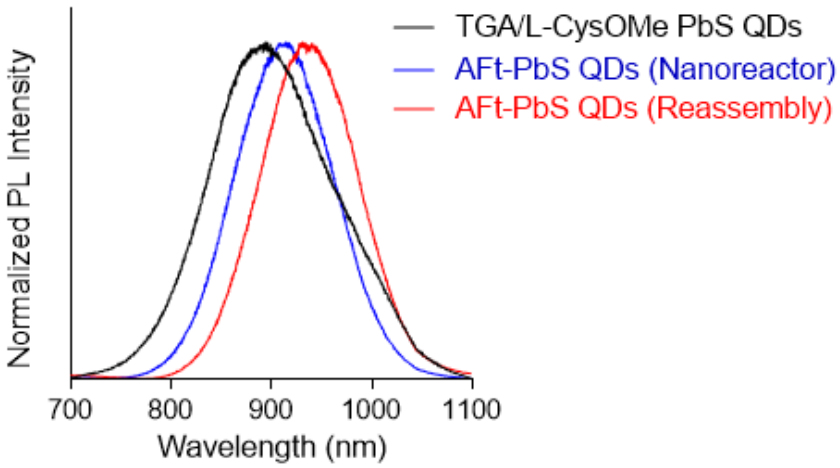


Figure 5.5. Room temperature PL emission spectra of TGA/L-CysOMe PbS QDs with Pb:TGA:L-CysOMe molar ratios of 1:1.5:1:0.3 (black), PL spectra of the PbS QDs encapsulated by AFt- following the pH reassembly (red) and nanoreactor (blue) routes.

The AFt-QDs solution of both encapsulation routes were analysed using native PAGE gels to examine the protein size after the encapsulation and to ensure that the QDs were not attached to the protein surface. The AFt-PbS QDs composite was ran at the same pH as the AFt-, pH 8.8, to reduce the effect of the surface charge of the AFt-. The native PAGE gel in Figure 5.6 for the AFt-PbS QDs solutions prepared using both routes reveals bands at the same molecular

weight as that of empty AFt-, which indicates the reforming of the AFt- and encapsulation of the QDs inside the cage.

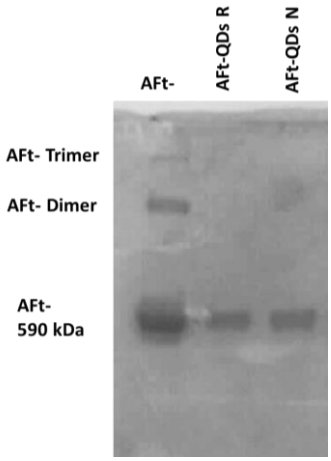


Figure 5.6. A native PAGE (10 cm x 10 cm x 1.0 mm, 6% (w/v), 120 V, 3 h) for the AFt- and AFt-PbS QDs encapsulated by the pH reassembly (AFt-QDs R) and nanoreactor (AFt-QDs N) methods.

The hydrodynamic size of the AFt-QDs was examined using DLS. The size observed for the AFt-QDs was 14 ± 6 nm, which is comparable to the size of the empty AFt- capsule (13 ± 4 nm) used for the encapsulation (Figure 5.7). These results confirm that the QDs are located inside the protein capsule rather than attached to the exterior of the AFt-.

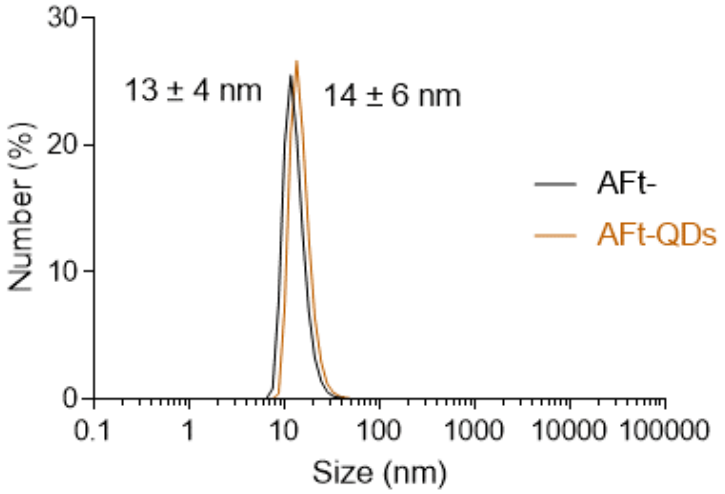


Figure 5.7. Size distribution of AFt-PbS QDs and AFt- measured by DLS at room temperature. The QDs were encapsulated by the pH reassembly method.

The diameter of the encapsulated PbS QDs by AFt- was examined by TEM to estimate the size and the distribution of the QDs. The TEM image of AFt-PbS QDs, Figure 5.8, presents some QDs with size ~ 4 ± 1 nm. According to the observed size of the QDs, we can estimate a high probability of the QDs encapsulation by AFt-. The TEM grid is hydrophobic and the QDs crystals are in aqueous solution, therefore, QDs were clustering and it is difficult to resolve individual QDs.

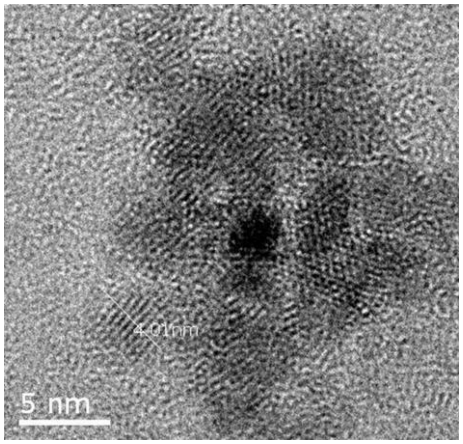


Figure 5.8. A TEM image for the AFt-PbS QDs composition without the use of uranyl acetate staining. The TGA/L-CysOMe PbS QDs were encapsulated by the pH reassembly method.

The urea reassembly method was also used to encapsulate the TGA/L-CysOMe PbS QDs. This route has not previously been used to encapsulate the PbS QDs. The PL peak positions of the AFt-PbS QDs solution was comparable to that of QDs alone, with small (~ 30 nm) red shift, shown in Figure 5.9.

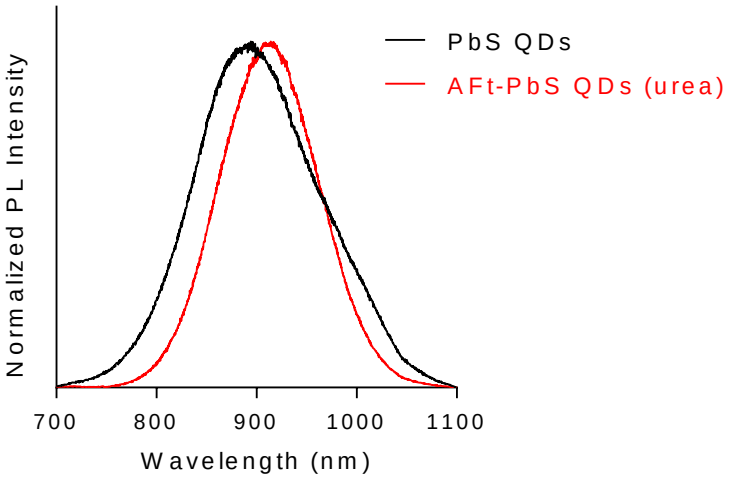


Figure 5.9. Room temperature PL spectra of TGA/L-CysOMe PbS QDs and AFt-PbS QDs encapsulated by the urea reassembly method.

The encapsulation of the QDs following pH reassembly, nanoreactor and urea route methods were stable in solution over a period of at least 14 days. However, the encapsulation by the pH reassembly was produced with higher concentration and higher intensity and therefore, the pH reassembly route is more preferable for the encapsulation. We concluded that the TGA/L-CysOMe PbS QDs were encapsulated successfully by AFt- following all used encapsulation routes.

5.2.3. GSH PbS QDs

GSH PbS QDs are of interest in bioimaging due to their stability and optical activity. Also, the potential properties of the GSH capping ligand and its usage to reduce the effect of the oxidative stress inside the living tissues means the GSH PbS QDs are promising for bioimaging. AFt- was used to encapsulate GSH PbS QDs synthesised with molar ratio of Pb:GSH:S of 1:2:0.5 with a PL emission at ~ 850 nm.

The pH reassembly and urea reassembly routes were used to perform the encapsulation. The QDs were synthesised at pH 6.5 to achieve λ_{max} emission < 900 nm, and therefore it was important to keep the pH in the range between 6.0–7.0 during the encapsulation process to prevent their precipitation and deterioration of optical properties. The AFt- at pH 2.0 was added to the QDs slowly under vigorous stirring with a controlled pH (6.0–7.0). After the encapsulation, the AFt-PbS QDs were dialysed against 20 mM Tris buffer (2 L) at pH 8.6 twice to remove the excess un-encapsulated QDs. The final solution of AFt-

QDs were stored at pH 8.6 because AFt- is highly stable at this pH. In addition, the emission of the encapsulated QDs should not be affected by increasing the pH of the encapsulation solution to > 7.0 due to their encapsulation inside the AFt- cage.

The PL studying revealed a λ_{max} emission peak of AFt-QDs at ~ 910 nm, which is comparable to the λ_{max} of the GSH PbS QDs (860 nm), Figure 5.10. The red shift of ~ 50 nm is likely due to the growth of the QDs even during the encapsulation process or inside the AFt- cage after the encapsulation. However, the λ_{max} emission of the AFt-QDs are in the same region of the optical window. These results are in agreement with the literature in regards to the efficient encapsulation of QDs inside the Aft- cage and protecting their optical emission.[177]

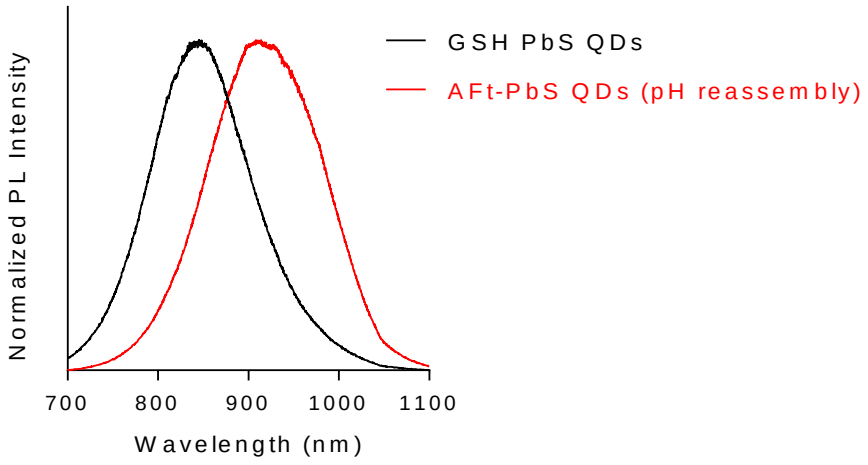


Figure 5.10. Room temperature PL spectra of GSH PbS QDs and AFt-PbS QDs. The encapsulation was performed using the pH reassembly route.

The molecular weight of the AFt-QDs was examined by native PAGE gel. The gel indicated that the AFt- reformed the cage in the encapsulation solution and had a band at the same level as AFt-, which indicates correct reforming of the AFt- cage.

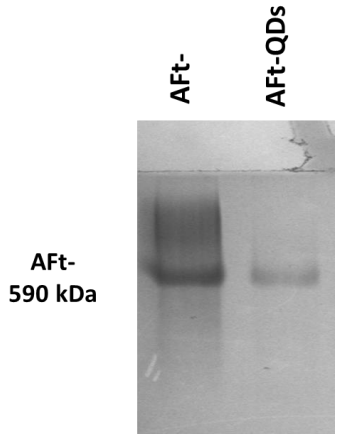


Figure 5.11. A photograph of a native PAGE (10 cm x 10 cm x 1.0 mm, 6% (w/v), 120 V, 3 h) of AFt- and AFt-PbS QDs. GSH PbS QDs were encapsulated by using the pH reassembly route.

GSH PbS QDs were encapsulated inside the AFt- cage using the urea reassembly method. The PL emission was measured after the encapsulation and the observed results showed red shift of PL peak position, as shown in Figure 5.12. This shift from 850 nm for PbS QDs to 910 nm for AFt-QDs is likely due to an increase of the QD size during the encapsulation.

The PL spectra of GSH PbS QDs encapsulated into the AFt- using both the pH reassembly and the urea route revealed red-shifts of the PL line, which is significantly larger compared to the TGA/L-CysOMe PbS QDs. We attribute this shift to the effect of the pH on the size of the QDs: during encapsulation, the pH is changed from pH 6.0 to pH 8.0

which could affect the binding of the ligands to the QDs surface, allowing nanocrystal growth.

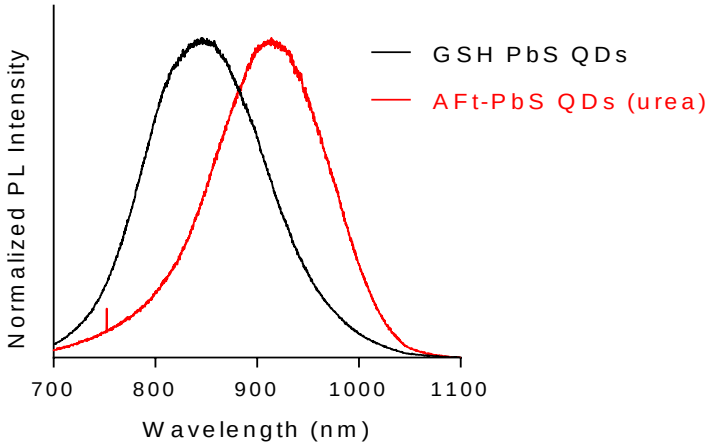


Figure 5.12. Room temperature PL emission spectra of GSH PbS QDs and AFt-PbS QDs. The AFt-PbS QDs was prepared by the urea route.

A native PAGE gel was run to examine the molecular weight of the AFt-. As seen in Figure 5.13, the AFt-PbS QDs exhibited a band at the same molecular weight as that of the empty AFt- capsule. These results confirm correct reassembly of the AFt- following QD encapsulation procedure.



Figure 5.13. A photograph of native PAGE (10 cm x 10 cm x 1.0 mm, 6% (w/v), 120 V, 3 h) of AFt- and AFt-PbS QDs. AFt-PbS QDs was prepared by using the urea method.

The hydrodynamic size of the AFt-QDs was determined by the DLS to be 13 ± 4 nm, which is comparable to the size of the empty cage. These results confirmed that the AFt- capsule reformed in the encapsulation solution. The observed results indicate the high possibility of the QDs to be encapsulated by the AFt-.

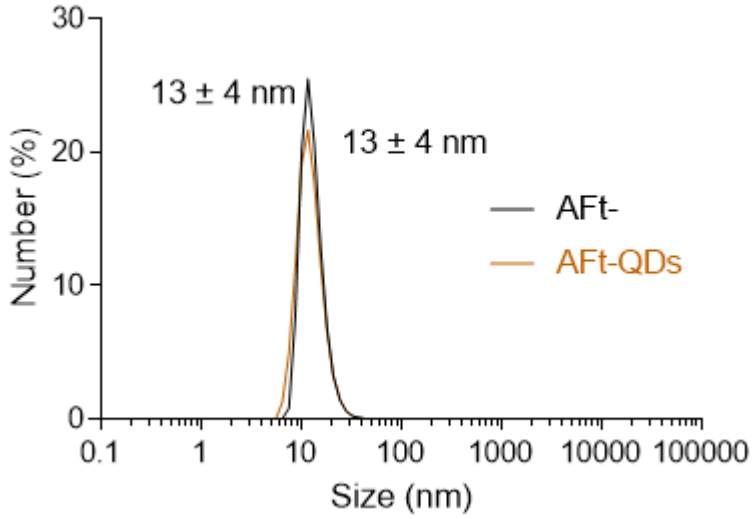


Figure 5.14. Hydrodynamic size distribution of AFt-QDs and AFt- measured by DLS. GSH PbS QDs were encapsulated by pH reassembly.

5.3. Affibody-apoferritin encapsulated PbS QDs

5.3.1. TGA/L-CysOMe PbS QDs

Afb-AFt- with an average of 4 Afb copies was used to encapsulate PbS QDs. Afb-AFt- was prepared and characterised as described in Chapter 4.5.2. The pH reassembly method was used for the encapsulation with Afb-AFt-. The PL emission wavelength was measured after each encapsulation for the QDs and the Afb-AFt- PbS QDs to examine the optical stability after encapsulation. In addition, a native PAGE gel was ran to confirm the protein folded correctly after the encapsulation.

The PL spectra of the PbS QDs are shown in Figure 5.15, and reveal a red shift of λ_{max} of the QDs from 850 nm to 890 nm after the encapsulation by Afb-AFt-. This shift in the λ_{max} of the Afb-AFt-QDs

can be a result of the Ostwald ripening during the encapsulation process. The protein cage can limit the size of the QDs inside the cage and prevent the Ostwald ripening of the QDs. However, Afb-AFt-QDs are optically active in the 1st NIR of the electromagnetic spectrum.

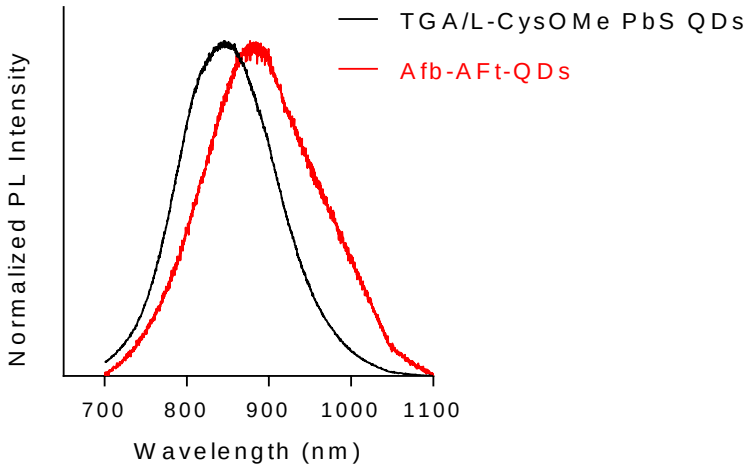


Figure 5.15. Room temperature PL emission spectra of TGA/L-CysOMe PbS QDs and Afb-AFt-PbS QDs. The encapsulation was performed by pH reassembly method.

A native PAGE gel was run to compare the size of the Afb-AFt-PbS QDs with the size of the empty cage Afb-AFt-. The native gel, Figure 5.16, revealed the size of the Afb-AFt- and Afb-AFt- PbS QDs with molecular mass of ~ 611 kDa (AFt- and 4 Afb) compared to the AFt- of the molecular mass ~ 590 kDa. These results show the proteins are correctly formed after the encapsulation and the PbS QDs are more likely to be encapsulated inside the Afb-AFt- cages rather than outside the cage.

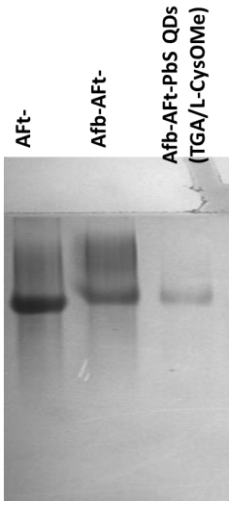


Figure 5.16. A native PAGE gel (10 cm x 1.0 mm, 6% (w/v), 120 V, 3 h) of the Afb-AFt-PbS QDs and the empty cages of AFt- and Afb-AFt- (4 Afb copies). The TGA/L-CysOMe PbS QDs were encapsulated using the pH reassembly method.

Furthermore, the size of the Afb-AFt-PbS QDs was determined by DLS. The hydrodynamic diameter of the Afb-AFt- PbS encapsulation solution is ~ 15 ± 4 nm, which is comparable to the hydrodynamic diameter of the Afb-AFt-, Figure 5.17. The Afb-AFt-QDs were stable in solution for at least 10 days.

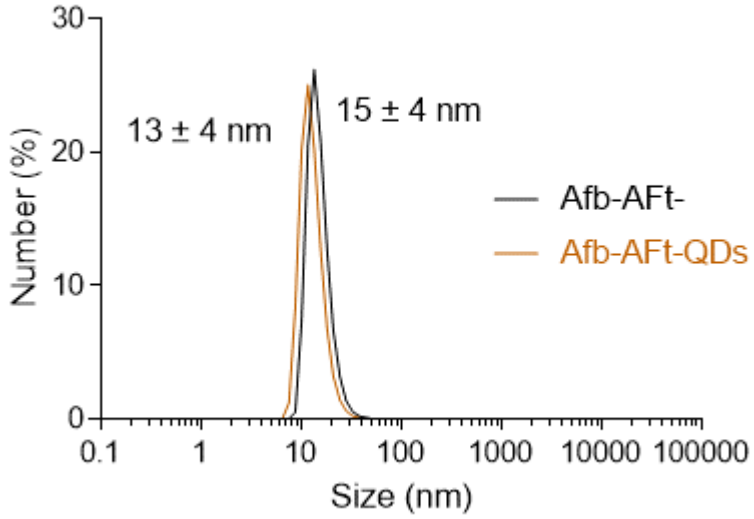


Figure 5.17. Size distribution of Afb-AFt-PbS QDs and Afb-AFt-measured by DLS. TGA/L-CysOMe PbS QDs were encapsulated by pH reassembly method.

5.3.2. GSH PbS QDs

GSH PbS QDs were encapsulated by Afb-AFt- following the pH reassembly method. The PL measurements indicated a small (25 nm) red shift of PL emission, Figure 5.18, where PL emissions ~ 950 nm were obtained for the QDs after the encapsulation. The Afb-AFt-PbS QD solution was stable for at least 2 weeks.

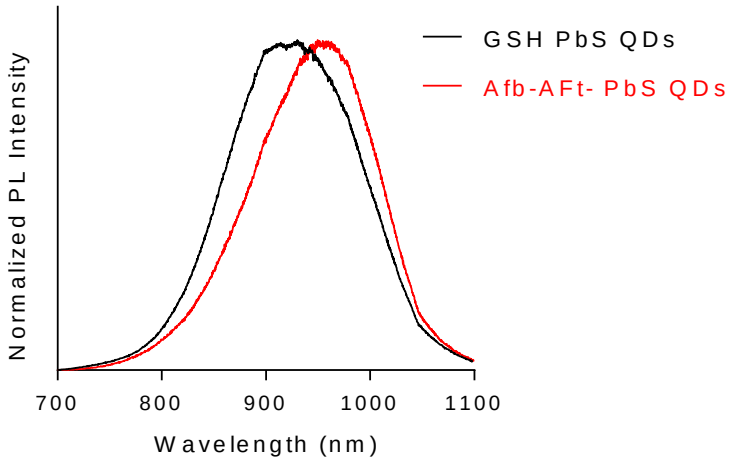


Figure 5.18. Room temperature PL emission spectra of GSH PbS QDs and Afb-AFt-PbS QDs. The encapsulation was performed by the pH reassembly method.

A native PAGE gel revealed the band of comparable molecular weight for the AFt-, Afb-AFt- and Afb-AFt-QDs (Figure 5.19), with the size of ~ 590 kDa for AFt- and ~ 611 kDa for Afb-AFt-. This result confirms that the Afb-AFt- cage reformed after the encapsulation.

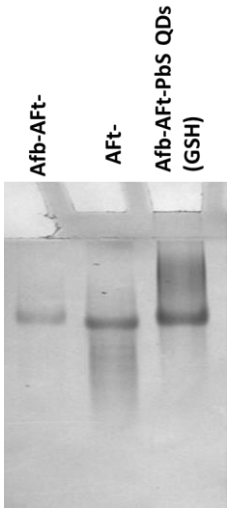


Figure 5.19. A photograph of a native PAGE (10 cm x 1.0 mm, 6% (w/v), 120 V, 3 h) of Afb-AFt-PbS QDs compared to AFt- and Afb-AFt- empty cages.

Afb-AFt-QDs with a hydrodynamic size 15 ± 4 nm were observed by DLS, which confirmed the formation of protein cage and the encapsulation of the QDs inside the cage rather than on the surface as seen in Figure 5.20.

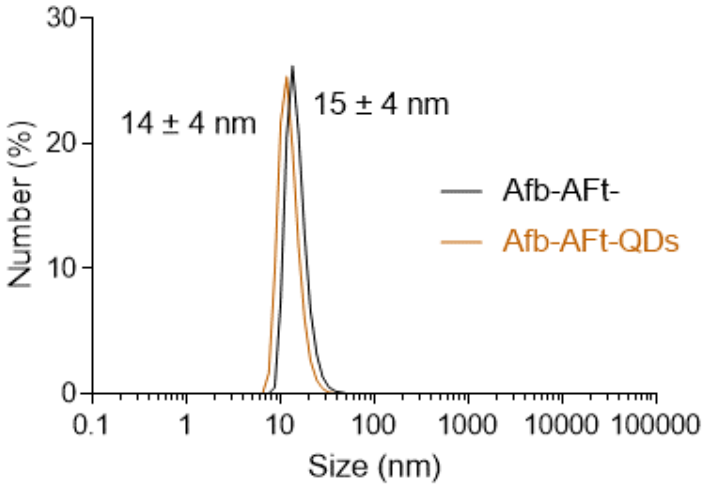


Figure 5.20. Size of Afb-AFt-QDs and Afb-AFt- measured by DLS. GSH PbS QDs were encapsulated by pH reassembly.

5.4. Conclusions

PbS QDs with diameter ~ 4 nm and passivated with TGA/L-CysOMe and GSH capping ligands were used for encapsulation in AFt- and Afb-AFt- (of 4 Afb copies) cages. The size and the charge of the QDs enables efficient encapsulation. We found PbS QDs with smaller size and less negative charge are more promising for the efficient encapsulation. The PL emission of the QDs was examined to confirm the stability of the QDs after the encapsulation. The molecular weight of the used protein was confirmed using the native PAGE gel, and the

size distribution was confirmed by the DLS to examine the size of the proteins after the encapsulation.

The encapsulations into AFt- capsule were efficiently achieved using the pH reassembly, nanoreactor and urea reassembly routes. The urea reassembly route was used for the first time to encapsulate the PbS QDs. The pH reassembly routes was resulted more efficient encapsulation in AFt-.

For the QDs encapsulation by the Afb-AFt- of 4 Afb copies, the pH reassembly method was used to prevent possibility of the protein degradation by the usage of 8 M of urea to decompose the protein cage.

Both TGA/L-CysOMe PbS QDs and GSH PbS QDs were successfully encapsulated into the AFt- and Afb-AFt- and the PL studies exhibited high stability in PL emission for the QDs before and after the encapsulation. The TGA/L-CysOMe PbS QDs exhibited higher PL stability than the GSH PbS QDs after the encapsulation by both proteins which is more likely due to the effect of the pH on the PL emission of the GSH PbS QDs. In addition, the native PAGE and the DLS confirmed the correct forming of the cages after the encapsulation.

Finally, we can say TGA/L-CysOMe and GSH PbS QDs encapsulated by AFt- and Afb-AFt- of 4 Afb copies are interesting to examine their toxicities on tumorous cells.

Chapter 6

6. Cytotoxicity studies of PbS QDs

6.1. *In vitro* studies of PbS QDs

Previous *in vitro* studies of PbS QDs in different cancer cells focused on understanding the cytotoxic effect of the QDs. PbS QDs encapsulated by horse spleen AFt were also used to treat different types of breast cancer cells. It has been reported that AFt-QDs had a cytotoxic effect on cancer cells with GI_{50} > 0.2 mg/mL;[48] however, non-tumour cells were not affected by the AFt-PbS QDs. That study suggested that the effect of the QDs resulted from increases in ROS and exposure to QDs induced apoptotic cell death.[193,48] The same QDs were used to treat colorectal cancerous cells and showed the toxic effect of the QDs occurred at GI_{50} ~ 0.07 mg/mL.[135]

In this study, we performed *in vitro* studies to explore the effect of the synthesised QDs and their encapsulation on cancer cells. MTT assays were used to examine the viability of the cancer cells after treatment with the PbS QDs (see Chapter 2.5.2). Two proteins, cysteine free human heavy chain apoferritin (AFt-) and human heavy chain apoferritin-affibody (Afb-AFt-) of 4 Afb copies, were selected as delivery vehicles for the PbS QDs due to their affinity to the transferrin receptors (TfR1) and to human epidermal growth factor (HER2 receptors), respectively.

This chapter will present the effect of the carrier proteins on the selected cancer cells and then the effect of PbS QDs with and without encapsulation by the cage proteins.

AFt- exhibited non-toxic results on the MDA-MB-231 cancer cells and showed an inhibitory effect on the SKBR3 cells at a concentration of ~ 0.3 mg/mL. On the other hand, the Afb-AFt- exhibited a non-toxic effect on both the MDA-MB-231 and SKBR3 cell lines with concentrations > 1.0 mg/mL.

Two types of PbS QDs were used in this study, TGA/L-CysOME PbS QDs and GSH PbS QDs due to their stability and successful encapsulations in both AFt- and Afb-AFt- cages. The dose dependence of the PbS QDs, proteins alone and the encapsulated QDs were examined. Serial dilutions (0.001, 0.01, 0.05, 0.1 and 0.2 mg/mL) of PbS QDs and corresponding concentrations of other proteins (Table 2.10) were used to expose the cells for a period of 72 h. Cell viability was examined using the MTT assay and the results were analysed and the growth inhibition values (GI_{50}) were calculated as described in Chapter 2.5.2.

6.2. Cytotoxicity of AFt-, Afb and Afb-AFt-

The internalization of AFt- into the cell is mediated by TfR1 (H-chain subunits) and SCARA5 (L-chain subunits) and involves clathrin-mediated endocytosis (also called receptor-mediated endocytosis).[194] The mechanism of the uptake starts with cell signalling to membrane receptors to facilitate protein uptake. AFt- receptors uptake the

heavy AFt- and then the clathrin polypeptides link to the adapter complex of the receptors. Then, clathrin polypeptides coat the protein to allow it inside the cell cytoplasm into the endosome.[95]

Human heavy chain AFt- and Afb-AFt- have been used as capsules to protect the cells from the QDs and to deliver the QDs specifically to the cancer cells. Therefore, their effect should be examined on the cancer cells.

1. Cysteine free human heavy chain apoferritin (AFt-)

AFt- has a high affinity to transferrin receptors on the cell membrane of breast cancer cells.[113] In order to use AFt- as a carrier it should not have a toxic effect on the cells. Therefore, a series of concentrations of 0.0072, 0.072, 0.36, 0.72, 1.44 mg/mL of AFt- were applied to the cancer cells.

The graph in Figure 6.1 A shows the effect of the protein on the viability of MDA-MB-231 cells. At high concentrations (> 0.7 mg/mL) it can be seen there is a slight effect on cell viability; however, significant toxicity was not observed for concentrations up to 1.44 mg/mL. These results are in agreement with the previous results that indicated that AFt- up to a concentration of 0.5 mg/mL showed a non-toxic effect (unpublished results).[167]

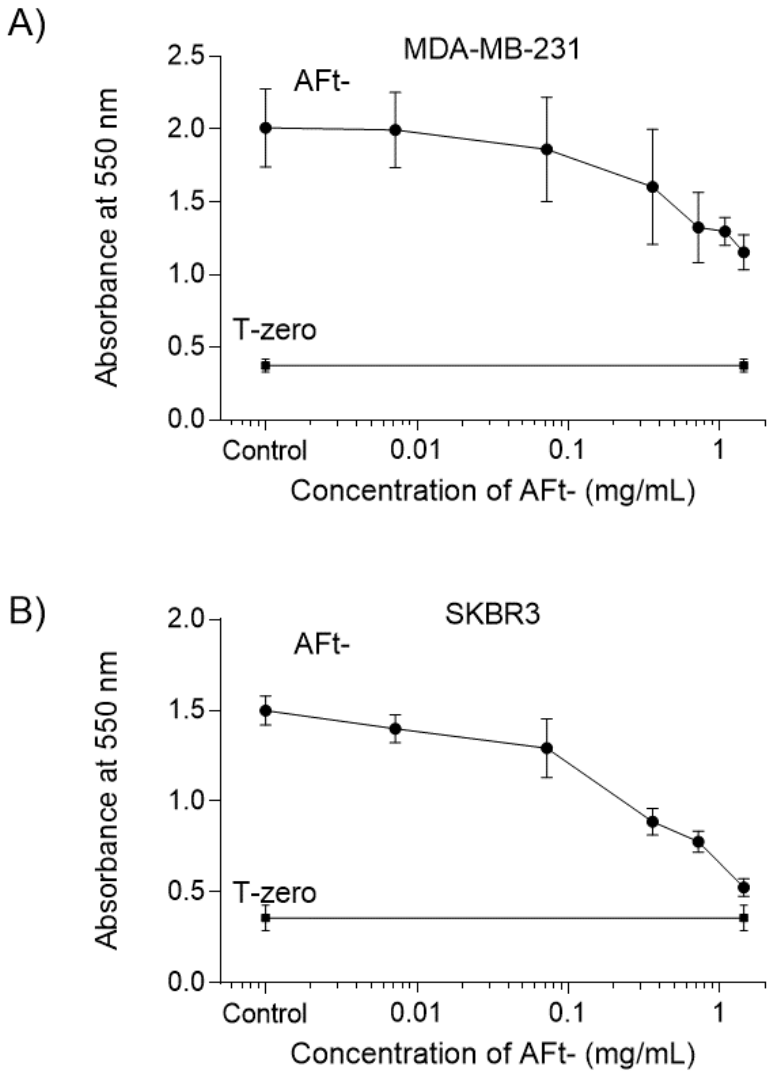


Figure 6.1. Growth inhibitory effect of AFt- on A) MDA-MB-231 and B) SKBR3 cell line after 72 h exposure. Error bars represent the standard deviation over 6 repeats for each point.

The same AFt- dilutions were examined for their effect on the SKBR3 cell line. The MTT assay results presented in Figure 6.1.B show GI_{50} ~ 0.3 mg/mL on these cells. These results should be provide a guide rage of concentrations were AFt- is non-toxic and could be used for further studies.

2. Affibody

The effect of the affibody without cysteine was examined on both breast cancer cell lines. It was expected that the affibody would not exhibit any toxicity in the cells.

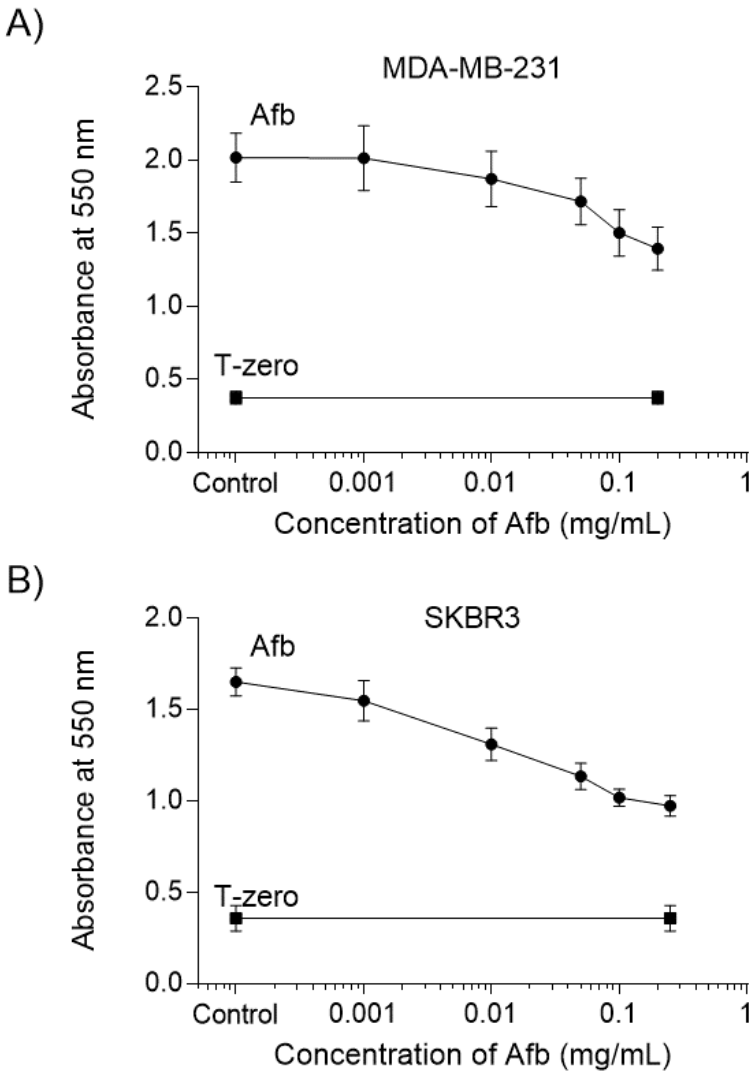


Figure 6.2 Growth inhibitory effect of Afb on A) MDA-MB-231 and B) SKBR3 cell line after 72 h exposure. Error bars represent the standard deviation over 6 repeats for each point.

The viability of the MDA-MB-231 cells after the treatment with affibody showed a slight effect at concentrations > 0.1 mg/mL, as seen in Figure 6.2.A. These results are in agreement with previous results obtained by Dr Lei Zhang (unpublished) [167]

The effect of the Afb on the viability of the SKBR3 cells, Figure 6.2.B, was examined and it showed there is only a slight effect on the growth of the cells with a non-toxic effect. These results indicate the range of Afb concentration suitable for use to target the HER2 receptors.

3. Afb-AFt- of 4 Afb copies

The cell viability after the treatment with affibody fused to the human apoferritin N terminus (Afb-AFt-) protein was also examined. The protein used in this study contains an average of four affibody copies on the surface of the protein cage. The affibody has a strong affinity to the HER2 receptors[195] and it is expected that the Afb-AFt- with four Afb copies can be used as a non-toxic targeted protein to HER2 receptors. A series of Afb-AFt- dilutions were prepared at 0.0077, 0.077, 0.385, 0.77 and 1.54 mg/mL concentrations and used in MTT assays.

The viability of the MDA-MB-231 cells following 72 h of exposure to Afb-AFt- is shown in Figure 6.3.A. The cells retained viability up to ~ 1.4 mg/mL. These results indicate within the studied range of concentrations, Afb-AFt- with 4 Afb copies, does not induce any toxic effects, and the cell viability is not altered.

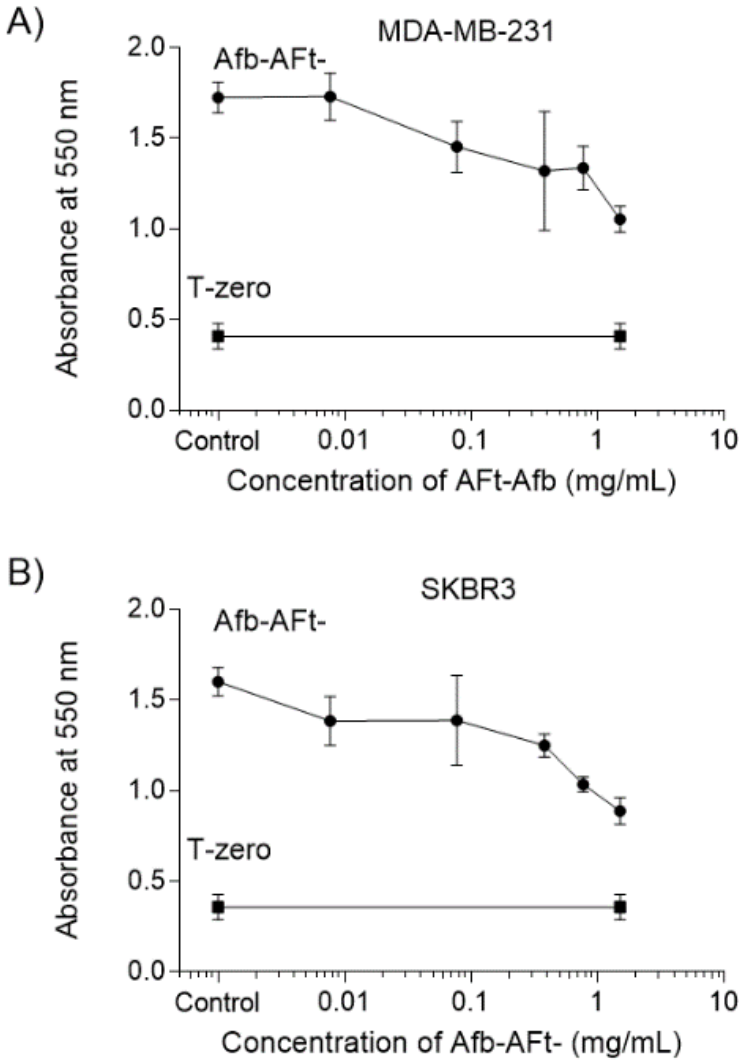


Figure 6.3. Growth inhibitory effect of Afb-AFt- on A) MDA-MB-231 and B) SKBR3 cell line after 72 h exposure. Error bars represent the standard deviation over 6 repeats for each point.

MTT results for SKBR3 cells are presented in Figure 6.3.B, with GI_{50} > 1.04 mg/mL. There is a small decrease in cell viability after exposure with 0.77 mg/mL of Afb-AFt-. However, the protein did not exhibit cytotoxic effect on the cells.

These results can be used as a guide for non-toxic concentrations for treatment after encapsulating the QDs.

6.3. MTT assay of protein encapsulated PbS QDs

TGA/L-CysOMe PbS QDs and GSH PbS QDs were encapsulated in AFt- and Afb-AFt- as described in Chapter 5 and were used for *in vitro* studies to examine their effect on breast cancer cell viability.

6.3.1. AFt- encapsulated TGA/L-CysOMe PbS QDs

TGA/L-CysOME PbS QDs of Pb:TGA:L-CysOMe:S 1:1.5:1:0.3 were encapsulated into AFt- cages by the pH reassembly method. The encapsulated PbS QDs cytotoxicity effect was measured on both breast cancer cell lines. A series of solutions with concentrations from 0.001 to 0.2 mg/mL of PbS QDs with the same concentration of PbS QDs in the encapsulation solution were prepared. In addition, a series of dilutions of AFt- with concentrations equal to the concentrations of the protein in the encapsulated solutions were prepared to explore the effect of the protein capsule on cytotoxicity of the QDs (Table 2.10).

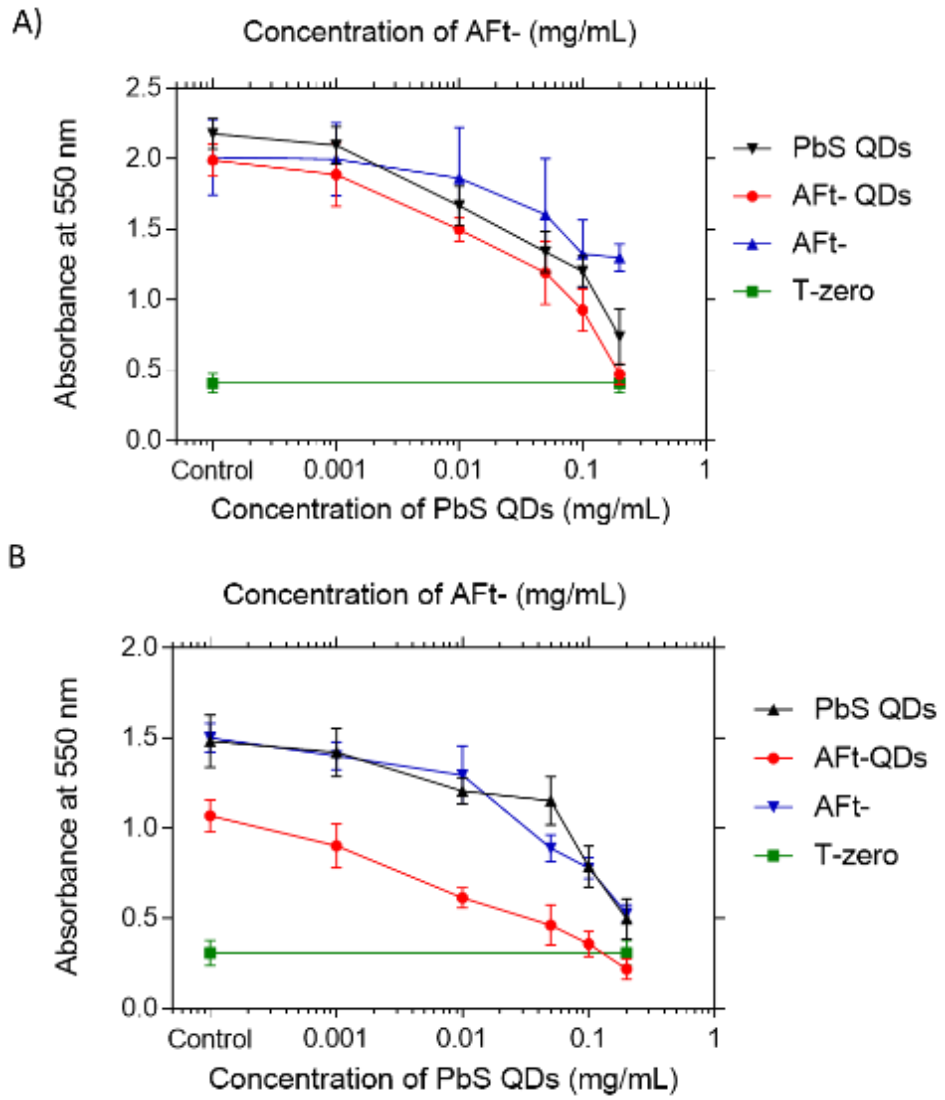


Figure 6.4.Growth inhibitory effect of TGA/L-CysOMe PbS QDs, AFt-QDs and AFt- on A) MDA-MB-231 and B) SKBR3 cell line after 72 h exposure. The concentration of the AFt-QDs is corresponding to the QDs, and the concentration of AFt- equall to the AFt- in the AFt-QDs. Error bars represent the standard deviation over 6 repeats for each point.

The graph in Figure 6.4.A shows the effect of the PbS QDs on the viability of the MDA-MB-231 cells. The estimated GI_{50} of the PbS QDs = 0.07 mg/mL, and the AFt-PbS QDs showed a comparable value of GI_{50} = 0.05 mg/mL. Hence, the encapsulation does not affect the

cytotoxicity of the PbS QDs. In addition, exposure to the AFt- with this concentration did not induce any cytotoxic effects in the cells, unlike exposure to the PbS QDs solutions. Therefore, we conclude that the effect of the AFt-PbS QDs is due to the toxicity associated with PbS QDs. We attribute the observed toxicity of the QDs to release of Pb^{2+}, which were reported to induce information of reactive oxygen species (ROS) leading to cell death.[196,48] The presence of ionic channels in the AFt- capsule would allow the release of Pb^{2+} from encapsulated QDs, explaining comparable GI_{50} values observed in our work.

The results shown in Figure 6.4.B exhibit the effect of the treatments on the SKBR3 viability and they show a very strong effect of AFt-PbS QDS with GI_{50} = 0.007 mg/mL, which is more effective than the QDs (GI_{50} = 0.09 mg/mL) which is probably due to the high affinity of the AFt- to the transferrin receptors that are overexpressed on the cell membrane.

6.3.2. Afb-AFt- encapsulated TGA/L-CysOMe PbS QDs

The growth inhibitory effects of the Afb-AFt- PbS QDs on MDA-MB-231 and SKBR3 were examined. A series of solutions of PbS QDs with concentrations between 0.001 and 0.2 mg/mL were prepared. Also, solutions of Afb-AFt- PbS QDs with the same PbS QDs concentrations were prepared and were compared to the equivalent concentrations of Afb-AFt- as shown in Table 2.10.

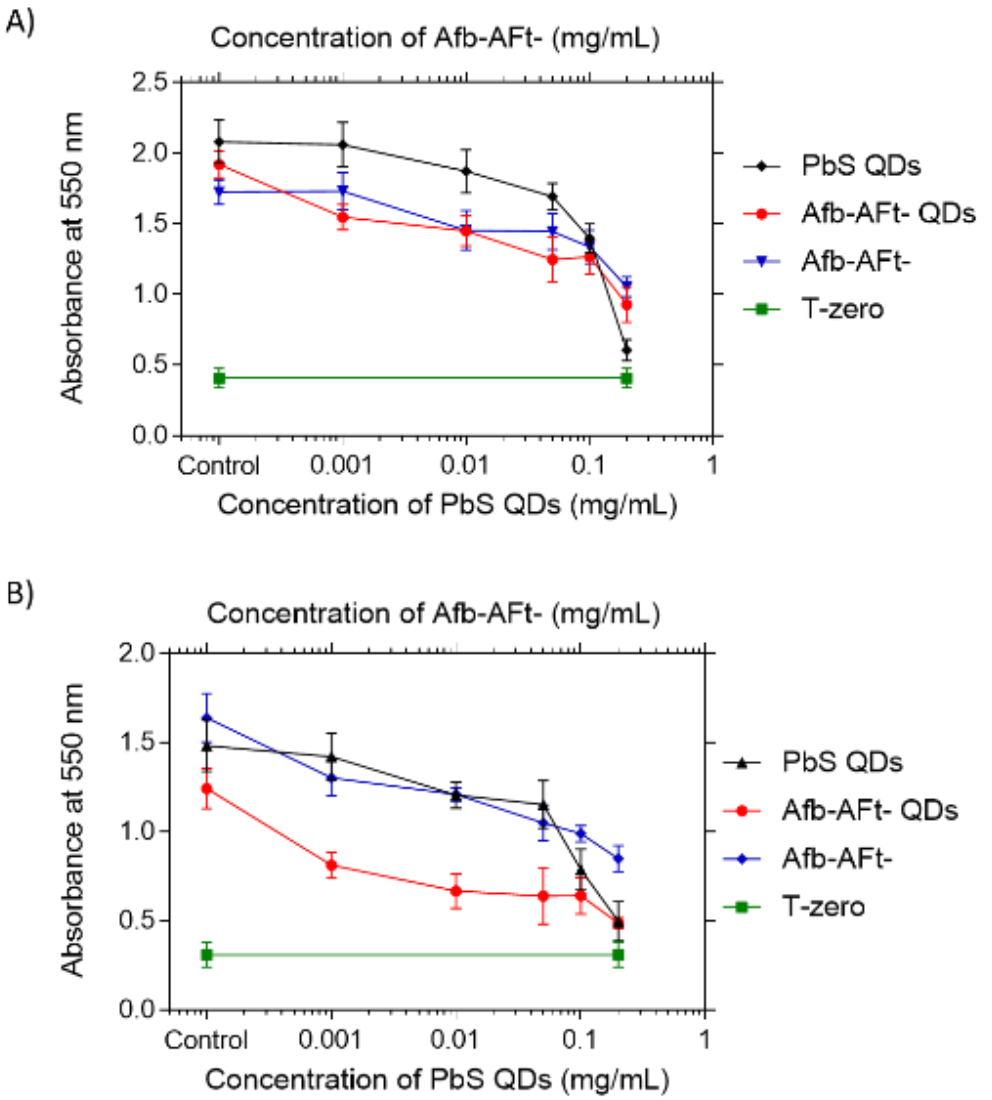


Figure 6.5. Growth inhibitory effect of TGA/L-CysOMe PbS QDs, Afb-AFt-QDs and Afb-AFt- on A) MDA-MB-231 and B) cell line after 72 h exposure. The concentration of the AFt-QDs is corresponding to the QDs, and the concentration of AFt- equall to the AFt- in the AFt-QDs. Error bars represent the standard deviation over 6 repeats for each point.

The graph in Figure 6.5.A shows the viability of the MDA-MB-231 cells after the treatment with Afb-AFt- PbS QDs. A lesser effect was observed compared to QDs alone: the GI_{50} of the PbS QDs was 0.1 mg/mL while for the Afb-AFt- PbS QDs it was 0.18 mg/mL. The Afb-

AFt- PbS QDs did not exhibit a toxic effect like the QDs alone; in addition, the protein itself had a non-toxic effect on cell viability. The increasing of the GI_{50} values of the TGA/L-CysOMe PbS QDs encapsulated by Afb-AFt- is due to the low expression of HER2 receptors which reduce the QDs uptake by the cell, i.e., greater numbers of QDs result in higher toxicity. The lower uptake of the Afb-AFt-QDs by the MDA-MB-231 cells is due to the lack of HER2 receptors availability, and therefore, a greater GI_{50} was observed for the Afb-AFt-QDs compared to the QDs alone.

The viability of SKBR3 was decreased by PbS QDs and Afb-AFt- PbS QDs, Figure 6.5.B. The GI_{50} of the PbS QDs was 0.09 mg/mL and for the Afb-AFt- PbS QDs it was 0.01 mg/mL. The observed GI_{50} of PbS QDs was ~ 9 times greater than the Afb-AFt-QDs, which gives an indication that SKBR3 cells were more able to uptake the encapsulated QDs than the non-encapsulated. This result supports our hypothesis of HER2 recognition of the Afb-AFt- and hence Afb-AFt- induces the increase in QDs uptake after encapsulation. Confocal NIR imaging is needed to confirm greater uptake (NIR detection is not available).

The MTT results are in agreement with a previous study reporting the growth inhibition of the targeted cancer cell.[193] These results suggest that Afb-AFt- enables selective delivery of PbS QDs to HER2 overexpressing SKBR3 cells.

6.3.3. AFt- encapsulated GSH PbS QDs

GSH PbS QDs of Pb:GSH:S molar ratio 1:2:0.3 were encapsulated by AFt- cages by the pH reassembly method. The growth inhibitory factor was measured after 72 hours of treatment. A series of dilutions with concentrations of 0.001 to 0.2 mg/mL of PbS QDs and AFt-PbS QDs with concentrations corresponding to the PbS QDs were prepared. Also, AFt- solutions with concentrations equal to the protein concentrations in the encapsulated solutions were prepared.

The graph in Figure 6.6.A shows the viability of the MDA-MB-231 cell line after the treatment with AFt-PbS QDs and GSH PbS QDs. The AFt-QDs showed a larger effect on the cell viability than the PbS QDs. The GI_{50} of the AFt- PbS QDs was 0.07 mg/mL and that of the PbS QDs was 0.15 mg/mL. Lowering the GI_{50} value of the encapsulated QDs was probably due to the affinity of the AFt- to the overexpressing transferrin receptors on the cancer cell membrane and increasing the number of QDs inside the cells. The AFt- exhibited a slight effect on the cell viability, which can be ignored if compared with the effect of the encapsulated QDs.

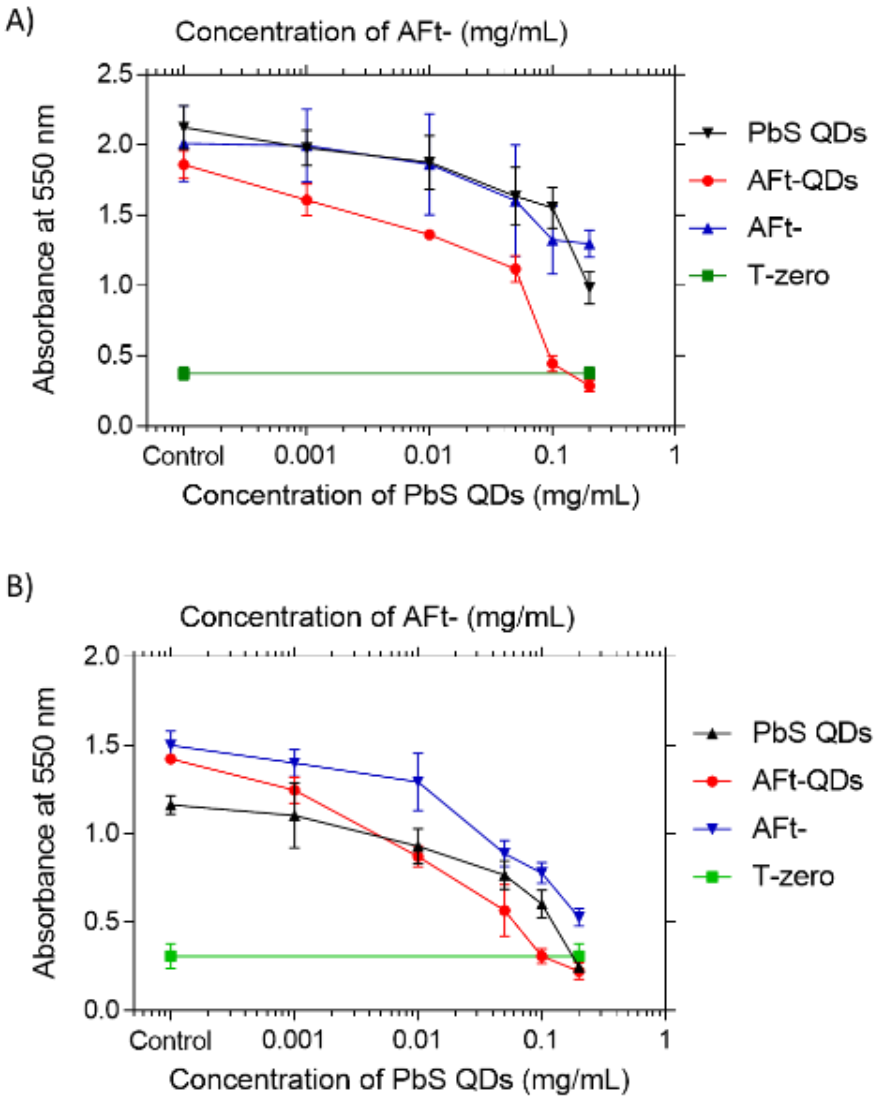


Figure 6.6. Growth inhibitory effect of GSH PbS QDs, AFt-QDs and AFt- on A) MDA-MB-231 and B) SKBR3 cell line after 72 h exposure. The concentration of the AFt-QDs corresponds to the QDs, and the concentration of AFt- is equal to the AFt- in the AFt-QDs. Error bars represent the standard deviation over 6 repeats for each point.

The results in Figure 6.6.B show growth inhibition of SKBR3 cells after the treatments with QDs and AFt-PbS QDs. The GI_{50} values calculated for the QDs and AFt-QDs were 0.1 and 0.01, respectively. SKBR3

exhibited higher toxicity when exposed to AFt-QDs, which indicates a higher uptake of QDs encapsulated than non-encapsulated.

6.3.4. Afb-AFt- encapsulated GSH PbS QDs

GSH PbS QDs were encapsulated by Afb-AFt- with 4 copies of Afb on the surface to target HER2 receptors on cancer cells. The graph in Figure 6.7.A shows the viability of MDA-MB-231 cancer cells after 72 hours of exposure with different concentrations of GSH PbS QDs and Afb-AFt- PbS QDs. The GI_{50} of the PbS QDs was 0.15 mg/mL while for the Afb-AFt- PbS QDs it was 0.13 mg/mL. The reduction of the GI_{50} indicates the higher effect on cell viability. The low effect of the encapsulated QDs is due to encapsulation by Afb-AFt-, which has a low uptake by the MDA-MB-231 cancer cells. The treatment of the cells with the Afb-AFt- exhibited a slight effect on the growth at concentrations higher than 1 mg/mL. This effect is negligible.

On the other hand, Figure 6.7.B, presents the viability of the SKBR3 cells after 72 hours of treatment. The GSH PbS QDs and Afb-AFt- PbS QDs exhibited a greater effect on the cells, the GI_{50} of the PbS QDs was 0.1 mg/mL and for the Afb-AFt- PbS QDs was 0.05 mg/mL. The reduction in the GI_{50} was due to the affinity of the Afb-AFt- to HER2 receptors that increased the QDs uptake by the cells. The effect of the Afb-AFt- can be neglected compared to that of Afb-AFt-QDs (GSH).

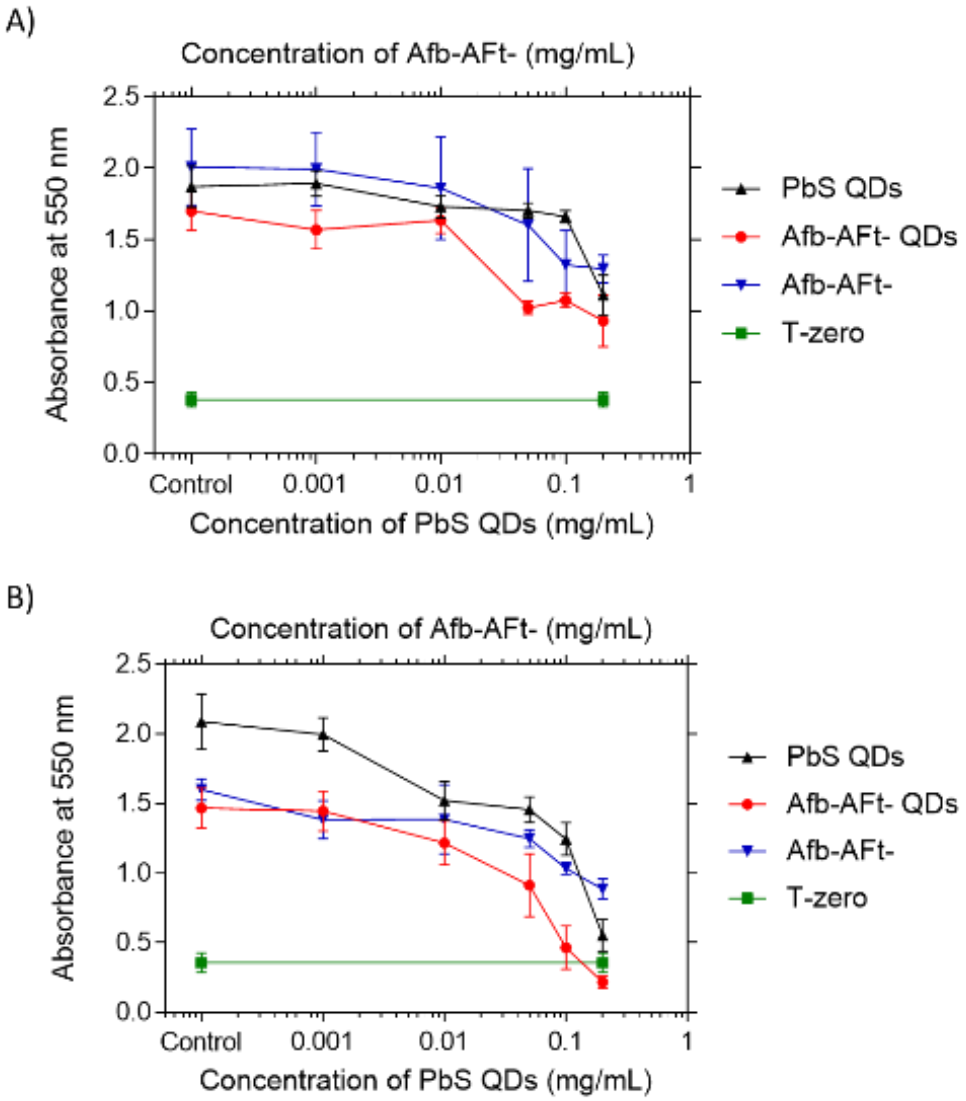


Figure 6.7. Growth inhibitory effect of GSH PbS QDs, Afb-AFt-QDs and Afb-AFt- on A) MDA-MB-231 and B) SKBR3 cell line after 72 h exposure. The concentration of the AFt-QDs corresponds to the QDs, and the concentration of AFt- is equal to the AFt- in the AFt-QDs. Error bars represent the standard deviation over 6 repeats for each point.

These results suggested that the encapsulation of GSH PbS QDs into Afb-AFt- results in high selectivity to SKBR3 cells, which overexpress HER2 receptors.

6.3.5. The effect of the protein encapsulation on the cytotoxicity of the QDs

1. TGA/L-CysOMe PbS QDs

The selectivity of the Afb-AFt- to HER2 receptors and the effect of the encapsulated QDs on the growth of the MDA-MB-231 and SKBR3 breast cancer cells was examined. The MDA-MB-231 and SKBR3 cells were used as a negative and positive control, respectively.

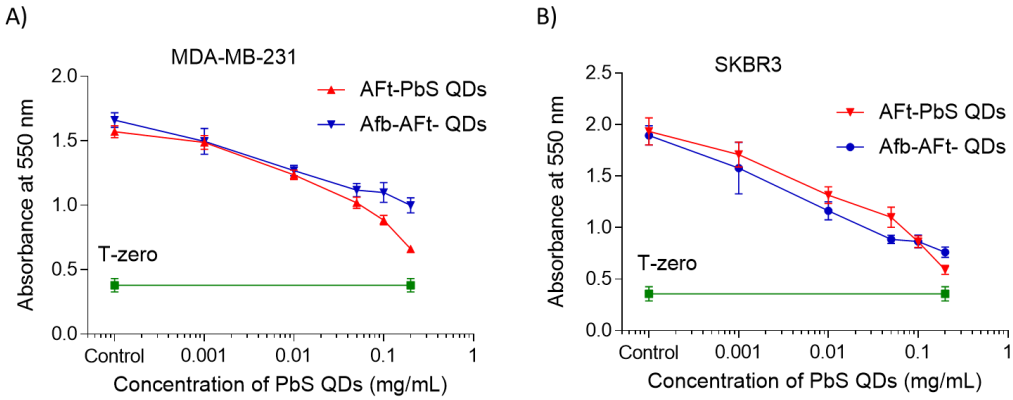


Figure 6.8. Growth inhibitory effect of AFt- PbS QDs and Afb-AFt- PbS QDs (TGA/L-CysOMe) on A) MDA-MB-231 and B) SKBR3. The concentration was applied relative to the concentration of the PbS QDs and the cells were exposed for 72 hours. Error bars represent the standard deviation over 6 repeats for each point.

The results in Figure 6.8.A show the effect of the AFt- PbS QDs and Afb-AFt- PbS QDs (TGA/L-CysOMe) on the MDA-MB-231 cell line. These results indicate the effect of the encapsulated PbS QDs in the AFt- on the cell lines is more effective than the Afb-AFt- PbS QDs. This difference is probably due to the high uptake of the AFt- QDs

through the TfR1 receptors and thus more QDs accumulating inside the cells and reducing the GI_{50} values as seen in Table 6.1.

Table 6.1. GI50 values of TGA/L-CysOMe PbS QDs encapsulated by AFt- and Afb-AFt- on MDA-MB-231 and SKBR3 breast cancer cells.

	GI_{50} values (mg/mL)	
	MDA-MB-231	SKBR3
AFt-QDs	0.08	0.16
Afb-AFt-QDs	0.02	0.01

The viability of the SKBR3 cells presented in Figure 6.8.B shows the toxicity effect of the PbS QDs encapsulated by AFt- and Afb-AFt-. The GI_{50} values indicate a higher toxicity of the Afb-AFt- QDs than the AFt- QDs due to the higher uptake of the Afb-AFt- by the SKBR3 cells through their affinity to the HER2 receptors, Table 6.1.

These results proved the selectivity of the AFt- QDs and Afb-AFt- QDs towards specific receptors, TfR1 and HER2, respectively, which are overexpressed on MDA-MB-231 and SKBR3, respectively.

2. GSH PbS QDs

The effect of the GSH PbS QDs on cell growth was examined with a targeted protein, Afb-AFt-, and a carrier protein, AFt-, on the negative and positive breast cancer cells, MDA-MB-231 and SKBR3, respectively.

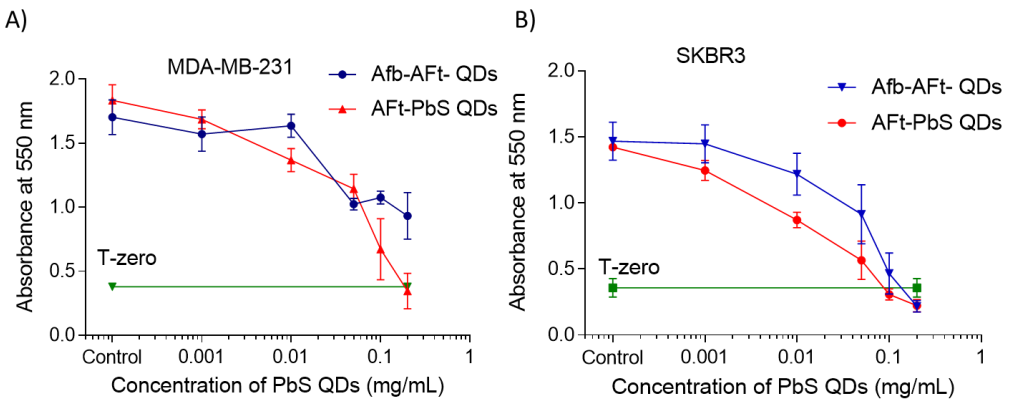


Figure 6.9. Growth inhibitory effect of AFt- PbS QDs and Afb-AFt- PbS QDs (GSH) on A) MDA-MB-231 and B) SKBR3. The concentration was applied relative to the concentration of the PbS QDs and the cells were exposed for 72 hours. Error bars represent the standard deviation over 6 repeats for each point.

From the graphs in Figure 6.9.A it can be seen that the cell viability is altered following exposure to the AFt-QDs, with GI_{50} 0.08 mg/mL, which is lower than for the Afb-AFt-QDs (GI_{50} 0.1 mg/mL). This difference is due to the higher uptake of QDs by the cells through the overexpression of TfR1 and HER2 receptors (Table 6.2).

Table 6.2. GI50 values of GSH PbS QDs encapsulated by AFt- and Afb-AFt- on MDA-MB-231and SKBR3 breast cancer cells.

	GI_{50} values (mg/mL)	
	MDA-MB-231	SKBR3
AFt-QDs	0.08	0.1
Afb-AFt-QDs	0.01	0.05

However, SKBR3 cells exhibited a high toxic effect by both encapsulation solutions, Figure 6.9. (B) and Table 6.2, is due to the overexpression of the HER2 as well as the transferrin receptors, which can increase the QDs uptake by the cells and cause cell toxicity. Also, despite targeting through the existence of the Afb copies on the AFt- surface may lead to smaller and / or enclose channels hence a smaller effect of Pb on the ROS formation.

6.4. Conclusions

The cytotoxicity of TGA/L-CysOMe PbS QDs and GSH PbS QDs were examined in both MDA-MB-231 an SKBR3 breast cancer cells, evaluating the dose effect of the treatments. Also, the effect of the carrier proteins (AFt- and Afb-AFt-) were examined to guide the use of the carrier proteins and their concentration range of usage.

The QDs of TGA/L-CysOMe capping ligands showed a lower GI_{50} than the GSH PbS QDs on both cell lines. This is probably due to the function of the GSH of detoxifying the living tissues from the effect of the oxidative stress. Also, the carrier proteins showed non-toxic effect in the MDA-MB-231 and SKBR3 cell lines with concentration up to 0.3 mg/mL. The Afb-AFt- showed no toxicity in both cell lines with concentration > 1.0 mg/mL.

The MTT assay studies of the PbS QDs encapsulated by AFt- revealed higher levels of toxicity in the cells than the QDs alone because of the affinity of the AFt- to the TfR1 overexpressed on the cancer cells and increasing the number of the QDs inside the cells. Since the AFt-

alone have no toxicity on the cells we can say the toxic effect of the encapsulated QDs are results from the PbS QDs.

The selectivity of the Afb to target the HER2 receptors was confirmed by determining the GI_{50} values of the encapsulated QDs into Afb-AFt- of 4 Afb copies. TGA/L-CysOMe and GSH PbS QDs encapsulated by Afb-AFt- exhibited a lower GI_{50} than the QDs alone in the HER2 overexpressing in the SKBR3 cells (positive control of HER2 receptors). In addition, higher values of GI_{50} were observed in MDA-MB-231 (negative control of HER2 receptors) than the QDs encapsulated by AFt-. Furthermore, the small effects of the Afb-AFt- on both cell lines can be negligible if compared with the effects of the encapsulated PbS QDs. These selectivity results are promising for more *in vitro* and *in vivo* studies.

7. Conclusions and future work

Recently, QDs have been shown to play significant roles in bioimaging and anticancer studies. QDs used in biological applications face several challenges such as fluorescence wavelength region, biocompatibility and delivery systems. Surface modification of QDs using different ligands, peptides and encapsulations have been applied to address these challenges.

In this work, PbS QDs capped with different capping ligands containing thiol groups were synthesised in physiologically relevant solvents. In addition, apoferritin and affibody-apoferritin cages were used to encapsulate the synthesised QDs to address the biocompatibility issues. The cytotoxicity of the encapsulated QDs were examined using the MTT assay on breast cancer cells.

PbS QDs were successfully passivated with different thiol ligands (L-Cys, L-CysOMe, TGA/L-CysOMe and GSH) and produced in aqueous solutions. The PbS QDs had optical emission wavelength range of 880 nm to 920 nm. The synthesis methods were adjusted to produce the QDs with desirable size, surface charge and optical properties. In order to achieve these properties, the composition materials molar ratio, temperature and the pH were optimised. The synthesised PbS QDs produced with highest stability and lowest PL emission were selected for encapsulation in AFt- cages.

Protein cages of AFt- and Afb-AFt- of 4 Afb copies were successfully expressed by *E. coli* and purified by the Ni-IMAC technique. High

purity and concentrations of the proteins were obtained. The Afb-AFt- purification was performed by using 4 M of urea instead of 8 M to reduce the protein degradation and increase the probability to achieve better purity of the protein.

For the PbS QDs encapsulation, AFt- and Afb-AFt- were used. pH reassembly, nanoreactor and urea reassembly routes were used for the encapsulation.

L-Cys PbS PbS QDs were not encapsulated successfully by the AFt- probably due to the high negative charge of the L-CysPbS QDs. Also, the L-CysOMe PbS QDs were not encapsulated due to their low stability in aqueous solution. However, TGA/L-CysOMe PbS QDs were successfully encapsulated by AFt- following all three encapsulation methods, and the GSH PbS QDs were successfully encapsulated by AFt- using pH reassembly and urea reassembly methods. TGA/L-CysOMe PbS QDs and GSH PbS QDs were successfully encapsulated by Afb-AFt-, and pH reassembly methods were used for the encapsulation. The surface charge of the QDs played a significant role in the production of efficient encapsulation solution.

For the cytotoxicity studies, MDA-MB-231 and SKBR3 breast cancer cells were treated with different concentrations of PbS QDs. AFt- QDs of both TGA/L-CysOMe PbS QDs and GSH PbS QDs showed toxic effects on both cancer cells through their uptake by TfR1 receptors.

The selectivity of the Afb towards HER2 receptors overexpressed on the SKBR3 cells was examined. It was found that Afb-AFt-QDs of

TGA/L-CysOMe PbS QDs and GSH PbS QDs had a stronger effect on the SKBR3 cells than the MDA-MB-231 cells. In addition, the Afb-AFt-QDs had a less effect on the MDA-MB-231 than the AFt-QDs.

Future *in vitro* studies are recommended for further understanding of the function of the PbS QDs inside the cancer cells. The TEM imaging of the cells after the treatment with the PbS QDs and encapsulated QDs is necessary to evaluate their localisation inside the cancer cells. Furthermore, the investigation of the QDs and encapsulated QDs uptake by the cancerous cells should be analysed by using inductively coupled plasma mass spectrometry (ICP-MS). Also, flow cytometry assay is required to determine at which stage of the cell cycle the encapsulated QDs targets the cells. Understanding the mechanism of cell death by the encapsulated PbS QDs can be investigated by Annexin V assays. Also, applying the synthesised QDs for *in vivo* studies and determine the effect of the QDs on the living cells and imaging the cells, and studying the distribution of the QDs inside the living tissue.

8. References

1. Saldanha, P. L., Lesnyak, V. & Manna, L. Large Scale Syntheses of Colloidal Nanomaterials. *Nano Today* 2017, **12,** 46–63.

2. Das, M., Shim, K. H., An, S. S. A. & Yi, D. K. Review on Gold Nanoparticles and Their Applications. *Toxicol. Environ. Health Sci.* 2011, **3,** 193–205.

3. Lin, J., Chen, X. & Huang, P. Graphene-Based Nanomaterials for Bioimaging. *Adv. Drug Deliv. Rev.* 2016, **105,** 242–254.

4. Palui, G., Aldeek, F., Wang, W. & Mattoussi, H. Strategies for Interfacing Inorganic Nanocrystals with Biological Systems Based on Polymer-Coating. *Chem. Soc. Rev.* 2015, **44,** 193–227.

5. Lai, L.-H., Protesescu, L., Kovalenko, M. V. & Loi, M. A. Sensitized Solar Cells with Colloidal PbS–CdS Core–shell Quantum Dots. *Phys. Chem. Chem. Phys.* 2014, **16,** 736–742.

6. Fang, M., Peng, C.-W., Pang, D.-W. & Li, Y. Quantum Dots for Cancer Research: Current Status, Remaining Issues, and Future Perspectives. *Cancer Biol. Med.* 2012, **9,** 151–163.

7. Reineck, P. & Gibson, B. C. Near-Infrared Fluorescent Nanomaterials for Bioimaging and Sensing. *Adv. Opt. Mater.* 2017, **5,** 1600446–1600472.

8. Giansante, C. *et al.* 'Darker-than-Black' PbS Quantum Dots: Enhancing Optical Absorption of Colloidal Semiconductor Nanocrystals via Short Conjugated Ligands. *J. Am. Chem. Soc.* 2015, **137,** 1875–1886.

9. Asano, H. & Omata, T. Design of Cadmium-Free Colloidal II-VI Semiconductor Quantum Dots Exhibiting RGB Emission. *AIP Adv.* 2017, **7,** 045309–045315.

10. Grigel, V., Dupont, D., De Nolf, K., Hens, Z. & Tessier, M. D.

InAs Colloidal Quantum Dots Synthesis via Aminopnictogen Precursor Chemistry. *J. Am. Chem. Soc.* 2016, **138,** 13485–13488.

11. Jang, Y. *et al.* Interface Control of Electronic and Optical Properties in IV–VI and II–VI Core/Shell Colloidal Quantum Dots: A Review. *Chem. Commun.* 2017, **53,** 1002–1024.

12. Medintz, I. L., Uyeda, H. T., Goldman, E. R. & Mattoussi, H. Quantum Dot Bioconjugates for Imaging, Labelling and Sensing. *Nat. Mater.* 2005, **4,** 435–446.

13. Pellegrino, T. *et al.* On the Development of Colloidal Nanoparticles Towards Multifunctional Structures and Their Possible Use for Biological Applications. *Small* 2005, **1,** 48–63.

14. Aswathy, R. G., Yoshida, Y., Maekawa, T. & Kumar, D. S. Near-Infrared Quantum Dots for Deep Tissue Imaging. *Anal. Bioanal. Chem.* 2010, **397,** 1417–1435.

15. Zhao, M. X. & Zeng, E. Z. Application of Functional Quantum Dot Nanoparticles as Fluorescence Probes in Cell Labeling and Tumor Diagnostic Imaging. *Nanoscale Res. Lett.* 2015, **10,** 1–9.

16. Zhao, P. *et al.* Near Infrared Quantum Dots in Biomedical Applications: Current Status and Future Perspective. *WIREs. Nanomed. Nanobiotechnol.* 2018, **10,** 1–16.

17. Levina, L. *et al.* Efficient Infrared-Emitting PbS Quantum Dots Grown on DNA and Stable in Aqueous Solution and Blood Plasma. *Adv. Mater.* 2005, **17,** 1854–1857.

18. Escobedo, J. O., Rusin, O., Lim, S. & Strongin, R. M. NIR Dyes for Bioimaging Applications. *Curr. Opin. Chem. Biol.* 2010, **14,** 64–74.

19. Hyun, B. R., Chen, H., Rey, D. A., Wise, F. W. & Batt, C. A. Near-Infrared Fluorescence Imaging with Water-Soluble Lead Salt Quantum Dots. *J. Phys. Chem. B* 2007, **111,** 5726–5730.

20. Resch-Genger, U., Grabolle, M., Cavaliere-Jaricot, S., Nitschke, R. & Nann, T. Quantum Dots Versus Organic Dyes as Fluorescent Labels. *Nat. Methods* 2008, **5,** 763–775.

21. Chung, H., Choi, H., Kim, D., Jeong, S. & Kim, J. Size Dependence of Excitation Energy Related Surface Trapping Dynamics in PbS Quantum Dots. *J. Phys. Chem. C* 2015, **119,** 7517–7524.

22. Kang, Y. *et al.* Quantum Dots for Wide Color Gamut Displays from Photoluminescence to Electroluminescence. *Nanoscale Res. Lett.* 2017, **12,** 1–8.

23. Ren, F. *et al.* Development and Investigation of Ultrastable PbS/CdS/ZnS Quantum Dots for Near-Infrared Tumor Imaging. *Part. Part. Syst. Charact.* 2016, **34,** 1–11.

24. Qin, H., Meng, R., Wang, N. & Peng, X. Photoluminescence Intermittency and Photo-Bleaching of Single Colloidal Quantum Dot. *Adv. Mater.* 2017, **29,** 1606923–1606938.

25. Vicente, N. B., Diaz Zamboni, J. E., Adur, J. F., Paravani, E. V. & Casco, V. H. Photobleaching Correction in Fluorescence Microscopy Images. *J. Phys. Conf. Ser.* 2007, **90,** 012068–012075.

26. Guo, C. X. *et al.* A New Class of Fluorescent-Dots: Long Luminescent Lifetime Bio-Dots Self-Assembled from DNA at Low Temperatures. *Sci. Rep.* 2013, **3,** 1–6.

27. Litvin, A. P. *et al.* Size-Dependent Room-Temperature Luminescence Decay from PbS Quantum Dots. *Proc. SPIE - Int. Soc. Opt. Photonics.* 2012, **8564,** 85641–85647.

28. Liu, L., Miao, Q. & Liang, G. Quantum Dots as Multifunctional Materials for Tumor Imaging and Therapy. *Materials.* 2013, **6,** 483–499.

29. Ortiz, S. N. C., Ospino, E. M. & Cabanzo, R. Spectroscopy Characterization and Quantum Yield Determination of Quantum Dots.

J. Phys. Conf. Ser. 2016, **687,** 12097–12100.

30. Shestha, A. *et al.* Versatile PbS Quantum Dot Ligand Exchange Systems in the Presence of Pb-Thiolates. *Small* 2017, **13,** 1–6.

31. Wise, F. W. Lead Salt Quantum Dots: The Limit of Strong Quantum Confinement. *Acc. Chem. Res.* 2000, **33,** 773–780.

32. Arya, H. *et al.* Quantum Dots in Bio-Imaging: Revolution by the Small. *Biochem. Biophys. Res. Commun.* 2005, **329,** 1173–1177.

33. Andersen, K. E., Fong, C. Y. & Pickett, W. E. Quantum Confinement in CdSe Nanocrystallites. *J. Non. Cryst. Solids* 2002, **302,** 1105–1110.

34. Moreels, I. *et al.* Size-Dependent Optical Properties of Colloidal PbS Quantum Dots. *ACS Nano* 2009, **3,** 3023–3030.

35. Wang, Y., Suna, A., Mahler, W. & Kasowski, R. PbS in Polymers. From Molecules to Bulk Solids. *J. Chem. Phys.* 1987, **87,** 7315–7322.

36. Zhang, Y. & Clapp, A. Overview of Stabilizing Ligands for Biocompatible Quantum Dot Nanocrystals. *Sensors* 2011, **11,** 11036–11055.

37. Ag, D. *et al.* Biofunctional Quantum Dots as Fluorescence Probe for Cell-Specific Targeting. *Colloids Surfaces B Biointerfaces* 2014, **114,** 96–103.

38. Liu, S., Wang, Y., Pan, H., Yang, K. & Zhou, L. Synthesis of High-Quality CdSe Quantum Dots in Aqueous Solution. *Micro Nano Lett.* 2012, **7,** 889–891.

39. Martinez-Mancera, F. D. & Hernandez-Lopez, J. L. Physical Characterization and Photoluminescence Properties of Thioglycolic Acid-Stabilized Lead Sulfide Nanocrystals. *Mater. Chem. Phys.* 2014, **148,** 1045–1054.

40. Reinhart, C. C. & Johansson, E. Colloidally Prepared 3-Mercaptopropionic Acid Capped Lead Sulfide Quantum Dots. *Chem. Mater.* 2015, **27,** 7313–7320.

41. Bunkoed, O. & Kanatharana, P. Mercaptopropionic Acid-Capped CdTe Quantum Dots as Fluorescence Probe for the Determination of Salicylic Acid in Pharmaceutical Products. *Luminescence* 2015, **30,** 1083–1089.

42. Yu, Y., Zhang, K. & Sun, S. Effect of Ligands on the Photoluminescence Properties of Water-Soluble PbS Quantum Dots. *J. Mol. Struct.* 2013, **1031,** 194–200.

43. Sun, Q., Fu, S., Dong, T., Liu, S. & Huang, C. Aqueous Synthesis and Characterization of TGA-Capped CdSe Quantum Dots at Freezing Temperature. *Molecules* 2012, **17,** 8430–8438.

44. Chang, L., He, X., Chen, L. & Zhang, Y. A Novel Fluorescent Turn-on Biosensor Based on QDs@GSH–GO Fluorescence Resonance Energy Transfer for Sensitive Glutathione S-Transferase Sensing and Cellular Imaging. *Nanoscale* 2017, **9,** 3881–3888.

45. Pérez-Donoso, J. M. *et al.* Biomimetic, Mild Chemical Synthesis of Cdte-GSH Quantum Dots with Improved Biocompatibility. *PLoS One* 2012, **7,** 30741–30749.

46. Feng, W. *et al.* A Layer-Nanostructured Assembly of PbS Quantum Dot/Multiwalled Carbon Nanotube for a High-Performance Photoswitch. *Sci. Rep.* 2014, **4,** 1–7.

47. Diaz-Diestra, D., Thapa, B., Beltran-Huarac, J., Weiner, B. R. & Morell, G. L-Cysteine Capped ZnS:Mn Quantum Dots for Room-Temperature Detection of Dopamine with High Sensitivity and Selectivity. *Biosens. Bioelectron.* 2017, **87,** 693–700.

48. Turyanska, L. *et al.* The Biocompatibility of Apoferritin-Encapsulated PbS Quantum Dots. *Small* 2009, **5,** 1738–1741.

49. Zamberlan, F. *et al.* Stable DHLA–PEG Capped PbS Quantum Dots: From Synthesis to Near-Infrared Biomedical Imaging. *J. Mater. Chem. B* 2018, **6,** 550–555.

50. Garcia-Cortes, M. *et al.* Capping of Mn-Doped ZnS Quantum Dots with DHLA for Their Stabilization in Aqueous Media: Determination of the Nanoparticle Number Concentration and Surface Ligand Density. *Langmuir* 2017, **33,** 6333–6341.

51. Gao, F., Liu, Y., Fan, Y. & Zhao, D. Synthesis of N-Acetyl-L-Cysteine-Capped ZnCdSe Quantum Dots via Hydrothermal Method and Their Characterization. *Sci. Technol. Adv. Mater.* 2014, **15,** 1–9.

52. Deng, D. *et al.* Facile Synthesis of High-Quality, Water-Soluble, Near-Infrared-Emitting PbS Quantum Dots. *Eur. J. Inorg. Chem.* 2009, **2009,** 3440–3446.

53. Jin, S., Hu, Y., Gu, Z., Liu, L. & Wu, H.-C. Application of Quantum Dots in Biological Imaging. *J. Nanomater.* 2011, **2011,** 1–13.

54. Andreakou, P. *et al.* Size- and Temperature-Dependent Carrier Dynamics in Oleic Acid Capped PbS Quantum Dots. *J. Phys. Chem. C* 2013, **117,** 1887–1892.

55. Tsoi, K., Dai, Q., Alman, B. & Chan, W. Are Quantum Dots Toxic? Exploring the Discrepancy Between Cell Culture and Animal Studies. *Acc. Chem. Res.* 2013, **46,** 662–671.

56. Shao, L., Gao, Y. & Yan, F. Semiconductor Quantum Dots for Biomedicial Applications. *Sensors* 2011, **11,** 11736–11751.

57. Deng, D. *et al.* Forming Highly Fluorescent Near-Infrared Emitting PbS Quantum Dots in Water Using Glutathione as Surface-Modifying Molecule. *J. Colloid Interface Sci.* 2012, **367,** 234–240.

58. Ren, T. *et al.* A Simple and Versatile Route to Stable Quantum Dot-Dye Hybrids in Nonaqueous and Aqueous Solutions. *J. Am.*

Chem. Soc. 2008, **130,** 17242–17243.

59. Wu, X. *et al.* Immunofluorescent Labeling of Cancer Marker HER2 and Other Cellular Targets with Semiconductor Quantum Dots. *Nat. Biotechnol.* 2003, **21,** 41–46.

60. Bruchez Jr., M., Moronne, M., Gin, P., Wiess, S. & Alivisatos, A. P. Semiconductor Nanocrystals as Fluorescent Biological Labels. *Science.* 1998, **281,** 2013–2016.

61. Hu, R. *et al.* PEGylated Phospholipid Micelle-Encapsulated Near-Infrared PbS Quantum Dots for *in Vitro* and *in Vivo* Bioimaging. *Theranostics* 2012, **2,** 723–733.

62. Yu, W. W. *et al.* Forming Biocompatible and Nonaggregated Nanocrystals in Water Using Amphiphilic Polymers. *J. Am. Chem. Soc.* 2007, **129,** 2871–2879.

63. Gerion, D. *et al.* Sorting Fluorescent Nanocrystals with DNA. *J. Am. Chem. Soc.* 2002, **124,** 7070–7074.

64. Sukhanova, A. *et al.* Biocompatible Fluorescent Nanocrystals for Immunolabeling of Membrane Proteins and Cells. *Anal. Biochem.* 2003, **324,** 60–67.

65. Panchbhai, A. Wilhelm Conrad Röntgen and the Discovery of X-Rays: Revisited after Centennial. *J. Indian Acad. Oral Med. Radiol.* 2015, **27,** 90–95.

66. Quek, C.-H. & Leong, K. W. Near-Infrared Fluorescent Nanoprobes for *in Vivo* Optical Imaging. *Nanomaterials* 2012, **2,** 92–112.

67. Kairdolf, B. A. *et al.* Semiconductor Quantum Dots for Bioimaging and Biodiagnostic Applications. *Annu. Rev. Anal. Chem.* 2013, **6,** 143–162.

68. Smith, A. M., Mancini, M. C. & Nie, S. Second Window for *in Vivo* Imaging. *Nat. Nanotechnol.* 2009, **4,** 710–711.

69. Pham, W., Medarova, Z. & Moore, A. Synthesis and Application of a Water-Soluble Near-Infrared Dye for Cancer Detection Using Optical Imaging. *Bioconjug. Chem.* 2005, **16,** 735–740.

70. Close, D. M., Xu, T., Sayler, G. S. & Ripp, S. *In Vivo* Bioluminescent Imaging (BLI): Noninvasive Visualization and Interrogation of Biological Processes in Living Animals. *Sensors* 2011, **11,** 180–206.

71. Tsukasaki, Y. *et al.* Synthesis and Optical Properties of Emission-Tunable PbS/CdS Core–shell Quantum Dots for *in Vivo* Fluorescence Imaging in the Second Near-Infrared Window. *RSC Adv.* 2014, **4,** 41164–41171.

72. Xing, Y., So, M., Koh, A., Sinclair, R. & Rao, J. Improved QD-BRET Conjugates for Detection and Imaging. *Biochem. Biophys. Res. Commun.* 2008, **372,** 388–394.

73. Chou, K. & Dennis, A. Förster Resonance Energy Transfer between Quantum Dot Donors and Quantum Dot Acceptors. *Sensors* 2015, **15,** 13288–13325.

74. Lingley, Z., Lu, S. & Madhukar, A. A High Quantum Efficiency Preserving Approach to Ligand Exchange on Lead Sulfide Quantum Dots and Interdot Resonant Energy Transfer. *Nano Lett.* 2011, **11,** 2887–2891.

75. Medintz, I. L. & Mattoussi, H. Quantum Dot-Based Resonance Energy Transfer and Its Growing Application in Biology. *Phys. Chem. Chem. Phys.* 2009, **11,** 17–45.

76. Jensen, E. C. Use of Fluorescent Probes: Their Effect on Cell Biology and Limitations. *Anat. Rec. Adv. Integr. Anat. Evol. Biol.* 2012, **295,** 2031–2036.

77. Derfus, A. M., Chan, W. C. W. & Bhatia, S. N. Probing the Cytotoxicity of Semiconductor Quantum Dots. *Nano Lett.* 2004, **4,** 11–18.

78. Lovrić, J., Cho, S. J., Winnik, F. M. & Maysinger, D. Unmodified Cadmium Telluride Quantum Dots Induce Reactive Oxygen Species Formation Leading to Multiple Organelle Damage and Cell Death. *Chem. Biol.* 2005, **12,** 1227–1234.

79. Parak, W. J. *et al.* Cell Motility and Metastatic Potential Studies Based on Quantum Dot Imaging of Phagokinetic Tracks. *Adv. Mater.* 2002, **14,** 882–885.

80. Valizadeh, A. *et al.* Quantum Dots: Synthesis, Bioapplications, and Toxicity. *Nanoscale Res. Lett.* 2012, **7,** 480–493.

81. Dubertret, B. *et al. In Vivo* Imaging of Quantum Dots Encapsulated in Phospholipid Micelles. *Science.* 2002, **298,** 1759–1762.

82. Yong, K. T. *et al.* Nanotoxicity Assessment of Quantum Dots: From Cellular to Primate Studies. *Chem. Soc. Rev.* 2013, **42,** 1236–1250.

83. Ye, L. *et al.* A Pilot Study in Non-Human Primates Shows No Adverse Response to Intravenous Injection of Quantum Dots. *Nat. Nanotechnol.* 2012, **7,** 453–458.

84. Odiba, A. *et al.* Therapeutic Nanomedicine Surmounts the Limitations of Pharmacotherapy. *Open Med.* 2017, **12,** 271–287.

85. Mirza, A. Z. & Siddiqui, F. A. Nanomedicine and Drug Delivery: A Mini Review. *Int. Nano Lett.* 2014, **4,** 94.

86. Abbasi, E. *et al.* Dendrimers: Synthesis, Applications, and Properties. *Nanoscale Res. Lett.* 2014, **9,** 1–10.

87. Namazi, H. *et al.* Encapsulation of Nanoparticles Using Linear-Dendritic Macromolecules. *Colloid Polym. Sci.* 2007, **285,** 1527–1533.

88. Yang, P. Y., Ju, S. P., Chuang, Y. C. & Chen, H. Y. Molecular Dynamics Simulations of PAMAM Dendrimer-Encapsulated Au

Nanoparticles of Different Sizes under Different PH Conditions. *Comput. Mater. Sci.* 2017, **137,** 144–152.

89. Solaro, R., Chiellini, F. & Battisti, A. *Targeted delivery of protein drugs by nanocarriers*. *Materials* (2010). **3,**

90. Hamelers, I. H. & de Kroon, A. I. Nanocapsules: A Novel Formulation Technology for Platinum-Based Anticancer Drugs. *Future Lipidol.* 2007, **2,** 445–453.

91. Mathur, D. *et al.* Quantum Dot Encapsulation Using a Peptide-Modified Tetrahedral DNA Cage. *Chem. Mater.* 2017, **29,** 5762–5766.

92. Li, Y., Liu, Z., Yu, G., Jiang, W. & Mao, C. Self-Assembly of Molecule-like Nanoparticle Clusters Directed by DNA Nanocages. *J. Am. Chem. Soc.* 2015, **137,** 4320–4323.

93. Erben, C. M., Goodman, R. P. & Turberfield, A. J. Single-Molecule Protein Encapsulation in a Rigid DNA Cage. *Angew. Chemie - Int. Ed.* 2006, **45,** 7414–7417.

94. Zhang, W. *et al.* Encapsulation of Inorganic Nanomaterials inside Virus-Based Nanoparticles for Bioimaging. *Nanotheranostics* 2017, **1,** 358–368.

95. Heger, Z., Skalickova, S., Zitka, O., Adam, V. & Kizek, R. Apoferritin Applications in Nanomedicine. *Nanomedicine* 2014, **9,** 2233–2245.

96. Tiwari, G. *et al.* Drug Delivery Systems : An Updated Review. *Int. J. Pharm. Investig.* 2012, **2,** 2–11.

97. Gelperina, S., Kisich, K., Iseman, M. D. & Heifets, L. The Potential Advantages of Nanoparticle Drug Delivery Systems in Chemotherapy of Tuberculosis. *Am. J. Respir. Crit. Care Med.* 2005, **172,** 1487–1490.

98. Din, F. U. *et al.* Effective Use of Nanocarriers as Drug Delivery Systems for the Treatment of Selected Tumors. *Int. J. Nanomedicine*

2017, **12,** 7291–7309.

99. Zangabad, P. S., Karimi, M. & Mehdizadeh, F. Nanocaged Platforms: Modification, Drug Delivery and Nanotoxicity. Opening Synthetic Cages to Release the Tiger. *RSC Nanoscale* 2017, **9,** 1356–1392.

100. Laufberger, V. Contribution to the Technique of Renin Seclusion. *C. R. Seances. Soc. Biol. Fil.* 1937, **126,** 107–109.

101. Zhang, Y. & Orner, B. P. Self-Assembly in the Ferritin Nano-Cage Protein Superfamily. *Int. J. Mol. Sci.* 2011, **12,** 5406–5421.

102. Dixon, S. J. & Stockwell, B. R. The Role of Iron and Reactive Oxygen Species in Cell Death. *Nat. Chem. Biol.* 2014, **10,** 9–17.

103. Thomas, C., Mackey, M. M., Diaz, A. A. & Cox, D. P. Hydroxyl Radical Is Produced via the Fenton Reaction in Submitochondrial Particles under Oxidative Stress: Implications for Diseases Associated with Iron Accumulation. *Redox Rep.* 2009, **14,** 102–108.

104. Linder, M. C. Mobilization of Stored Iron in Mammals: A Review. *Nutrients* 2013, **5,** 4022–4050.

105. Chasteen, N. D. & Harrison, P. M. Mineralization in Ferritin: An Efficient Means of Iron Storage. *J. Struct. Biol.* 1999, **126,** 182–194.

106. Zang, J., Chen, H., Zhao, G., Wang, F. & Ren, F. Ferritin Cage for Encapsulation and Delivery of Bioactive Nutrients: From Structure, Property to Applications. *Crit. Rev. Food Sci. Nutr.* 2017, **57,** 3673–3683.

107. He, D. & Marles-Wright, J. Ferritin Family Proteins and Their Use in Bionanotechnology. *N. Biotechnol.* 2015, **32,** 651–657.

108. Abe, S., Maity, B. & Ueno, T. Design of a Confined Environment Using Protein Cages and Crystals for the Development of Biohybrid Materials. *Chem. Commun.* 2016, **52,** 6496–6512.

109. Uchida, M., Kang, S., Reichhardt, C., Harlen, K. & Douglas, T. The Ferritin Superfamily: Supramolecular Templates for Materials Synthesis. *Biochim. Biophys. Acta - Gen. Subj.* 2010, **1800,** 834–845.

110. Andrews, S. C. *et al.* Structure, Function, and Evolution of Ferritins. *J. Inorg. Biochem.* 1992, **47,** 161–174.

111. Uchida, M. *et al.* Targeting of Cancer Cells with Ferrimagnetic Ferritin Cage Nanoparticles. *J. Am. Chem. Soc.* 2006, **128,** 16626–16633.

112. Levi, S. *et al.* Evidence of H- and L-Chains Have Co-Operative Roles in the Iron-Uptake Mechanism of Human Ferritin. *Biochem. J.* 1992, **288,** 591–596.

113. Li, L. *et al.* Binding and Uptake of H-Ferritin Are Mediated by Human Transferrin Receptor-1. *Proc. Natl. Acad. Sci.* 2010, **107,** 3505–3510.

114. Lane, D. J. R. *et al.* Cellular Iron Uptake, Trafficking and Metabolism: Key Molecules and Mechanisms and Their Roles in Disease. *Biochim. Biophys. Acta - Mol. Cell Res.* 2015, **1853,** 1130–1144.

115. Li, J. Y. *et al.* Scara5 Is a Ferritin Receptor Mediating Non-Transferrin Iron Delivery. *Dev. Cell* 2009, **16,** 35–46.

116. Stefanini, S. *et al.* Thermal Stability of Horse Spleen Apoferritin and Human Recombinant H Apoferritin. *Arch. Biochem. Biophys.* 1996, **325,** 58–64.

117. Kim, M. *et al.* PH-Dependent Structures of Ferritin and Apoferritin in Solution: Disassembly and Reassembly. *Biomacromolecules* 2011, **12,** 1629–1640.

118. Andrews, S. C., Smith, J. M. A., Yewdall, S. J., Guest, J. R. & Harrison, P. M. Bacterioferritins and Ferritins Are Distantly Related in

Evolution Conservation of Ferroxidase-Centre Residues. *FEBS Lett.* 1991, **293,** 164–168.

119. Douglas, T., Allen, M. & Young, M. Self-assembling Protein Cage Systems and Applications in Nanotechnology. *Biopolym. Online* 2005, **15,** 405–411.

120. Wang, Z. *et al.* Functional Ferritin Nanoparticles for Biomedical Applications. *Front. Chem. Sci. Eng.* 2017, **11,** 633–646.

121. Chen, Z. *et al.* Apoferritin Nanocage for Brain Targeted Doxorubicin Delivery. *Mol. Pharm.* 2017, **14,** 3087−3097.

122. Laghaei, R., Evans, D. G. & Coalson, R. D. Metal Binding Sites of Human H-Chain Ferritin and Iron Transport Mechanism to the Ferroxidase Sites: A Molecular Dynamics Simulation Study. *Proteins Struct. Funct. Bioinforma.* 2013, **81,** 1042–1050.

123. Zhang, S. *et al.* The Size Flexibility of Ferritin Nanocage Opens a New Way to Prepare Nanomaterials. *Small* 2017, **13,** 1–6.

124. Lin, X. *et al.* Chimeric Ferritin Nanocages for Multiple Function Loading and Multimodal Imaging. 2012, **11,** 814–819.

125. Zhen, Z. *et al.* RGD Modified Apoferritin Nanoparticles for Efficient Drug Delivery to Tumors. *ACS Nano.* 2013, **7,** 4830–4837.

126. Truffi, M. *et al.* Ferritin Nanocages : A Biological Platform for Drug Delivery, Imaging and Theranostics in Cancer. *Pharmacol. Res.* 2016, **107,** 57–65.

127. Liu, G., Wu, H., Wang, J. & Lin, Y. Apoferritin-Templated Synthesis of Metal Phosphate Nanoparticle Labels for Electrochemical Immunoassay. *Small* 2006, **2,** 1139–1143.

128. Makino, A. *et al.* Effective Encapsulation of a New Cationic Gadolinium Chelate into Apoferritin and Its Evaluation as an MRI Contrast Agent. *Nanomedicine Nanotechnology, Biol. Med.* 2011, **7,** 638–646.

129. Geninatti Crich, S. *et al.* Mn-Loaded Apoferritin: A Highly Sensitive MRI Imaging Probe for the Detection and Characterization of Hepatocarcinoma Lesions in a Transgenic Mouse Model. *Contrast Media Mol. Imaging* 2012, **7,** 281–288.

130. Simsek, E. & Akif Kilic, M. Magic Ferritin: A Novel Chemotherapeutic Encapsulation Bullet. *J. Magn. Magn. Mater.* 2005, **293,** 509–513.

131. Dostalova, S. *et al.* Site-Directed Conjugation of Antibodies to Apoferritin Nanocarrier for Targeted Drug Delivery to Prostate Cancer Cells. *ACS Appl. Mater. Interfaces* 2016, **8,** 14430–14441.

132. Luo, Y., Wang, X., Du, D. & Lin, Y. Hyaluronic Acid-Conjugated Apoferritin Nanocages for Lung Cancer Targeted Drug Delivery. *Biomater. Sci.* 2015, **3,** 1386–1394.

133. Geninatti Crich, S. *et al.* Targeting Ferritin Receptors for the Selective Delivery of Imaging and Therapeutic Agents to Breast Cancer Cells. *Nanoscale* 2015, **7,** 6527–6533.

134. Sun, C. *et al.* Controlling Assembly of Paired Gold Clusters within Apoferritin Nanoreactor for *in Vivo* Kidney Targeting and Biomedical Imaging. *J. Am. Chem. Soc.* 2011, **133,** 8617–8624.

135. Bradshaw, T. D. *et al.* Apoferritin-Encapsulated PbS Quantum Dots Significantly Inhibit Growth of Colorectal Carcinoma Cells. *J. Mater. Chem. B* 2013, **1,** 6254.

136. Turyanska, L. *et al.* The Differential Effect of Apoferritin-PbS Nanocomposites on Cell Cycle Progression in Normal and Cancerous Cells. *J. Mater. Chem.* 2012, **22,** 660–665.

137. He, Y. *et al.* Near Infrared Dye Loaded Copper Sulfide-Apoferritin for Tumor Imaging and Photothermal Therapy. *RSC Adv.* 2018, **8,** 14268–14279.

138. Agostinis, P. *et al.* Photodynamic Terapy of Cancer: An Update.

CA. Cancer. J. Clin. 2011, **61,** 250–281.

139. Zhen, Z. *et al.* Ferritin Nanocages To Encapsulate and Deliver Photosensitizers for Efficient Photodynamic Therapy against Cancer. *ACS Nano* 2013, **7,** 6988–6996.

140. Delany, I., Rappuoli, R. & De Gregorio, E. Vaccines for the 21st Century. *EMBO Mol. Med.* 2014, **6,** 708–720.

141. Kanekiyo, M. *et al.* Self-Assembling Influenza Nanoparticle Vaccines Elicit Broadly Neutralizing H1N1 Antibodies. *Nature* 2013, **499,** 102–106.

142. Clark, L. A. *et al.* Affinity Enhancement of an *in Vivo* Matured Therapeutic Antibody Using Structure-Based Computational Design. *Protein Sci.* 2006, **15,** 949–960.

143. Löfblom, J. *et al.* Affibody Molecules: Engineered Proteins for Therapeutic, Diagnostic and Biotechnological Applications. *FEBS Lett.* 2010, **584,** 2670–2680.

144. Ståhl, S. *et al.* Affibody Molecules in Biotechnological and Medical Applications. *Trends Biotechnol.* 2017, **20,** 1–22.

145. Nygren, P. Å. & Skerra, A. Binding Proteins from Alternative Scaffolds. *J. Immunol. Methods* 2004, **290,** 3–28.

146. Ahmad, Z. A. *et al.* ScFv Antibody: Principles and Clinical Application. *Clin. Dev. Immunol.* 2012, **2012,** 1–15.

147. Ståhl, S., Kronqvist, N., Jonsson, A. & Löfblom, J. Affinity Proteins and Their Generation. *J. Chem. Technol. Biotechnol.* 2013, **88,** 25–38.

148. Zhao, N. *et al.* Small-Protein-Stabilized Semiconductor Nanoprobe for Targeted Imaging of Cancer Cells. *ChemBioChem* 2016, **17,** 1202–1206.

149. Frejd, F. Y. & Kim, K. T. Affibody Molecules as Engineered

Protein Drugs. *Exp. Mol. Med.* 2017, **49,** 306–313.

150. Peckys, D. B., Korf, U. & de Jonge, N. Local Variations of HER2 Dimerization in Breast Cancer Cells Discovered by Correlative Fluorescence and Liquid Electron Microscopy. *Sci. Adv.* 2015, **1,** 1500165–1500174.

151. Xavier, C. *et al.* 18F-Nanobody for PET Imaging of HER2 Overexpressing Tumors. *Nucl. Med. Biol.* 2016, **43,** 247–252.

152. Gao, J. *et al.* Affibody-Based Nanoprobes for HER2-Expressing Cell and Tumor Imaging. *Biomaterials* 2011, **32,** 2141–2148.

153. Hartsuiker, L., Zeijen, N. J. L., Terstappen, L. W. M. M. & Otto, C. A Comparison of Breast Cancer Tumor Cells with Varying Expression of the HER2/Neu Receptor by Raman Microspectroscopic Imaging. *Analyst* 2010, **135,** 3220.

154. Breast Cancer Statistics. 2018, Available at: https://www.wcrf.org/int/cancer-facts-figures/data-specific-cancers/breast-cancer-statistics.

155. Kuruppu, A. I. The Role of HER Family Signalling in Breast Cancer. (The University of Nottingham, 2016).

156. Riese, D. J. & Stern, D. F. Specificity within the EGF Family/ErbB Receptor Family Signaling Network. *BioEssays* 1998, **20,** 41–48.

157. Iqbal, N., Iqbal, N., Iqbal, N. & Iqbal, N. Human Epidermal Growth Factor Receptor 2 (HER2) in Cancers: Overexpression and Therapeutic Implications. *Mol. Biol. Int.* 2014, **2014,** 1–9.

158. Ménard, S., Pupa, S. M., Campiglio, M. & Tagliabue, E. Biologic and Therapeutic Role of HER2 in Cancer. *Oncogene* 2003, **22,** 6570–6578.

159. Wieduwilt, M. & Moasser, M. The Epidermal Growth Factor Receptor Family: Biology Driving Targeted Therapeutics. *Cell. Mol.*

Life Sci. 2008, **65,** 1566–1584.

160. Burstein, H. J. The Distinctive Nature of HER2-Positive Breast Cancers — NEJM. *N. Engl. J. Med.* 2005, **353,** 1652–1654.

161. Holliday, D. L. & Speirs, V. Choosing the Right Cell Line for Breast Cancer Research. *Holliday Speirs Breast Cancer Res.* 2011, **13,** 215–221.

162. Xing, L., Hung, M., Bonfiglio, T., Hicks, D. G. & Tang, P. Breast Cancer : Basic and Clinical Research The Expression Patterns of ER, PR, HER2, CK5/6 , EGFR, Ki-67 and AR by Immunohistochemical Analysis in Breast Cancer Cell Lines. *Breast Cancer Basic Clin. Res.* 2010, **4,** 35–41.

163. Neve, R. M. *et al.* A Collection of Breast Cancer Cell Lines for the Study of Functionally Distinct Cancer Subtypes. *Cancer Cell* 2006, **10,** 515–527.

164. Bakueva, L. *et al.* PbS Quantum Dots with Stable Efficient Luminescence in the Near-IR Spectral Range. *Adv. Mater.* 2004, **16,** 926–929.

165. Nakane, Y., Tsukasaki, Y., Sakata, T., Yasuda, H. & Jin, T. Aqueous Synthesis of Glutathione-Coated PbS Quantum Dots with Tunable Emission for Non-Invasive Fluorescence Imaging in the Second Near-Infrared Biological Window (1000–1400 Nm). *Chem. Commun.* 2013, **49,** 7584–6.

166. Sambrook, J. F., Fritsh, E. F. & Maniatis, T. *Molecular Cloning: A Laboratory Manual. 2nd Edition; Cold Spring Harbor Laboratory Press*. (1989).

167. Zhang, L. Multifunctional Apoferritin and Dps Protein Nanoparticles for *In Vivo* Imaging and Breast Cancer Treatment. (PhD thesis, University of Nottingham, 2015).

168. Tayyab, S., Qamar, S. & Islam, M. Size Exclusion

Chromatography and Size Exclusion HPLC of Proteins. *Biochem. Educ.* 1991, **19,** 149–152.

169. Wingfield, P. T. Protein Precipitation Using Ammonium Sulfate. *Curr. Protoc. Protein. Sci.* 2001, 1–10.

170. Andersen, K. R., Leksa, N. C. & Schwartz, T. U. Optimized E. Coli Expression Strain LOBSTR Eliminates Common Contaminants from His-Tag Purification. *Proteins.* 2013, **81,** 1857–1861.

171. Riss, T. L. *et al.* Cell Viability Assays. in *Assay Guidance Manual.* (2013). **114,** 785–796.

172. Boles, M. A., Ling, D., Hyeon, T. & Talapin, D. V. The Surface Science of Nanocrystals. *Nat. Mater.* 2016, **15,** 141–153.

173. Deng, D. *et al.* Forming Highly Fluorescent Near-Infrared Emitting PbS Quantum Dots in Water Using Glutathione as Surface-Modifying Molecule. *J. Colloid Interface Sci.* 2012, **367,** 234–240.

174. Zhang, C. *et al.* Combination of Cation Exchange and Quantized Ostwald Ripening for Controlling Size Distribution of Lead Chalcogenide Quantum Dots. *Chem. Mater.* 2017, **29,** 3615–3622.

175. Turyanska, L., Patanè, A., Henini, M., Hennequin, B. & Thomas, N. R. Temperature Dependence of the Photoluminescence Emission from Thiol-Capped PbS Quantum Dots. *Appl. Phys. Lett.* 2007, **90,** 101913–101916.

176. Jalilehvand, F., Sisombath, N. S., Schell, A. C. & Facey, G. A. Lead(II) Complex Formation with L-Cysteine in Aqueous Solution. *Inorg. Chem.* 2015, **54,** 2160–2170.

177. Hennequin, B. *et al.* Aqueous Near-Infrared Fluorescent Composites Based on Apoferritin- Encapsulated PbS Quantum Dots. *Adv. Mater.* 2008, **20,** 3592–3596.

178. Dinescu, A., Cundari, T. R., Bhansali, V. S., Luo, J. L. & Anderson, M. E. Function of Conserved Residues of Human

Glutathione Synthetase: Implications for the ATP-Grasp Enzymes. *J. Biol. Chem.* 2004, **279,** 22412–22421.

179. Li, J. *et al.* Naphthalene-Based Fluorescent Probes for Glutathione and Their Applications in Living Cells and Patients with Sepsis. *Theranostics* 2018, **8,** 1411–1420.

180. Tiwari, D. K. *et al.* Synthesis and Characterization of Anti-HER2 Antibody Conjugated CdSe/CdZnS Quantum Dots for Fluorescence Imaging of Breast Cancer Cells. *Sensors* 2009, **9,** 9332–9354.

181. Jin, T. & Imamura, Y. Applications of Highly Bright PbS Quantum Dots to Non-Invasive Near-Infrared Fluorescence Imaging in the Second Optical Window. *ECS J. Solid State Sci. Technol.* 2016, **5,** 3138–3145.

182. Sahandi Zangabad, P. *et al.* Nanocaged Platforms: Modification, Drug Delivery and Nanotoxicity. Opening Synthetic Cages to Release the Tiger. *RSC Nanoscale* 2017, **9,** 1356–1392.

183. Ruozi, B. *et al.* Apoferritin Nanocage as Streptomycin Drug Reservoir: Technological Optimization of a New Drug Delivery System. *Int. J. Pharm.* 2017, **518,** 281–288.

184. Tolmachev, V. *et al.* Affibody Molecules: Potential for *in Vivo* Imaging of Molecular Targets for Cancer Therapy. *Expert Opin. Biol. Ther.* 2007, **7,** 555–568.

185. Strupat, K. Molecular Weight Determination of Peptides and Proteins by ESI and MALDI. *Methods Enzymol.* 2005, **405,** 1–36.

186. Ghirlando, R., Mutskova, R. & Schwartz, C. Enrichment and Characterization of Ferritin for Nanomaterial Applications. *Nanotechnology* 2015, **27,** 45102.

187. Chen, X., Zaro, J. & Shen, W.-C. Fusion Protein Linkers: Property, Design and Functionality. *Adv Drug Deliv Rev.* 2013, **65,** 1357–1369.

188. Truffi, M. *et al.* Ferritin Nanocages: A Biological Platform for Drug Delivery, Imaging and Theranostics in Cancer. *Pharmacol. Res.* 2016, **107,** 57–65.

189. Wang, X., Dong, J., Liu, X., Liu, Y. & Ai, S. A Novel PH-Controlled Immunosensor Using Hollow Mesoporous Silica and Apoferritin Combined System for Target Virus Assay. *Biosens. Bioelectron.* 2014, **54,** 85–90.

190. Shi, J., Xiao, Z., Kamaly, N. & Farokhzad, O. C. Self-Assembled Targeted Nanoparticles: Evolution of Technologies and Bench to Bedside Translation. *Acc. Chem. Res.* 2011, **44,** 1123–1134.

191. Kilic, M. A., Ozlu, E. & Calis, S. A Novel Protein-Based Anticancer Drug Encapsulating Nanosphere: Apoferritin-Doxorubicin Complex. *J. Biomed. Nanotechnol.* 2012, **8,** 508–514.

192. Blazkova, I. *et al.* Apoferritin Modified Magnetic Particles as Doxorubicin Carriers for Anticancer Drug Delivery. *Int. J. Mol. Sci.* 2013, **14,** 13391–13402.

193. Turyanska, L. *et al.* The Differential Effect of Apoferritin-PbS Nanocomposites on Cell Cycle Progression in Normal and Cancerous Cells. *J. Mater. Chem.* 2012, **22,** 660–665.

194. Liu, X. *et al.* Apoferritin-Camouflaged Pt Nanoparticles: Surface Effects on Cellular Uptake and Cytotoxicity. *J. Mater. Chem.* 2011, **21,** 7105–7110.

195. Ekerljung, L., Lennartsson, J. & Gedda, L. The HER2-Binding Affibody Molecule (ZHER2:342)2 Increases Radiosensitivity in SKBR-3 Cells. *PLoS One* 2012, **7,** 3–8.

196. Levy, R. I., Grizzle, J. E. & Nichols, A. V. Nutrient Intake and Its Association with High-Density Lipoprotein and Low-Density Lipoprotein Cholesterol in Selected US and USSR Subpopulations. The US-USSR Steering Committee for Problem Area I: The Pathogenesis of Atherosclerosis. *Am. J. Clin. Nutr.* 1984, **39,** 942–952.